SPECTROSCOPIC ANALYSIS AND TEMPORAL EVOLUTION OF LASER-INDUCED PLASMA IN DIFFERENT SAMPLES

J. J. Camacho[1*], L. Díaz[2], J. P. Cid[1] and J. M. L. Poyato[1]

[1]Departamento de Química-Física Aplicada. Facultad de Ciencias. Universidad Autónoma de Madrid. Cantoblanco. 28049-Madrid. Spain

[2]Instituto de Estructura de la Materia, CFMAC, CSIC, Serrano 121. 28006-Madrid, Spain

ABSTRACT

When the radiation of a powerful pulsed laser is focused on the surface of a solid target or in a volume filled with gas, a visible bright flash and hot plasma is produced. A study of the electronic spectra of the different laser-produced plasmas enables us to understand the physical and chemical processes that take place in terrestrial and cosmic plasmas. The aim of this chapter is to provide some fundamentals of laser-induced breakdown spectroscopy (LIBS) and to report recent experimental studies developed in our laboratory on plasmas generated in different samples (He, Ge, GeH_4 and CO_2). We describe the expansion of laser-induced plasma in these samples. The plasmas were spectroscopically analyzed in the UV-Visible-near IR range. The spectra are dominated by emission of strong atomic and ionic species and also some weak intensity molecular bands are observed. Plasma characteristics were examined in detail on the emission lines from diverse excited species by time-resolved optical emission spectroscopy (OES) technique. The measurements allow us to obtain excitation temperature, electron number density, velocity and kinetic energy distributions for different species. Excitation temperatures were estimated from the intensities of atomic and ionic lines. Electron number densities were deduced from the Stark broadening of several spectral lines. The velocity and kinetic energy distributions were obtained from time-of-flight OES measurements. In the case of gaseous samples, the characteristics of the spectral emission intensities from different species have been investigated as a function of the gas pressure and laser irradiance. Optical breakdown threshold intensities in gases have been measured experimentally. The physical processes leading to laser-induced breakdown of the gases have been analyzed. From the time evolution of line intensity and electron density some considerations about ionization and recombination processes were made. Three-body electron-ion recombination rate constants were also estimated.

* Corresponding author; E-mails: j.j.camacho@uam.es; luisol@cfmac.csic.es; juanpablo.cid@uam.es; jml.poyato@uam.es.

1. INTRODUCTION

A striking demonstration of the interaction of radiation with matter is the plasma formation which occurs when a high-power laser is focused in a gas or on a solid material. Strong pulses of infrared (IR) laser light can cause breakdown and plasma formation in gases, which are usually transparent at these wavelengths. In the case of solid materials, an ablation plasma plume can be formed above the sample surface. This plasma may absorb a part of the laser pulse, shielding the sample, increasing its temperature and decreasing the efficiency of laser energy available for mass ablation. In these conditions, gases or ablation plumes are transformed into opaque, highly conducting plasma in times of the order of nanoseconds. The properties and composition of the resulting plasma may evolve, both as a result of collisions between particles in the plasma and through plasma-laser radiation interactions. The transformation from neutral gas into hot plasma takes place in three quite distinct stages: initiation, formative growth, and plasma development accompanied by shock wave generation and propagation in the surrounding gas. A fourth and final stage, extinction, follows.

The formation of laser-induced breakdown (LIB) plasma in a gas has been investigated since its discovery by Maker *et al* [1], resulting in several studies that have been summarized by different authors [2-16]. On the other hand, the interaction of a high-energy infrared (IR) pulsed laser beam with solid materials has been investigated extensively over the past several years, due to its significance in technologies such as laser sampling for chemical analysis and pulsed laser deposition of thin film [17-21]. Due to the many experimental parameters involved in these experiments, an exhaustive investigation of the plasma would involve the processing of an impressive number of records. To investigate LIB of gases and ablation plasma plume, several diagnostic techniques have been employed in the last years. Optical emission spectroscopy (OES) is a powerful tool to get information on the LIB species. Because of the transient features of the plume created by LIB, OES technique, with time and space resolution, is especially appropriate to obtain information about the behaviour of the formed species in space and time as well as about the dynamics of the plasma evolution. Although OES gives only partial information about the plasma particles, this diagnostic technique help to us to draw a picture of the plasma in terms of the emitting chemical species, to evaluate their possible mechanisms of excitation and formation and to study the role of gas-phase reactions in the plasma expansion process.

The objectives of this work are: (i) to show some fundamentals of laser-induced breakdown spectroscopy (LIBS) and, (ii) to review our recent results on LIBS analysis of chemical species in gases plasmas and ablation plumes induced by high-power IR CO_2 laser, adding some new results. This chapter describes the experimental results obtained from ultraviolet-visible-near infrared (UV-Vis-NIR) spectra of LIB plasmas generated by carbon dioxide laser pulses in gases such as He, GeH_4 and CO_2 and in the ablation plumes on Ge. The major parts of this work have already published by us in different journals [22-25]. We consider here only research on the plasma induced when a high-intensity laser radiation is focused in a gas or onto a solid surface. The emission observed in the laser-induced plasma region is due to electronic relaxation of excited atoms, ions and molecules. Line intensities from different atomic and ionic species were

used for determining electron temperature, and Stark-broadened profiles of some lines were employed to calculate electron density. The characteristics of the spectral emission intensities from different species have been investigated as functions of the gas pressure and laser irradiance. Optical breakdown threshold intensities in the different studied gases have been determined. We discuss the dynamics of the plume expansion and formation of different species for various delay times with respect to the beginning of the laser pulse. The velocity and kinetic distributions were obtained from the time-of-flight (TOF) measurements using time-resolved OES. Possible mechanisms for the production of these distributions are discussed. The temporal behavior of the electron number density has been employed for the estimation of three-body recombination rate constant and recombination time. The present paper is aimed at discussing temporal processes produced by high-power IR CO_2 pulsed laser on several gases and at evaluating LIB changes, which are of fundamental importance in establishing the mechanisms responsible for the plasma emission.

2. Fundamentals of Laser Induced Breakdown Spectroscopy (LIBS)

Laser-induced breakdown spectroscopy (LIBS) is a simple, rapid, real-time analytical technique based on the analysis of the spectral emission from laser-induced sparks or plasmas. The LIBS technique operates by focusing the laser into a small volume of gaseous sample or onto a small area at the surface of the solid sample. Excellent textbooks and reviews about the fundamentals of LIBS and examples of various processes are readily available today [26-29]. The LIBS technique, called sometimes laser-induced plasma spectroscopy (LIPS), is a method of atomic-molecular emission spectroscopy which utilizes a highly-power laser pulse as the excitation source. LIBS can analyze any matter regardless of its physical-state, being it solid, liquid or gas. Because all elements emit light when excited to sufficiently high energy, LIBS can detect different species (atomic, ionic and molecular) and limited only by the power of the laser as well as the sensitivity and wavelength range of the spectrograph/detector. When power densities exceed hundreds of MW/cm^2, a high-temperature, high electron density laser spark or plasma is formed. The temperature of this plasma, initially, is very hot: 10^4 to 10^7 ºC. At such a high temperature, any sample material is broken down, vaporized, and ionized. In the early stages of plasma thermalization, as electrons interact and recombine with ions, energy will be released over a broad spectral range, from soft X rays through the visible to the near IR. At the early time, the plasma emits a continuum of radiation which does not contain any known information about the present species and within a very small timeframe the plasma expands at supersonic velocities and cools. This continuum emission can be gated off by a detection system. After suitable time delays, the plasma cools down to the point when neutral atoms in excited states are formed. Time-resolved spectral analysis of these atomic emissions yields a fingerprint of the atomic species present in the sample. The greatest advantage of LIBS is the simplicity of experimental arrangement, which makes it cheap. It provides simultaneous multi-element analysis, with no sample preparation. Application of optical fiber techniques to this method enables the construction of a simple and compact device for real time remote sensing of solid, liquid, and gaseous samples. The LIBS technique has several limitations, such as self-absorption of emission, line broadening, and

continuum background. These limitations may be minimized by the optimal time gating. Another limitation for quantitative determination of absolute concentrations is related to the relatively low precision (≈ 5%) and relatively high limit of detection (up to 100 ppb). If you would like to have a detection limit, say, of subparts per trillion, then definitely, you have to use another method as, for example, laser atomic fluorescence (LAF) spectroscopy. The LAF technique is based on the absorption of resonant laser radiation by the atomized analyte atom and the detection of the subsequently emitted fluorescence radiation. This technique requires utilization of expensive and sophisticated frequency-tunable lasers with narrow bandwidth to make this light-atom interaction extremely selective. It has the ability to detect as low as subparts per trillion. However, if you are interested in a detection limit, say, of some parts per million, well, definitely, laser breakdown spectroscopy is your choice. Basically LIBS makes use of OES and is to this extent very similar to arc/spark emission spectroscopy. The LIBS technique is similar and complementary to a number of other laser-based techniques (Raman spectroscopy, laser-induced-fluorescence, etc). In fact devices are now being manufactured which combine these techniques in a single instrument, allowing the atomic, molecular and structural characterization of a sample as well as giving a deeper insight into physical properties. A typical LIBS system consists of a pulsed laser and a spectrometer with a wide spectral range and a high sensitivity, fast response rate and time gated detector. The principal advantages of LIBS over the conventional analytical spectroscopic techniques are its simplicity and the sampling speed.

2.1. Nature of the Plasmas

Plasma is an ionized gas, a distinct fourth state of matter. The free electric charges (electrons and ions) make plasma electrically conductive (sometimes more than gold and copper), internally interactive, and strongly responsive to electromagnetic fields. Ionized gas is usually called plasma when it is electrically neutral (i.e., electron density is balanced by that of positive ions) and contains a significant number of the electrically charged particles, sufficient to affect its electrical properties and behaviour. Plasmas occur naturally but also can be effectively man-made in laboratory and in industry, which provides opportunities for numerous applications, including thermonuclear synthesis, electronics, lasers, fluorescent lamps, and many others.

Plasma offers three major features that are attractive for applications in chemical-physics: (1) temperatures and energy density of at least some plasma components can significantly exceed those in conventional technologies, (2) plasmas are able to produce very high concentrations of energetic and chemically active species (e.g., electrons, ions, atoms, molecules and radicals, excited states, and different wavelength photons), and (3) plasma systems can essentially be far from thermodynamic equilibrium, providing extremely high concentrations of chemically active species and keeping bulk temperature as low as room temperature. These plasma features permit significant intensification of traditional chemical processes, essential increase of their efficiency, and often successful stimulation of chemical reactions impossible in conventional chemistry. Plasmas are found in nature in various forms and are characterized normally by their electron density n_e and electron temperature T_e. On earth they exist in the ionosphere at height of 70-500 km (density $n_e = 10^6$ cm^{-3}, $T_e = 2300$ K). Solar wind is

another natural plasma originating from the sun with n_e = 10 cm^{-3} and T_e = 10^5 K. The corona which extends around the sun has an electron density n_e = 10^8 cm^{-3} and its electron temperature is T_e = 10^6 K. Finally, white dwarfs, the final state of stellar evolution, have a n_e of 10^{30} cm^{-3}. In plasma formation, as the temperature of material is raised, its state changes from solid to liquid and then to gas. If the temperature is elevated further, an appreciable number of gas atoms are ionized and go into a high temperature gaseous state in which the charge numbers of ions and electrons are almost the same and charge neutrality is satisfied at a macroscopic scale. When the ions and electrons move collectively, these charged particles interact via Coulomb forces which are long-range forces and decay with the inverse square of the distance between charged particles. Therefore, many charged particles interact with each other by long range forces rather then through short range collision process like in a common gas. This results in different kinds of collective phenomena such as plasma instabilities and wave phenomena [30].

2.2. Plasma formation and evolution.

Plasma is a local assembly of atoms, molecules, ions and free electrons, overall electrically neutral, in which the charged species often act collectively. The LIB plasma is initiated by a single laser pulse. If we consider the temporal evolution of LIB plasma, at early times the ionization grade is high. As electron-ion recombination proceeds, neutral atoms and molecules form. A recombination occurs when a free electron is captured into an ionic or atomic energy level and gives up its excess kinetic energy in the form of a photon. LIB plasmas are characterized by a variety of parameters, the most basic being the degree of ionization. A weakly ionized plasma is one in which the ratio of electrons to other species is less than 10%. At the other extreme, high ionized plasmas may have atoms stripped of many of their electrons, resulting in very high electron to atom/ion ratios. LIB plasmas, for low power laser intensities, fall in the category of weak ionized plasmas. At high laser power densities, LIB plasmas correspond to strong ionized plasmas.

2.2.1. Initiation Mechanism: Multiphoton Ionization (MPI) and Electron Impact Ionization (EII)

Plasma is initiated by electron generation and electron density growth. The conventional LIB plasma can be initiated in two methods: multiphoton ionization (MPI) and electron impact ionization (EII) both followed by electron cascade. EII is sometimes denominated as cascade ionization process or avalanche ionization due to inverse bremsstrahlung (IB) heating of electrons.

In the MPI, an atom or a gas molecule A simultaneously absorbs a number of photons n. If the absorbed energy is higher than the ionization potential $I_P(A)$, the gas is ionized:

$$nh\nu + A \rightarrow A^+ + e + I_P(A);\ nh\nu \geq I_P(A), \qquad (2.1)$$

where n is the number of photons needed to strip off an electron, which corresponds to the integer part of the quantity:

$$n = \frac{I_P + \varepsilon_{osc}}{h\nu} + 1. \tag{2.2}$$

Here ϵ_{osc} is the oscillation energy of a free electron in the alternating electric field. Multiphoton ionization has been studied by many authors and several reviews of past work are available [6,31,32]. Calculations of the MPI rate W_{MPI}, based on m-order perturbation theory, have been proposed [6,33,34]. Within the classical microwave breakdown theory [35], a free electron oscillates in the alternating electric field E of the laser electromagnetic wave with frequency ω and wavelength λ(μm), and its oscillation energy,

$$\varepsilon_{osc}[eV] = \frac{e^2E^2}{4m\omega^2} = \frac{e^2}{4m\pi c^3} I_W \lambda^2 = 4.67\times10^{-14} I_W \lambda^2, \tag{2.3}$$

remains constant. In Eq. (2.3) e is the electron charge and I_w is the laser intensity [irradiance, power density or flux density in W×cm^{-2}]. The probability of MPI W_{MPI}, by absorbing simultaneously n laser photons to strip off an electron, is expressed by the classical formula [36]

$$W_{MPI}[s^{-1}] \cong \omega\, n^{3/2} \left(1.36\frac{\varepsilon_{osc}}{I_P}\right)^n = 1.88\times10^{15} \lambda^{2n-1} n^{3/2} \left\{\frac{6.35\times10^{-14} I_W}{I_P}\right\}^n, \tag{2.4}$$

where I_P is in eV. Besides, the probability of simultaneous absorption of photons decreases with the number of photons n necessary to cause ionization. Therefore, the MPI rate is proportional to I_W^n and inversely proportional to I_P^n. Multiphoton ionization predicts a very weak dependence of the threshold flux on gas pressure. In addition, although MPI process may provide the initial electrons, it does not account entirely for the breakdown phenomena, except possibly at very short wavelengths (<1 μm) or at very low pressures (<1 kPa), where collisional effects are negligible [34]. Keldysh [33] has shown that the MPI effect and the tunnel effect have a common nature, and are limiting cases of a single process in which one electron goes from a bound state in the atom into a free state under the influence of an alternating electromagnetic field.

In the MPI process, most treatments based on n-order perturbation theory show that the transition probability for n photon absorption may by simply expressed as:

$$W_{MPI} = AF^n \quad \text{where } A = \frac{\sigma^n \tau_l^{n-1}}{(n-1)!}, \tag{2.5}$$

being F the flux density in photons/cm^2 s, σ is the photon absorption cross-section and τ_l is the mean lifetime of an excited species.

There are many effects that can significantly enhance the ionization rate. It has been shown that a strong electromagnetic field can decrease the number of photons required for the photoionization process. This is because of the action of the field on the upper and intermediate energy levels of an atom. A strong field results in Stark shifting and broadening of the intermediate energy levels and bringing them into resonance. This effect become quite important when an atom is ionized via the quasi-resonant intermediate excitation states. The second effect is due to the overlapping and merging of the upper energy levels into a quasi-continuum spectrum under a strong field. This effect can decrease in the effective ionization potential by an amount of approximately 1 eV. An additional effect that can significantly change the prediction of the ionization rate can be attributed to the laser modes of operation. Q-switched laser pulses of nanosecond duration are usually composed of many cavity modes. The larger the number of modes, the more incoherent the beam becomes. Beam coherence will play an important role since the local fields in a very small volume can greatly exceed the average value over the focusing volume. Picosecond pulses are considered coherent because there is a correlation of the phases of the many longitudinal modes of the cavity leading to constructive interference over the picosecond pulse lengths. Effects of nanosecond are that the ionization efficiency from nanosecond laser pulses drops significantly in comparison with femtosecond laser pulse excitation.

The EII process consists on the absorption of light photon by free or quasifree electrons, producing electrons with enough kinetic energy e^* to ionize one atom or molecule: $e + n\mathrm{h}\nu + A \rightarrow e^* + A \rightarrow 2e + A^+$. The electrons then absorb more photons via the inverse bremsstrahlung process. If the electrons gain sufficient energy, they ionize other gas molecules on impact, leading to an electron cascade and breakdown of the gas. The cascade ionization process is significant at high pressure and longer laser pulse because under these conditions, electron–atom or electron–ion collisions have sufficient time to occur during the laser pulse. According to Morgan [6], this condition is determined when the product of gas pressure and laser pulse width, $p \times \tau_p$, is greater than 10^{-7} Torr.s. This process is a competing process between the process by which the energy gained causing rapid ionization and the processes by which electrons vanish or lose energy. Two conditions must co-exist for EII to initiate: (i) an initial electron must reside in the focal volume; and (ii) the initial electron must acquire energy which exceeds the ionization energy of the material in the focus. These initial electrons can be produced by MPI, if the laser intensity is high enough. The presence of impurities, such as aerosol particles or low ionization-potential organic vapours, can also significantly facilitate the generation of the initial electrons. In addition, these free or quasifree electrons can be produced by the effect of cosmic ray ionization or natural ionization. The equilibrium number of free electrons and ions per cm^3 in the atmosphere at the earth's surface is about 500 [37]. The electron cascade ionization process requires the presence of either free electrons or excited atoms or molecules in the focal region for their initiation, but the possibility of a free electron or an excited atom produced by natural causes being present there during the laser flash can be discounted, as Tozer pointed out [38]. They occur naturally in the earth's atmosphere, produced at a rate of about 10 $cm^{-3} \times s^{-1}$ at the earth's surface by the presence of local radioactivity and the passage of ultraviolet radiation and cosmic rays. Most electrons become rapidly attached to electronegative atoms and molecules to form negative ions. The mean

lifetime of a free electron in the atmosphere is about 10^{-7} s, so that the aggregate life of free electrons is about 10^{-6} s when liberated at the rate of ≈ 10 cm$^{-3}\times$s^{-1}. The probability of finding a free electron in the focal region ($\approx 10^{-4}$ cm^3) during a laser flash ($\approx 10^{-8}$ s) is thus entirely negligible, as is the chance for finding an excited atom. One concludes that the laser light itself produces the initiatory electrons. These electrons in the focal volume gain sufficient energy, from the laser field through IB collision with neutrals, to ionize atoms, molecules or ions by inelastic electron-particle collision resulting in two electrons of lower energy being available to start the process again

$$e^*[\epsilon \geq I_P(A)] + A \rightarrow A^+ + 2e;\ e^*[\epsilon \geq I_P(A^+)] + A^+ \rightarrow A^{2+} + 2e. \qquad (2.6)$$

Thus a third species (atom-molecule/ion) is necessary for conserving momentum and energy during optical absorption. The recurring sequences of IB absorption events and subsequent EII lead to a rapid growth in the number of free electrons, if the laser intensity is sufficient to overcome the losses of free electrons through diffusion out of the focal volume and through recombination. The MPI mechanism dominates electron generation only for low exciting wavelengths. Therefore, initial EII becomes a problem at a higher wavelength because neither cascade nor MPI can furnish the sufficient number of electrons. At higher laser intensities, electric field of the laser can pull an outer shell electron out of its orbit. After the initial electron ejection, the LIB plasma is commonly maintained by the absorption of optical energy and EII. Electrons in the laser field will gain energy through electron-neutral IB collisions and will lose energy by elastic and inelastic collisions with the neutral species through excitation of rotational and vibrational degree of freedom of molecules and excitation of electronic states. While some electrons will be lost by attachment, new electrons will be produced by ionizing collisions. At high laser intensity, few electrons will be generated with energy larger than the ionization energy. The wavelength-resolved emission spectra from the laser plasma are not expected to vary due to the plasma origin. However, plasma origin may be relevant, if the enhancement is observed between UV, visible and IR excitation wavelengths.

2.2.2. Continuity rate equation. Electron attachment, recombination and diffusion

When the LIB plasma is formed, its growth is governed by the continuity rate equation for the electron density [39] due to the combined effect of EII and MPI

$$\frac{dn_e}{dt} = \nu_i n_e + W_{MPI} I_W^n N - \nu_a n_e - \nu_R n_e^{\ 2} + D_e \nabla^2 n_e, \qquad (2.7)$$

where ν_i is the impact ionization rate, W_{MPI} is the multiphoton ionization rate coefficient, I_w is the intensity of the laser beam, n is the number of photons required for MPI, N is the number of atoms/molecules per unit volume, ν_a is the attachment rate, ν_R is the recombination rate and D_e is the electron diffusion coefficient. The term dn_e/dt is the net rate of change in electron concentration at a point in the focal volume at a time t after the release of initiatory electrons. On the right side of Eq. (2.7), the first term is the electron generation due to impact ionization. The second term on the right is MPI rate.

The third, fourth and fifth terms are sinking terms which represent electron attachment, recombination and diffusion, respectively. Impact ionization is defined by multiplying the number of electrons per unit volume to the impact ionization rate ν_i. The impact ionization rate refers to the rate at which electrons are generated by ionizing collisions. At a high laser intensity, a few new electrons can be generated and gain energy larger than their ionization energy, which leads to the generation of new electrons by impact ionization, thereby leading to the cascade growth. Recombination losses are usually not important in the breakdown forming stage. On the other hand, recombination processes can counterbalance the electron generation by EII and MPI thus reducing the charged particles number densities in the plasma. If the recombination time constant is comparable to or longer than the laser pulse duration, electrons generated by ionization processes can effectively contribute to the IB absorption.

Electron attachment is the rate of electron attachment ν_a multiplied by the number of electrons per unit volume. The LIB plasma typically loose electrons to the neutral species via the attachment mechanism in the form of three-body attachment or two-body dissociative attachment. Three-body attachment is: $e + AB + X \rightarrow AB^- + X$, where X appears to be a facilitator that allows the electrons to be gained by AB even although X remains unchanged throughout the process. Two-body dissociative attachment is: $e + AB \rightarrow A^- + B$. In this mechanism the electrons must exhibit a threshold electron energy that is equal to the difference between the dissociative energy of AB and the attachment energy of A, which results in the separation of A and B.

Electron recombination is the rate of electron recombination ν_R multiplied to the number of electrons per unit volume. When the electron density is high, such as during the last stage of cascade breakdown, the LIB plasma can lose electrons to ions through electron-ion recombination. Similar to the electron attachment, three-body recombination and two-body recombination occurs as: $e + AB^+ + X \rightarrow AB + X$, $e + AB^+ \rightarrow A + B$. The electron-ion recombination rate has been studied theoretically for a three-body recombination by Gurevich and Pitaevskii [40]

$$\nu_R = 8.8\times10^{-27}\frac{n_e^2}{T_e^{3.5}}\ [s^{-1}], \tag{2.8}$$

where n_e is the electron density in cm^{-3} and T_e is the electron temperature in eV. The electron diffusion term is expressed as $D_e\nabla^2 n_e$ [Eq. (2.7)]. This loss mechanism, more important for a small diameter laser beam, is the diffusion of electrons out of the focal volume. Morgan [6] referred to the combined effect of diffusion and cascade ionization as the responsible for top-hat intensity profile. By imposing an electron skin at the edge of the intensity profile, they found that the electron density grows exponentially as

$$\langle v_e \rangle = \frac{2.408 D_e}{r^2}\ , \tag{2.9}$$

where the first member is the average electron velocity, D_e is electron diffusion coefficient and r is the radius of the beam. The equation (2.9) is intended to be an upper

boundary for diffusion losses only because laser beams typically have a radial distribution closer to the Gaussian rather than top-hat distribution.

In LIB plasmas, the decrease of electron density is mainly due to recombination between electrons and ions in the plasma. These processes correspond to the so-called radiative recombination and three-body recombination processes in which a third body may be either a heavy particle or an electron. The electron number density n_e (cm^{-3}) in the laser induced plasma is governed by the kinetic balance equation [40, 41]

$$\frac{dn_e}{dt} = k_{ion} n_e N_i - k_{rec} n_e^3, \tag{2.10}$$

where N_i indicates the concentration of heavy particles (neutrals and ions) and k_{ion} (cm^3 s^{-1}) and k_{rec} (cm^6 s^{-1}) denote the rate constants of ionization ($e + A \rightarrow A^+ + 2e$) and tree-body electron-ion recombination ($2e + A^+ \rightarrow A^* + e$), respectively. The excess of energy in three-body electron-ion recombination is deposited as kinetic energy to a free electron, which participates in the recombination process as a third body partner. The three-body electron-ion recombination energy can be converted into radiation in the process of radiative electron-ion recombination ($e + A^+ \rightarrow A^* \rightarrow A + h\nu$). The cross section of this process is relatively low, and it can be competitive with three-body electron-ion recombination only when the plasma density is low. If $dn_e/dt=0$ an equilibrium condition can be established; if $dn_e/dt\neq0$, then ionization ($dn_e/dt>0$) or three-body recombination ($dn_e/dt<0$) prevails and departure from equilibrium occurs [40]. The second derivative of $Y=dn_e/dt$ with respect to the electron number density is given by

$$\frac{d^2Y}{dn_e^2} = -6k_{rec} n_e. \tag{2.11}$$

The recombination time can be determined by the value of the rate constant of the recombination process as $t_{rec}=1/(n_e^2.k_{rec})$ [41]. In summary, the process of plasma initiation essentially consists in the formation of free or quasi-free electrons by interplay of MPI and EII. Therefore, two mechanisms MPI and EII can initiate a conventional LIB plasma formation. After the LIB plasma formation, the temporal growth is governed by the equation (2.7). The recombination of these two source terms (MPI and EII) and three sink terms (electron attachment, electron recombination and electron diffusion) controls the development of the conventional LIB plasma. The decrease of n_e is mainly due to the so-called radiative recombination and the three-body recombination processes in which a third body may be either a heavy particle or an electron. These mechanisms that directly affect the temporal development of the LIB plasma, determine the necessary spectroscopic techniques required to spectrally resolve elemental species inside the LIB plasma.

2.2.3. Optical Breakdown: Threshold Intensities

The minimum power density required to form a plasma is called the breakdown threshold; different types of lasers, samples, and environmental conditions will have

different breakdown thresholds. Breakdown thresholds of solids and liquids are usually much lower than those for gases. The principal method of investigation has been to measure the beam intensity required for electron liberation and the minimum intensity needed to produce the breakdown as a function of the radiation wavelength and pressure of a variety of gases. Precise measurements of the intensities of laser radiation required to release initiatory electrons or to lead to breakdown are made only with the greatest difficulty. The difficulties arise on account of the imprecise definition of the extent of the focal region and inaccurate knowledge of the spatial-temporal characteristics of the beam intensity within the focal region, which, in turn, lead to uncertainties in the absolute value of the instantaneous radiation intensity. The parameters which characterize a focused laser beam are its polarization, wavelength, line width, duration, divergence and the temporal and spatial distribution of intensity. For a given pulse, these are functions of the laser and focusing system governed by the mode structure within the laser cavity, by the aberration functions of the lens or focusing mirror, and by the beam diameter at the lens or mirror. In specifying the electron liberation or breakdown threshold intensities all these factors should ideally be specified, but, regrettably, in the literature, there are often inadequate details and essential features of experimental procedures are frequently omitted. In consequence, many published data are of little value, serving merely to indicate orders of magnitude and broad trends only rather than absolute values in well-defined conditions. For these reasons data published by various workers are often contradictory, and reliable interpretation is sometimes difficult to make.

For gases to breakdown, a certain concentration of electrons has to be reached before the end of the laser pulse. Laser-induced breakdown is frequently defined [5, 30] as an electron density multiplication during the laser pulse by a factor of 10^{13} corresponding to 43 electron generations. In fact, multiplying the natural electron density by 10^{13} leads to $n_e \approx 10^{16}$ cm^{-3} which is the electron density of plasmas at the atmospheric pressure for which electron-ion IB dominates electron-neutral IB. With respect to electron-neutral IB, the electron-ion IB has a much higher efficiency as consequence of the long range Coulomb interaction, and a plasma with an electron density $n_e = 10^{16}$ cm^{-3} is quasi instantaneously completely ionized.

The condition for the optical breakdown is taken to occur when the number density of the induced electrons equals the critical density for the laser wavelength. The critical plasma density

$$n_{e,cr}\left[\mathrm{cm}^{-3}\right] = m\ \omega^2 / 4\pi e^2 \cong 1.1\times 10^{21} / \lambda^2\left[\mu\mathrm{m}\right] \qquad (2.12)$$

is the density where the electron plasma frequency equals the laser frequency ($n_{e,cr} \approx 10^{19}$ cm^{-3} for CO_2 laser). When the electron density exceeds the critical density the sample is not transparent any more. Energetic electrons produce excited species through impact excitation, dissociation and ionization of gas molecules. According to the microwave theory [22], electrons gain energy from the laser radiation field by elastic collisions with neutral atoms at the rate:

$$(\mathrm{d}\varepsilon / \mathrm{d}t)_{\mathrm{gain}} = (e^2 F_E^2 / m)\cdot[\nu_c^2 /(\omega^2 + \nu_c^2)], \qquad (2.13)$$

where F_E and ω are the root-mean-square electric field and angular frequency of the radiation and ν_c is the electron-neutral collision frequency.

Several models have been developed to describe the optical breakdown and to compute the breakdown threshold. Chan *et al.* [30] proposed a model based on the energy balance of electrons neglecting their energy distribution. According to this work, breakdown occurred if the laser heating of electrons by IB induces a gain of electron energy that overcomes the energy losses. Thus, one requires a laser power density (power threshold density)

$$I_{las} \geq \frac{m\ c\ I_P}{4\pi e^2 \ln 2} \frac{\omega^2 + \nu_c^2}{\nu_c} \left[\frac{43}{\tau_p} \ln 2 + \frac{D_e}{\Lambda^2} + \frac{2m\ \langle \varepsilon \rangle\ \ln 2\ \nu_c}{M\ I_P} + (\alpha + \frac{\beta}{\Lambda^2}) \nu_c \right], \quad (2.14)$$

where m and e are the mass and charge of electrons, c is the light velocity, and I_P and M are the ionization potential and the atomic mass of the gas. The terms ω, ν_c, τ_p, D_e, Λ and $<\epsilon>$ are the laser frequency, effective electron-neutral collision frequency, laser pulse duration, diffusion coefficient, diffusion length and average electron energy, respectively. The terms α (dimensionless) and β (length^2) are two parameters, which depend on the atomic structure of the gas. The terms inside the brackets represent various loss terms. The first term in the brackets stands for the generation of 43 electrons necessary for the breakdown. The second, third, and fourth terms take into account the electron energy loss due to diffusion out of the focal volume, elastic and inelastic collisions, respectively. The loss due to electron attachment is very low and therefore, not considered in Eq. (2.14). The losses due to elastic and inelastic collisions are proportional to ν_c that increases linearly with the gas pressure p. At a low pressure, collisional loss can be neglected and electron heating by IB varies linearly with p according to $\nu_c^2 << \omega$. Thus, the threshold decreases with p in the low-pressure range. When increasing p to sufficiently high values, the collisional losses overcome the terms of electron generation and diffusion loss. If $\nu_c^2 << \omega$ still holds, both gain and loss terms are proportional to p and the threshold is pressure independent. In the high pressure range ($\nu_c^2 >> \omega$) the gain by IB diminishes as p^{-1} and the threshold increases. Thus, it exists an optimum pressure for which the optical breakdown threshold is minimum. According to Eq. (2.14), the breakdown power threshold density in general is directly proportional to the ionization potential of the gas. Moreover, the breakdown threshold passes through a minimum at the pressure at which laser angular frequency ω is equal to the effective electron-neutral collision frequency ν_c, as indicated by the term outside the brackets. Depending on their relative magnitudes, breakdown may be termed to be limited, diffusion limited or attachment limited [43].

In MPI process, from Eq. (2.5), the breakdown threshold flux intensity F_{th} is

$$F_{th} = \frac{1}{\sigma \tau_l} \left[\frac{n_{e,cr} \tau_l (n-1)!}{N_0 p \tau_p} \right]^{1/n}, \quad (2.15)$$

where $n_{e,cr}$ is the critical number density of electrons for gas breakdown (about 10^{16} electrons/cm^3), N_0 is the number of atoms in a volume of gas at pressure p of one

atmosphere, τ_l is the mean lifetime of an excited species and τ_p is the duration of laser pulse. From Eq. (2.15) the breakdown threshold flux intensity depends on gas pressure as $p^{-1/n}$.

Time-limited breakdown occurs if the first term in the brackets dominates, that is when the laser pulse duration τ_p is so short that the growth rate of electron density required to induce a visible breakdown exceeds any losses. Thus, the threshold power density varies inversely with pulse duration and the breakdown is determined by the product of the intensity times the pulse duration. Diffusion-limited processes occur when the second term in the brackets dominates, that is for the gas breakdown to take place in a small focal volume at low gas pressure. The breakdown power density threshold in this case decreases as Λ^{-2} with the focal size and it also decreases as p^{-2} with the gas pressure in the range of pressure so that $\omega >> \nu_c$. The third and fourth terms are the attachment and elastic collision loses. They are relatively unimportant and are dependent on the type and masses of the gas. For inert gases, the attachment loss can be completely neglected. The last term is the energy loss due to inelastic collision, and it should be important for molecular gases because the large number of excited states they possess. Because the attachment rate and collision frequency are assumed to be proportional to the gas pressure p, these three terms are independent of the gas pressure. At low pressure and in particular for small waist, the electron diffusion out of the focal volume is the dominating loss term. The electron diffusion length Λ can be estimated assuming a focal volume of cylindrical shape with radius $r = f \times \theta /2$ and length

$$l = \left(\sqrt{2} - 1\right)\frac{f^2\theta}{d}, \tag{2.16}$$

where f is the focal length of the focussing lens, θ the angle of laser beam divergence, and d the laser beam diameter incident on the lens. For a Gaussian laser beam, one has

$$\frac{1}{\Lambda^2} = \left(\frac{2.405}{r}\right)^2 + \left(\frac{\pi}{l}\right)^2, \tag{2.17}$$

For a large numerical opening ($\geq f/5$), Eq. (2.17) is simplified to $\Lambda = r/2.405$. Using this expression with r from Eq. (2.17) and computing the electron diffusion coefficient as

$$D_e = \frac{2\langle\varepsilon\rangle}{3m\nu_{\text{eff}}}, \tag{2.18}$$

the energy loss due to electron diffusion can be evaluated. With respect to the loss due to elastic collisions, the energy loss by diffusion can be neglected if

$$\nu_{\text{eff}} >> \frac{4.81\sqrt{I_P M}}{\sqrt{3}mf\theta}. \tag{2.19}$$

A large dispersion of breakdown threshold values exists in literature. It is attributed to the large number of parameters on which the optical breakdown depends. Several mechanisms have been found to reduce the threshold of optical breakdown. Smith and Haught [44] observed threshold lowering by Penning effect during the ruby laser breakdown in a high-pressure Ar atmosphere when adding 1% Ne. The phenomenon was due to Ar ionization by collisions with excited Ne atoms, which were produced by a resonant excitation process. However, the threshold lowering was at maximum of about 50% [44]. For CO_2 laser radiation, a resonant excitation process can be excluded because of the small photon energy and the Penning effect does not contribute to the optical breakdown threshold lowering in the far IR spectral range. For laser radiation of sufficiently high photon energy, the presence of impurities with low ionization energy lead to threshold lowering [45] attributed to multiphoton ionization. However, this effect is not observed for CO_2 laser radiation. Gas impurities with the lowest ionization potential like hydrocarbon radicals require at least the simultaneous absorption of more than 50 photons what are a process of vanishing probability. Contrarily, molecular species such as hydrocarbon or other radicals brake the ionization avalanche. They have many vibrational and rotational excitation levels, which cause electron energy loss by inelastic collisions.

Several authors [46,47] reported threshold lowering when initiating the breakdown by ablation of a solid target. A threshold reduction by a factor of 10^2 was observed for CO_2 laser radiation [46]. The threshold lowering was explained by shock wave generation as an effect of strong material ablation. The shock wave heats up the surrounding gas which is instantaneously transformed in a strongly ionized plasma. The optical breakdown from solid material ablation has been shown to be a multistage plasma initiation process that is characterized by three thresholds [47]: (i) the material ablation threshold I_{vap}; (ii) the breakdown threshold of the evaporated material I_{vap}^*; and (iii) the breakdown threshold of the surrounding gas I_{gas}^*. It is noted that I_{vap}* and I_{gas}^* are the thresholds of preionized vapour and gas, respectively. For the case of CO_2 laser ablation, the initial ionization stage of the ablated material vapour is $n_e/n_{vap}<10^{-5}$-10^{-4} [47], n_{vap} being the ablated material vapor density. As a consequence of preionization, the number of electron generations necessary for complete ionization is strongly reduced (<<43). Thus, the electron generation term can be neglected in Eq. (2.14). The diffusion loss can be also neglected according to the relative large volume preionized by the shock wave. In the case of rare gases, the loss by inelastic collisions is much smaller than that due to elastic collisions and the avalanche ionization is determined by the balance between IB heating of electrons and losses by elastic collisions. The breakdown threshold (in $W\times cm^{-2}$) given by Eq. (2.14) is simplified to [47].

2.2.4 Laser-Plasma Interaction

The interaction between the laser radiation and the free electrons of the plasma is described by the Drude model considering the electron motion in the laser field as a harmonic oscillator. For collision frequencies $\omega_P^2>>\nu_c^2$, where ω_P is the plasma frequency, the dielectric constant is given by $\epsilon \approx 1 - \omega_P^2/\omega^2$, where ω is the laser frequency. Optical breakdown in gases at the atmospheric pressure leads to an electron density equal to the critical density. In the region where the critical density is reached,

the plasma frequency is equal to the laser frequency and n=0. The plasma is thus completely reflecting in the corresponding zone. Only a few authors have investigated the laser beam reflection by the plasma. In fact, the studies show that breakdown plasmas reaching the critical density absorb most of the incident laser energy [48-50]. The fraction of reflected radiation is small because of strong absorption in the zone next to the plasma sheet of critical density. Donaldson *et al.* [49] showed that 80% of incident laser energy is absorbed in a zone of weak thickness where the electronic density vary from 0.83 $n_{e,cr}$ to $n_{e,cr}$, when generating breakdown with a (Nd:YAG) laser of τ_p=35 ps and I_W=10^{14} W×cm^{-2}. Offenberger and Burnett [48] measured the reflected and transmitted power of TEA-CO_2 laser pulses during the breakdown in hydrogen. The reflected power is always below 2% of the incident laser power. The major absorption mechanism of CO_2 laser radiation during breakdown ignition is electron-neutral IB. Once strongly ionized plasma is formed, the electron impact ionization or electron-ion IB dominates due to the long range Coulomb interaction between charged particles.

Several experimental and theoretical studies have been performed to investigate the IB effect. The IB process involves the absorption of photons by free electrons, which gain energy from the laser beam during collisions with neutral and ionized atoms, thus promoting vapour ionization and excitation through electron collisions with excited- and ground-state neutrals. IB due to electron–neutral interaction is usually one or two orders of magnitude smaller than that due to electron–ion interaction when the ion density is high. Nevertheless, the electron-neutral interaction can be of importance in weakly ionized vapours. However, in this last case the vapour behaves like a thin medium and the absorption is very low. Among numerous expressions for the determination of the IB absorption coefficient [2,5] the formula

$$\alpha_{IB} = 3.69\times10^{8}\,\frac{n_e^2\sum_i f_i Z_i^2}{\sqrt{T_e}\,\nu^3}\left(1-e^{-h\omega/2\pi k_B T}\right), \qquad (2.20)$$

proposed by Spitzer [51] is used by many authors to estimate the laser energy absorption by the plasma. Here, T_e and n_e are in K and cm^{-3}, respectively. The factors f_i are the fractional abundances of ions, Z_i the corresponding ion charge. Equation (2.20) shows that the IB process is less efficient in the UV than in the visible and IR part of the light spectrum. Nevertheless, the IB absorption coefficient depends both on the vapour/plasma degree of ionization and on the effectiveness of the vaporization process. Thus, the actual effectiveness of the IB absorption process results from several factors, which involve the target thermo-physical properties and the interaction of the laser beam with the evaporated species (i.e. the ionization potential and electronic structure of the evaporated atoms). In particular, electrons generated by both MPI and electron impact ionization can participate in the IB absorption process. However, electrons directly evaporated from the target can give an effective contribution to IB absorption in the early stages of the laser–target interaction.

In the case of CO_2 laser radiation, one has $(1 - e^{-h\omega/2\pi kT}) \approx h\omega/2\pi kT$ and Eq. (2.20) simplifies for singly ionized plasma to

$$\alpha_{\mathrm{IB}} = 1.8 \times 10^{-35} \frac{n_e^2}{T_e^{3/2}}, \tag{2.21}$$

where α_{IB} is in cm^{-1} and T_e is in eV. This equation shows that the efficiency of IB absorption decreases with increasing electron temperature. At high plasma temperatures, other absorption mechanisms dominate. These have been made in evidence during studies of laser-plasma interaction related to thermonuclear fusion using power densities several orders of magnitude higher than breakdown thresholds. In IR laser-ablation processes, primary electrons coming from vaporization are able to absorb laser photons by IB even at very low electron density. For example, at the CO_2 laser wavelength α_{IB} can be higher than 10^{-19} cm^{-2} at very low plasma temperature and electron density. At a laser intensity of 10^7 W cm^{-2}, the product of cross section and photon flux gives a probability of ≈ 50% for an IB photon absorption in 10 ns. This leads to strong electron heating and breakdown ionization even at very low laser intensity. Due to this high absorption of infrared radiation into the nascent laser plasma, it is not possible to efficiently couple energy to the target and the ablated vapour density and ablation depth remain low even at higher laser intensity [47]. In visible and UV laser-ablation processes, IB absorption is less efficient, but direct MPI of excited atoms in the vapour can play a significant role.

2.2.5. Absorption wave Propagation

After breakdown ignition, the strongly absorbing plasma will propagate in the direction opposite to the laser beam. The absorption wave formation has been observed in many experiments using CO_2 laser sources [46]. The theoretical analyses of optical breakdown and absorption wave propagation performed by Raizer [2] using a hydrodynamic model have been widely accepted and became a standard theory in the field. According to this model, the laser-induced absorption waves propagate by the following stepwise mechanisms: (i) A small plasma zone is heated up by the laser beam. It reaches the critical density and strongly absorbs the laser radiation. (ii) The electron density in the adjacent zones increases. (iii) The adjacent preionized zone that is irradiated by the laser beam is heated up and becomes absorbent. Thus, the strongly absorbing plasma zone propagates in the direction opposite to the laser beam.

Three different propagation modes are distinguished. The breakdown wave is characterized by the following propagation mechanism:

(i) breakdown initially occurs in the region of the highest laser power density and later in the zones of lower power density. The expansion of high pressure plasma compresses the surrounding gas and drives a shock wave. Thus, the breakdown propagates in the direction opposite to the laser beam. The plasma also tends to expand back along the beam path toward the laser, a phenomenon known as moving breakdown. The velocity of the breakdown wave is given by

$$\mathrm{v_{bw}} = \frac{w_0}{\tau_p \ \mathrm{tg}\varphi}, \tag{2.22}$$

where w_0 and φ are the minimum radius and opening angle of the focused laser beam, respectively. For example, for our typical experimental conditions with the CO_2 laser, taking w_0=0.05 cm, τ_p=100 ns and tgφ=0.2, the breakdown wave propagates with $v_{bw}=2.5\times10^6$ cm/s;

(ii) Propagation through the detonation wave mechanisms occurs when rapid heating of the gas in the region of strong absorption induces a spherical shock wave. The latter propagates into the surrounding gas that is heated and preionized. The part of the preionized gas that is further illuminated by the laser beam absorbs the laser radiation and becomes opaque. Thus, the absorption zone follows the shock wave. The propagation velocity of the detonation wave is given by

$$v_{bw} = \left[2\left(\gamma^2 - 1\right)\frac{I_W}{\rho_0} \right]^{1/3}, \tag{2.23}$$

where γ and ρ_0 are respectively, the adiabatic constant of the gas and the specific mass. The specific energy that is injected into the gas is

$$\varepsilon_{bw} = \frac{\gamma}{\left(\gamma^2 - 1\right)\left(\gamma + 1\right)} v_{bw}^2 . \tag{2.24}$$

It is noted that detonation wave propagation velocity and injected specific energy are independent of the atomic structure of the gas. The gas influences the detonation wave propagation only through its specific mass and adiabatic constant. Thus, a change of gas nature is equivalent to a pressure variation if γ is unchanged. Consequently, the detonation wave propagation velocity in Ar is equal to that in Xe at three times a lower pressure. For Xe at atmospheric pressure and $I_W=10^8$ W cm^{-2}, the detonation wave propagates with a velocity of 6×10^5 cm s^{-1} and heats up the gas to a temperature of 28 eV. The temperature is obtained by assuming an ideal gas, for which the specific energy is related to the temperature by $\epsilon_{bw}=(3/2)\, k_B\, T\, N_A/M$. Here, k_B, T, N_A and M are Boltzmann's constant, plasma temperature, Avogadro's constant and mass, respectively.

(iii) For $I_W>10^{10}$ Wcm^{-2}, the plasma is heated up to $T<10^2$ eV. According to the high temperature, the plasma strongly radiates in the UV and soft X-ray spectral range ionizing thus the surrounding gas. Once preionized, the gas in the zone illuminated by the laser beam absorbs the laser radiation and a laser sustained radiation wave propagates in the direction opposite to the laser beam. The dominating propagation mechanism of the absorption wave depends on the experimental conditions. Breakdown waves are formed in the case of very small opening angle of the focused laser beam, whereas radiation waves occur at very high laser power density. For moderate power density and sufficiently wide opening angle, the optical breakdown propagates as a detonation wave.

A portion of the laser pulse energy is absorbed by the expanding plasma generating three different types of waves: (i) laser-supported combustion (LSC) waves; (ii) laser-supported detonation (LSD) waves; and (iii) laser-supported radiation (LSR) waves [40]. They differ in their predictions of opacity and energy transfer properties of

the plasma to the surrounding gas. At low-power laser regime (I_W<1 MW/cm^2), LSC waves are produced, which comprise of a precursor shock, that is separated from the absorption zone and the plasma. The shock wave results in an increase in the ambient gas density, temperature and pressure, whereas the shock edges remain transparent to the laser light. At medium-power laser regime (1 MW/cm^2< I_W <4 GW/cm^2), the precursor shock is sufficiently strong and the shocked gas is hot enough to begin absorbing the laser radiation without requiring additional heating by energy from the plasma. The laser absorption zone follows directly behind the shock wave and moves at the same velocity. In this case, a LSD wave is produced and has been modelled by several authors [2-3]. The propagation of the LSD wave is controlled by the absorption of the laser energy. At high-power laser regime (I_W >4 GW/cm^2), the plasma is so hot that, prior to the arrival of the shock wave, the gas it heated to temperatures at which laser absorption begins. Laser radiation is initiated without any density change and the pressure profile results, mainly from the strong local heating of the gas rather than from propagating shock wave. The LSR wave velocity increases much more rapidly with irradiance than those of the LSC and LSD waves.

2.3. Laser-Ablation plasmas

The interest in laser-ablation plasmas is due to the fact that both fundamental aspects of laser-solid interaction and consequent plasma generation, and applied techniques in material processing technology and sample elemental analysis are involved. In particular, plasmas evaporated by irradiating solid targets with nanosecond laser pulses are widely used for the deposition of thin solid films, and the technique has been applied successfully to a wide range of materials [52]. In the analysis of laser-ablation processes it is useful to consider that laser light absorption and the resulting simultaneous target heating, vaporization and plasma formation take place much faster than the expansion of the ablated material [53]. Under these assumptions the laser-ablation process can be divided schematically into two stages: (i) Evaporation of the solid target and formation of the laser plasma; (ii) Expansion of the ablated vapor cloud in vacuum or into a background gas.

The interaction of high-intensity laser pulses with a solid target involves laser-solid interaction and plasma formation. When the process occurs at low laser irradiance, the vapor produced by the laser pulse behaves like a thin medium and the laser beam passes nearly unattenuated through the vapor. At high laser irradiance, the vapor temperature is high and atomic excitation and ionization are produced. In this case the vapor absorbs the incident laser radiation leading to breakdown and plasma formation. At low fluences, the main physical processes involve heat conduction, melting and vaporization of the target. At high energies, the plasma density can be so high that an efficient shielding of the target occurs. In this case the properties of the laser-ablation process are influenced by both laser-plasma interaction and plasma dynamics. Laser ablation with femtoand and picosecond laser pulses can be considered as a direct solid-vapor transition, due to the fact that at very short time scales thermal conduction into the target can be neglected. On the contrary, in nanosecond laser ablation of solids, the absorbed laser energy first heats up the target to the melting point and then to the vaporization temperature. In this case evaporation occurs from the liquid metal, and heat

conduction into the solid target is the main source of energy loss. The vaporization process can be described by using the one-dimensional heat flow equation,

$$\rho.c\frac{\partial T}{\partial t}=\frac{\partial T}{\partial z}\left(k\frac{\partial T}{\partial z}\right)+\alpha A I_0\exp(-\alpha z)\,, \tag{2.25}$$

where T, ρ, c, k and A are temperature, mass density, specific heat, thermal conduction and surface absorbance of the target, respectively and z is the coordinate normal to the target surface. In this equation α and I_0 are the laser absorption length and the intensity of the incident laser pulse. An exact solution of this equation is very difficult to find by considering the nonlinear boundary condition for vaporization and the presence of a moving solid-liquid interface. Consequently, numerical approaches are always considered. To estimate the order of magnitude of the laser fluence threshold for vaporization, simple approximated energy balance considerations can be applied. For nanosecond laser pulses and metallic targets, the heat penetration depth L_{th} fulfills the condition $L_{th}>>1/\alpha$, being $L_{th}\approx(2\ D\ \tau_p)^{1/2}$ where $D=k/\rho\ c$ is the heat diffusion coefficient. Then, the absorbed energy is stored in a layer with a thickness of the order of L_{th} because there is enough time for thermal wave propagation into the target. For metals, it is necessary much more energy to vaporize than to melt and evaporation occurs when the energy per unit volume absorbed into the vaporized layer becomes larger than the latent heat of evaporation per unit volume. The minimum energy above which appreciable evaporation occurs F_{th} is given approximately by the energy needed to melt a surface layer of the order of L_{th}:

$$F_{th}=\frac{\rho\ c(T_m-T_0)L_{th}}{A}\,, \tag{2.26}$$

where T_m and T_0 are the melting and initial target temperature, respectively. The fluence threshold grows as $(\tau_P)^{1/2}$ and depends on the thermal and optical properties of the target.

3. LIB PLASMA ANALYSIS

In contrast to conventional spectroscopy, where one is mainly concerned with the structure of an isolated atom and molecule, the radiation from the plasma also depends on the properties of the plasma in the intermediate environment of the atomic or molecular radiator. This dependence is a consequence of the long-range Coulomb potential effects which dominate the interactions of ions and electrons with each other and with existing neutral particles. These interactions are reflected in the characteristic radiations in several ways. They can control population densities of the discrete atomic states, spectral shift and broadening by Stark effect, decrease of ionization potentials of the atomic species, cause continuum radiation emissions and emission of normally forbidden lines. Generally, the radiation emitted from self-luminous plasma can be divided into bound-bound, bound-free, and free-free transitions.

3.1. Local Thermodynamic Equilibrium (LTE)

Plasma description starts by trying to characterize properties of the assembly of atoms, molecules, ions and electrons rather than individual species. If thermodynamic equilibrium exits, then plasma properties can be described through the concept of temperature. Thermodynamic equilibrium is rarely complete, so physicists have settled for a useful approximation, local thermodynamic equilibrium (LTE). In LTE model, it is assumed that the distribution of population densities of the electrons is determined exclusively through collisional processes and that they have sufficient high rate constants so that the distribution responds instantaneously to any change in the plasma conditions. In such a circumstances each process is accompanied by its inverse and these pairs of processes occur at equal rates by the principle of detailed balance. Thus, the distribution of population densities of the electrons energy levels is the same as it would be in a system in complete thermodynamic equilibrium. The population distribution is determined by the statistical mechanical law of equipartition among energy levels and does not require knowledge of atomic cross sections for its calculation. Thus, although the plasma density and temperature may vary in space and time, the distribution of population densities at any instant and location in space depends entirely on local values of density, temperature, and chemical composition of plasma. If the free electrons are distributed among the energy levels that are available for them, their velocities have a Maxwellian distribution

$$dn_{\mathrm{v}} = n_e 4\pi \left(\frac{m}{2\pi k_B T_e} \right)^{3/2} \exp\left(-\frac{m\ \mathrm{v}^2}{2k_B T_e} \right) \mathrm{v}^2 d\mathrm{v}, \tag{3.1}$$

where n_e is the electron density, m is the electron mass, k_B is the Boltzmann constant, T_e is the electron temperature and v is the electron velocity. For the bound levels the distributions of population densities of neutrals and ions are given by the Boltzmann (3.2) and Saha (3.3) equations

$$\frac{N_j}{N_i} = \frac{g_j}{g_i} \exp\left(-\frac{(E_{\mathrm{j}} - E_i)}{k_B T_e} \right), \tag{3.2}$$

$$\frac{N_{z+1,k} n_e}{N_{z,k}} = \frac{g_{z+1,k}}{g_{z,k}} 2 \left(\frac{2\pi\ m\ k_B\ T_e}{h^2} \right)^{3/2} \exp\left(-\frac{I\mathrm{p}_{\mathrm{z,k}}}{k_B T_e} \right), \tag{3.3}$$

where N_{i}, N_{j}, $N_{\mathrm{z+1,k}}$ and $N_{\mathrm{z,k}}$ are the population densities of various levels designated by their quantum numbers j (upper), i (lower) and k (the last for the ground level) and ionic charge z and z+1. The term $g_{\mathrm{z,i}}$ is the statistical weight of the designated level, E_{j} and E_{i} are the energy of the levels j and i and $Ip_{\mathrm{z,k}}$ is the ionization potential of the ion of charge z in its ground level k. Equations (3.1)-(3.3) describe the state of the electrons in an LTE plasma. For complete LTE of the populations of all levels, including the ground state, a necessary condition is that electron collisional rates for a given transition exceed the corresponding radiative rates by about an order of magnitude [54]. This condition gives a criterion [55] for the critical electron density of the level with energy $\Delta E = E_{\mathrm{j}} - E_{\mathrm{i}}$

$$n_{\mathrm{e,cr}} \geq \frac{5}{8\sqrt{\pi}}\left(\frac{\alpha}{a_0}\right)^3 z^7\left(\frac{\Delta E}{z^2 E_{\mathrm{H}}}\right)^3\sqrt{\left(\frac{k_{\mathrm{B}}T_{\mathrm{e}}}{z^2 E_{\mathrm{H}}}\right)} \cong 1.6\times10^{12}\, T_{\mathrm{e}}^{1/2}(\Delta E)^3, \tag{3.4}$$

where α is fine-structure parameter, a_0 is Bohr radius, and E_{H} is the hydrogen ionization potential. In the numerical relationship of Eq. (3.4), $n_{\mathrm{e,cr}}$ is given in cm^{-3}, T_{e} in K and ΔE (energy difference between the two neighboring states) in eV. Many plasmas of particular interest do not come to close to complete LTE, but can be considered to be only in partial thermodynamic equilibrium in the sense that the population of sufficiently highly excited levels are related to the next ion's ground state population by Saha-Boltzmann relations, respective to the total population in all fine-structure levels of the ground state configuration [54]. For any atom or ion with simple Rydberg level structure, various criteria were advanced for the minimum principal quantum number n_{c} for the lowest level, often called thermal or collision limit, for which partial thermodynamic equilibrium remains valid to within 10%. One criterion with quite general validity is given by Griem [55]:

$$n_{e,cr} \approx \left[\frac{10\, z^7}{2\sqrt{\pi}\, n_c}\left(\frac{\alpha}{a_0}\right)^3\right]^{2/17}\left(\frac{k_B T_e}{z^2 E_H}\right)^{1/17} \approx 7\times10^{18}\, z^6 n_c^{\,-17/2}\frac{k_B T_e}{E_H}. \tag{3.5}$$

3.2 Line Radiation and Continuum radiation

Line radiation from plasma occurs for electron transitions between the discrete or bound energy levels in atoms, molecules or ions. In an optically thin plasma of length l along the line of sight [56], the integrated emission intensity I_{ji} of a spectral line arising from a transition between bound levels j and i is given by

$$I_{ji} = \frac{A_{ji} h\nu_{ji}}{4\pi}\int N_j ds = h\nu_{ji} A_{ji} N_j l, \tag{3.6}$$

where N_{j} is the population density of the upper level j, $h\nu_{\mathrm{ji}}$ is the photon energy (energy difference between levels j and i), and A_{ji} is the spontaneous transition probability or Einstein A coefficient. The integration is taken over the depth of plasma viewed by the detector, and the intensity of radiation is measured in units of power per unit area per unit solid angle. Transition probabilities can be sometimes expressed via the oscillator strength f_{ji}. This is defined as the ratio of the number of classical oscillators to the number of lower state atoms required to give the same line-integrated absorption [57]. Its relationship to the Einstein coefficient is

$$f_{ji} = \frac{4\pi\varepsilon_0}{e^2}\frac{mc^3}{8\pi^2\nu_{ji}}\frac{g_j}{g_i}A_{ji}. \tag{3.7}$$

The usefulness of f_{ji} is that it is dimensionless, describing just the relative strength of the transition. The detailed values of A_{ji} , g_{i}, and g_{j} can be obtained from reference compilations or from electronic databases, i.e by NIST [58].

The origins of continuum radiation are both bound-free and free-free transitions. Free-free emission or IB radiation is due to the interaction of free electrons with positively charged ions. In free-bound emission (recombination radiation), a free electron is captured by an ion in a bound level. The energy of the given off photon is the difference between original energy of the electron and its new energy in whatever level of whatever atom it ends up. Since this difference may have any value, the result of many free-bound transitions is a continuous spectrum. Transitions between two free energy levels can occur in plasmas increasing the energy exchanges of charged particles. Classically, this takes place because a moving charge radiates when it is accelerated or retarded. For most cases of practical importance, these free-free transitions are classified as bremsstrahlung or cyclotron spectra. In bremsstrahlung, the acceleration of charged particle takes place via the Coulomb field of charged particles. In cyclotron radiation, the acceleration is due to the gyration of charged particles in a magnetic field. The total continuum radiation at any particular frequency $I(\nu)$ is the sum of the contributions from all such processes having components at the specified frequency. Thus

$$I(\nu)d\nu = \frac{1}{4\pi}\int n_e \sum_i N_i \left[\gamma(i, T_e, \nu) + \sum_p \alpha(i, j, T_e, \nu) \right] h\nu \; ds \; d\nu \,, \tag{3.8}$$

where $\gamma(i, T_e, \nu)$ is the atomic probability of a photon of frequency ν being produced in the field of an atom or ion (specified by i) by an electron of mean kinetic temperature T_e making free-free transition; $\alpha(i, j, T_e, \nu)$ is the corresponding probability where the electron makes a free-bound transition into a level j. As before, the integration is taken over the plasma depth s.

3.3. Line Broadening; Determination of Electron Number Density from Stark Broadening of Spectral Lines

The shape of the spectral lines in the LIB has been studied since the first observation of the laser-induced breakdown in early 1960s. It plays an important role for the spectrochemical analysis and quantification of the plasma parameters. The observed spectral lines are always broadened, partly due to the finite resolution of the spectrometers and partly to intrinsic physical causes. In addition, the center of the spectral lines may be shifted from its nominal central wavelength. The principal physical causes of the spectral line broadening are the Doppler, resonance pressure, and Stark broadening. There are several reasons for this broadening and shift. These reasons may be divided into two broad categories: broadening due to local conditions and broadening due to extended conditions. Broadening due to local conditions is due to effect which hold in a small region around the emitting element, usually small enough to assure LTE. Broadening due to extended conditions may result from changes in the spectral distribution of the radiation as it traverses its path to the observer. It also may result from the combining of radiation from a number of regions, which are far from each other.

The uncertainty principle relates the lifetime of an excited state (due to the spontaneous radiative decay) with the uncertainty of its energy. This broadening effect produces an unshifted Lorentzian profile. The FWHM of natural broadening for a transition with a natural lifetime of τ_{ji} is: $\Delta\lambda^{N}_{FWHM}=\lambda^2/\pi c\tau_{ji}$. The natural lifetime τ_{ji} is dependent on the probability of spontaneous decay: $\tau_{ji}=1/A_{ji}$. Natural broadening is usually very small compared with other causes of broadening.

The Doppler broadening is due to the thermal motion of the emitting atoms, molecules or ions. The atoms in a gas which are emitting radiation will have a distribution of velocities. Each photon emitted will be "red" or "blue" shifted by the Doppler effect depending on the velocity of the atom relative to the observer. The higher the temperature of the gas, the wider the distribution of velocities in the gas. Since the spectral line is a combination all of the emitted radiation, the higher the temperature of the gas, the broader will be the spectral line emitted from that gas. This broadening effect is described by a Gaussian profile and there is no associated shift. For a Maxwellian velocity distribution the line shape is Gaussian, and the FWHM may be estimated as (in Å):

$$\Delta\lambda^{D}_{FWHM} = 7.16\times10^{-7}\cdot\lambda\cdot\sqrt{T/M}\ , \tag{3.9}$$

being λ the wavelength in Å, T the temperature of the emitters in K, and M the atomic mass in amu.

The presence of nearby particles will affect the radiation emitted by an individual particle. There are two limiting cases by which this occurs: (i) Impact pressure broadening: The collisions of other particles with the emitting particle interrupt the emission process. The duration of a collision is much shorter than the lifetime of the emission process. This effect depends on both the density and the temperature of the gas. The broadening effect is described by a Lorentzian profile and there may be an associated shift. (ii) Quasistatic pressure broadening: The presence of other particles shift the energy levels in the emitting particle, thereby altering the frequency of the emitted radiation. The duration of the influence is much longer than the lifetime of the emission process. This effect depends on the density of the gas, but is rather insensitive to temperature. The form of the line profile is determined by the functional form of the perturbing force with respect to distance from the perturbing particle. There may also be a shift in the line center. Pressure broadening may also be classified by the nature of the perturbing force as follows: (i) *Linear Stark broadening* occurs via the linear Stark effect which results from the interaction of an emitter with an electric field, which causes a shift in energy which is linear in the field strength ($\sim E$ and $\sim 1/r^2$); (ii) *Resonance broadening* occurs when the perturbing particle is of the same type as the emitting particle, which introduces the possibility of an energy exchange process ($\sim E$ and $\sim 1/r^3$); (iii) *Quadratic Stark broadening* occurs via the quadratic Stark effect which results from the interaction of an emitter with an electric field, which causes a shift in energy which is quadratic in the field strength ($\sim E$ and $\sim 1/r^4$); (iv) *Van der Waals broadening* occurs when the emitting particle is being perturbed by Van der Waals forces. For the quasistatic case, a Van der Waals profile is often useful in describing the profile. The energy shift as a function of distance is given in the wings by e.g. the Lennard-Jones potential ($\sim$E and $\sim 1/r^6$).

Stark broadening of spectral lines in the plasma occurs when an emitting species at a distance r from an ion or electron is perturbed by the electric field. This interaction is described by the Stark effect. The linear Stark effect exists for hydrogen and for all other atoms. Stark broadening from collisions of charged species is the primary mechanism influencing the emission spectra in LIBS. Stark broadening of well-isolated lines in the plasma can be used to determine the electron number density $n_e(cm^{-3})$. In the case of a non-H-like line, an estimation of the Stark width (FWHM) and line shift of the Stark broadened lines is given as [54-57]:

$$\Delta\lambda_{\mathrm{FWHM}}^{\mathrm{Stark}} = 2W\left(\frac{n_e}{10^{16}}\right) + 3.5A\left(\frac{n_e}{10^{16}}\right)^{1/4}\left(1 - BN_D^{-1/3}\right) W\left(\frac{n_e}{10^{16}}\right), \tag{3.10}$$

$$\Delta\lambda^{\mathrm{Shift}} = D\left(\frac{n_e}{10^{16}}\right) \pm 2A\left(\frac{n_e}{10^{16}}\right)^{1/4}\left(1 - BN_D^{-1/3}\right) W\left(\frac{n_e}{10^{16}}\right), \tag{3.11}$$

where W is the electron impact parameter or half-width, A is the ion impact parameter both in Å, B is a coefficient equal to 1.2 or 0.75 for ionic or neutral lines, respectively, D (in Å) is the electron shift parameter and N_D is the number of particles in the Debye sphere $N_D=1.72\times10^9 T^{3/2} n_e^{-1/2}$. The electron and the ion impact parameters are functions of temperature. The first term on the right side of Eq. (3.10) refers to the broadening due to the electron contribution, whereas the second one is the ion broadening. The minus sign in Eq. (3.11) applies to the high-temperature range of those few lines that have a negative value of D/W at low temperatures. Since for LIB conditions Stark broadening is predominantly by electron impact, the ion correction factor can safely be neglected, and Eq. (3.10) becomes

$$\Delta\lambda_{\mathrm{FWHM}}^{\mathrm{Stark}} \approx 2W\left(\frac{n_e}{10^{16}}\right). \tag{3.12}$$

The coefficients W are independent of n_e and slowly varying functions of electron temperature. A comprehensive list of width and shift parameters W, A and D is given by Griem [55]. In the quasi-static approximation, the interaction between slowly moving ions and radiating species can be approximated by a perturbation which remains nearly constant over the whole time that the species are radiating. Hydrogen and hydrogen-like ions exhibits linear Stark effect. The FWHM (in Å) of a hydrogen or H-like ion spectral line, in the quasi-static approximation, is given by [54,55]

$$\Delta\lambda_{\mathrm{FWHM}}^{\mathrm{Stark}} = 8.16\times10^{-19}\left(1 - 0.7N_D^{-1/3}\right)\lambda_0^2(n_2^2 - n_1^2)(Z_p^{1/3} - Z_e)n_e^{2/3}, \tag{3.13}$$

where λ_0 is the wavelength line centre, n_2 and n_1 are the principal quantum numbers of the upper and lower states, respectively, Z_p and Z_e are the nuclear charge on the perturbing ion and the emitting species (atom or ion) and n_e is the electron number density in cm^{-3}. Although the line shapes do depend on the electron contribution, the FWHM are generally insensitive. Eq. (3.13) represents a very good estimate of the Stark broadening in those hydrogenic lines that have not a strong undisplaced Stark component as for example L_β, L_δ, H_β (Balmer) and H_δ transitions. On the other hand, the

FWHM of hydrogenic lines with strong central Stark components are dominated by interactions of the electrons with the emitting hydrogenic species such as L_α and H_α transitions. Such lines have a Lorentzian line shape and the FWHM for L_α transition in the impact approximation is given by

$$\Delta\lambda_{\mathrm{FWHM}}^{\mathrm{Stark}} \approx 1.62\times10^{-17}\,\frac{n_{\mathrm{e}}}{\sqrt{T}}\left(13.76-\log\frac{n_e^{1/2}}{T}\right), \tag{3.14}$$

where $\Delta\lambda_{\mathrm{FWHM}}^{\mathrm{Stark}}$ is in Å, T is in K and n_{e} is in cm^{-3}. It is seen from Eqs. (3.13) and (3.14) that the ion broadening, in the quasi-static approximation, varies as $n_{\mathrm{e}}^{2/3}$ and is independent of the temperature whereas the collisional broadening varies approximately as n_{e} and it is very much temperature dependent. It is to be noted the electron densities determined from Eqs. (3.13) and (3.14) are only crude estimations and one must compute the entire line profile to extract the total line width for an accurate estimation of n_{e}.

3.4. Determination of Excitation Temperature

The excitation temperature T_{exc} can be calculated according to the Boltzmann equation under the assumption of LTE (Section 3.1). The significance of this temperature depends on the degree of equilibrium within the plasma. For plasma in LTE, any point can be described by its local values of temperature, density, and chemical composition. By considering two lines λ_{ji} and λ_{nm} of the same species, characterized by different values of the upper energy level ($E_{\mathrm{j}}\neq E_{\mathrm{n}}$), the relative intensity ratio can be used to calculate the plasma excitation temperature

$$T_{\mathrm{exc}}=\frac{E_j-E_n}{k_{\mathrm{B}}\ln\left[\dfrac{I_{nm}\cdot\lambda_{nm}\cdot g_j\cdot A_{ji}}{I_{ji}\cdot\lambda_{ji}\cdot g_n\cdot A_{nm}}\right]}. \tag{3.15}$$

When selecting a line pair, it is advisable to choose two lines as close as possible in wavelength and as far apart as possible in excitation energy. This is to limit the effect of varying the spectral response of the detection system. The use of several lines instead of just one pair leads to greater precision of the plasma excitation temperature estimation. In fact, though the precision of the intensity values can be improved by increasing the signal intensity, the transition probabilities A_{ji} reported in the literature exhibit significant degree of uncertainty (5-50%). The excitation temperature can be calculated from the relative intensities of a series of lines from different excitation states of the same atomic or ionic species from the slope of the Bolztmann plot $\ln[I_{\mathrm{ji}}\cdot\lambda_{\mathrm{ji}}/g_{\mathrm{j}}\cdot A_{\mathrm{ji}}]$ versus $E_{\mathrm{j}}/k_{\mathrm{B}}$

$$\ln\left[\frac{I_{ji}\cdot\lambda_{ji}}{g_j\cdot A_{ji}}\right]=C-\frac{E_j}{k_{\mathrm{B}}\cdot T_{\mathrm{exc}}}, \tag{3.16}$$

where I_{ji} is the emissivity (W m^{-3} sr^{-1}) of the emitted $j \rightarrow i$ spectral line, λ_{ji} is the wavelength, $g_j=2J_j+1$ is the statistical weight, A_{ji} is the Einstein transition probability of spontaneous emission, E_j/k_B is the normalized energy of the upper electronic level and $C=\ln(hcN_j/4\pi Q(T))$ ($Q(T)$ is the partition function). The values of the λ_{ji}, g_j, A_{ji} and E_i for selected atomic or ionic lines can be obtained from the NIST Atomic Spectral Database [58]. A set of selected spectral lines can be chosen based on their relative strengths, accuracies and transition probabilities.

3.5. Ionization Degree of the Plasmas: Saha Equation

In plasma there is a continuous transition from gases with neutral atoms to a state with ionized atoms, which is determined by an ionization equation. The transition between gas and plasma is essentially a chemical equilibrium, which shifts from the gas to the plasma side with increasing temperature. Let us consider the first three different ionization equilibria of an atom A with successive ionization potentials (IP): $A \leftrightarrow A^+ + e + I\text{P}(A\text{-I})$, $A^+ \leftrightarrow A^{2+} + e + I\text{P}(A\text{-II})$, $A^{2+} \leftrightarrow A^{3+} + \text{e} + I\text{P}(A\text{-III})$. For each ionization equilibrium, considering the atoms and ions in their ground electronic state, the LTE between ionization and recombination reactions at temperature T is described by the Saha equation

$$\frac{n_e \cdot N_i}{N_0} = \frac{g_e \cdot g_i}{g_0} \frac{\left(2\pi\ m\ k_B T\right)^{3/2}}{h^3} e^{-I_P/k_B T}, \tag{3.17}$$

where $n_e = N_i$ are the electron and ion densities in the different ionization equilibria in the second member of ionization equilibria. From this equation, ionization degree $n_e \cdot N_i/N_0$ can be estimated.

3.6. Laser parameters and focal properties

The variables that can influence the LIBS measurements are mainly the laser parameters (wavelength, energy, pulse duration, shot-to-shot energy fluctuations etc), focal properties, ambient conditions, physical properties of the sample and the detection window (delay time and gate width). Below we describe some parameters that affect the precision and accuracy of LIBS.

In LIBS a high-power laser is used to ablate or to breakdown a gaseous sample in the form of plasma. The primary energy related parameters influencing the laser-gas interaction are the laser peak power P_W (or radiant pulse energy per time, in W) and the laser peak intensity I_W (power density or irradiance; energy per unit area and time, W cm^{-2}) given by

$$P_W = E_W / \tau_{FWHM}, \tag{3.18}$$

$$I_W = P_W / \pi r^2, \tag{3.19}$$

where E_W (in J) is the pulse energy, τ_{FWHM} (in s) is the pulse duration at the FWHM and πr^2 is the focal spot area (cm^2). The fluence Φ_W (in J cm^{-2}) on the focused spot area, the photon flux density F_{ph} (photon cm^{-2} s^{-1}), electric field F_E (V cm^{-1}) and pressure radiation p_R (Pa) are given by

$$\Phi_W = E_W / \pi r^2 , \tag{3.20}$$

$$F_{ph} = I_W \lambda / hc , \tag{3.21}$$

$$F_E = \sqrt{I_W / c\varepsilon_0} , \tag{3.22}$$

$$p_R = 2I_W / c , \tag{3.23}$$

where λ is the laser wavelength, h is the Planck constant, c is the speed of light, and ε_0 is the electric constant. In the equation (3.23) we suppose that the laser radiation is totally reflected and therefore the pressure radiation can be doubled. The laser peak intensity I_W, fluence, photon flux and electric field are inversely proportional to the focused spot area. For LIBS, the peak intensity I_W (and the other properties Φ_W, F_{ph}, F_E and P_R) that can be delivered to the sample is more important than the absolute value of the laser power. For the formation of plasma, the laser fluence needs to exceed the threshold value, typically of the order of several J×cm^{-2} for a nanosecond laser pulse [59]. If the laser energy is very close to the breakdown threshold, the pulse-to-pulse fluctuations can cause the plasma condition to be irreproducible, which results in poor measurement precision. The intensities of the emission lines are proportional to the laser energy while the laser plasma is in the optical thin region. When the laser energy increases further, it produces very dense and hot plasma that can absorb laser energy. This will lead to an increase in the continuum emission and a decrease in the signal intensity. Besides, the laser pulse duration and the shot-to-shot fluctuations can also affect the signal reproducibility and hence LIBS precision.

The laser power density at the focal volume is inversely proportional to the focused spot size. For a laser beam with a Gaussian profile, the focused beam waist w_0 is given by [60]

$$w_0 = \frac{\lambda f}{\pi w_s} , \tag{3.23}$$

where f is the focal length of the lens and w_s is the radius of the unfocused beam. The higher laser power density at the focal point can be achieved by reducing the focused beam waist using a shorter focal length lens.

On the other hand, the angular spread in laser light generated by the diffraction of plane waves passing through a circular aperture consists of a central, bright circular spot (the Airy disk) surrounded by a series of bright rings. The beam divergence angle θ, measured to edges of Airy disk, is given by θ=2.44×λ/d, where λ is the laser wavelength and d is the diameter of the circular aperture. It can be

shown that a laser beam, with beam divergence θ_i, incident on a lens of focal length f, whose diameter is several times larger than the width of the incident beam, is focused to a diffraction-limited spot of diameter approximately equal to $f \times \theta_i$. If the focal region of the laser beam is assumed to be cylindrical in shape, the spot size in terms of length l, can be approximated as equation (2.16).

4. EXPERIMENTAL DETAILS

Laser-induced breakdown spectroscopy is a plasma based optical method that can be used to determine the elemental composition of solids, liquids and gases. In some cases small molecules can also be analyzed using LIBS. The LIBS technique uses similar instrumentation to that used by other spectroscopic methods. A typical LIBS apparatus utilizes a pulsed laser that generates the powerful optical pulses to form the plasma. Principles of laser operation in general and the operation of specific lasers are described in detail in numerous books. In addition, optical elements for collection and directing of light emitted from the laser-induced plasma, a spectrograph for separating the light by wavelength, and a detector, often an intensified-charge-coupled device (ICCD) to collect the image produced by the spectrograph, are necessary

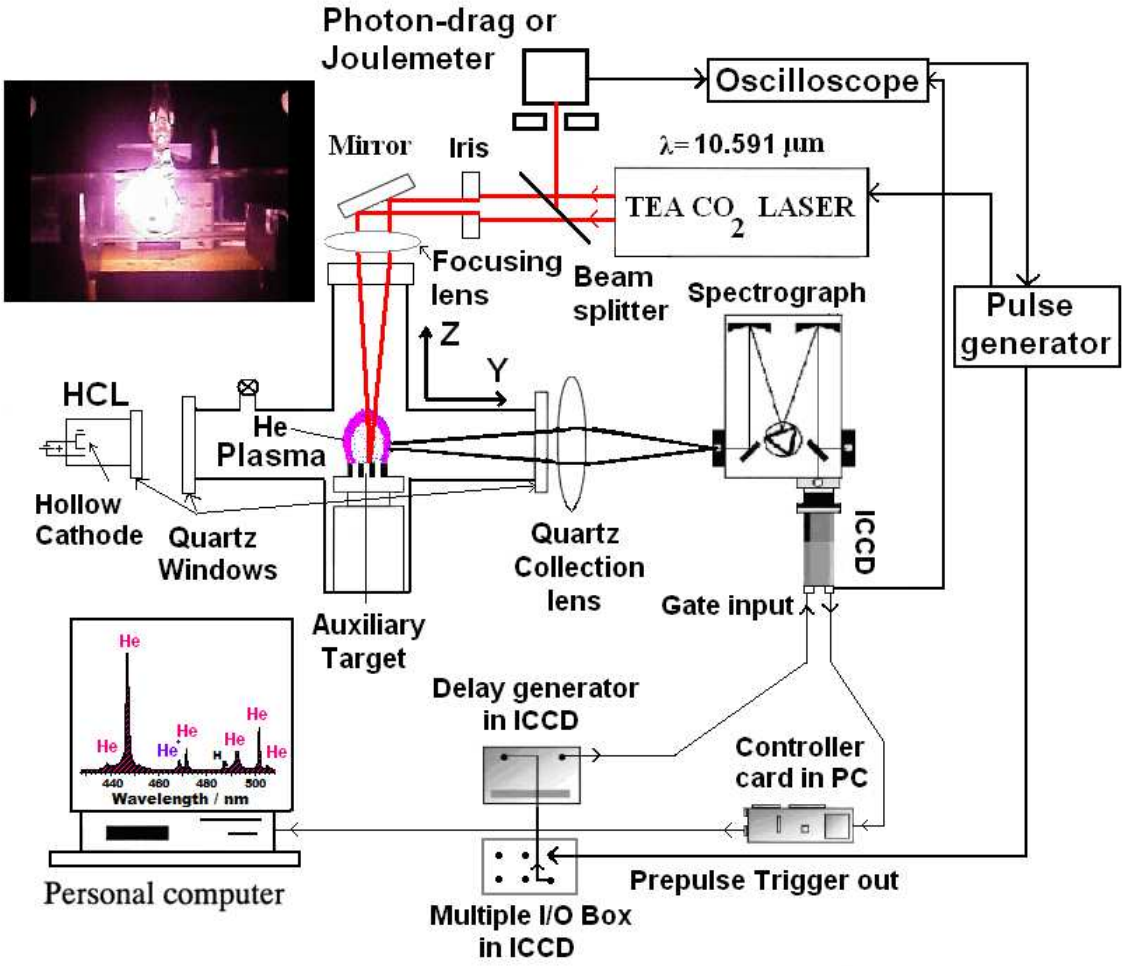

Figure 1. Schematic diagram of the experimental setup of the time gated ICCD for TEA-CO_2 pulsed laser He breakdown diagnostics.

A schematic diagram of the experimental configuration used for time-resolved TEA-CO_2 pulsed laser gas breakdown diagnostics is shown in figure 1. In this case the gas used was Helium. The majority of the experiments were carried out with a transverse excitation atmospheric (TEA) CO_2 laser (Lumonics model K-103) operating on an 8:8:84 mixture of CO_2:N_2:He, respectively. In some cases, a Q-Switched Nd:YAG pulsed laser (Litron model LPY707G-10) was used. The CO_2 laser was equipped with frontal Ge multimode optics (35 % reflectivity) and a rear diffraction grating with 135 lines mm^{-1} blazed at 10.6 μm. The laser pulse repetition rate was usually 1 Hz for CO_2 laser and 10 Hz for Nd:YAG laser. The divergence of the emitted laser beam was 3 and 0.5 mrad, respectively. The CO_2 laser delivered up to 3.16 J at 10.591 μm, leading to an estimated power of 49.5 MW (Eq. 3.18), intensity (power density or irradiance) of 6.31 GW cm^{-2} (Eq. 3.19), fluence of 403 J×cm^{-2} (Eq. 3.20), photon flux of 3.1×10^{29} photon×cm^{-2}×s^{-1} (Eq. 3.21), electric field of 1.54 MV×cm^{-1} (Eq. 3.22) and radiation pressure of 421 kPa (Eq. 3.23) on the focal position. The focused-spot area (7.85×10^{-3} cm^2) of the CO_2 laser beam was measured with a pyroelectric array detector (Delta Development Mark IV). The temporal shape of the CO_2 laser pulse, monitored with a photon drag detector (Rofin Sinar 7415), consisted in a prominent spike of a FWHM of around 64 ns carrying ≈ 90% of the laser energy, followed by a long lasting tail of lower energy and about 3 μs duration. The primary CO_2 laser beam was angularly defined and attenuated by a diaphragm of 17.5 mm diameter before entering to the sample cell. A beam splitter was used to redirect 10% of the laser pulse energy on a pyroelectric detector (Lumonics 20D) or on the photon-drag detector for energy and temporal shape monitoring and triggering, respectively, through a digital oscilloscope (Tektronix TDS 540). The laser-pulse energy was varied with the aid of several calibrated CaF_2 attenuating plates. The pulsed laser light from the CO_2 laser was focused by two NaCl lenses of 24 or 40 cm focal distance onto the sample. In time-resolved gas breakdown, a stainless steel mesh (7 mm×7 mm) was used as the auxiliary target. This allowed us to fix the focal position for LIB at any fluence inducing strong gas breakdown plasma. Although the metal mesh itself can be ablated, in our experimental conditions, mainly time- and space-resolved emission spectra from the gas plasmas were recorded. The high purity samples (≈ 99.99 %) were placed in a medium-vacuum cell equipped with a NaCl window for the laser beam and two quartz windows for optical access. The samples were initially at ambient temperature (298 K). The cell was evacuated with the aid of a rotary pump, to a base pressure of 4 Pa measured by a mechanical gauge.

The optical emission from the laser-induced plasma was optically imaged 1:1, at right angles to the normal of the target surface, by a quartz lens (focal length 4 cm, *f*-number = *f*/2.3) onto the entrance slit of different spectrometers. The emission was viewed in a *XZ* plane parallel to the front face of the target for different distances *z* along the plasma *Y* axis. Two spectrometers were mainly used: 1/8 m Oriel spectrometer (10 and 25 μm slits) with two different gratings (1200 and 2400 grooves×mm^{-1}) in the spectral region 2000-11000 Å at a resolution of ~1.3 Å in first-order (1200 grooves mm^{-1} grating), and an ISA Jobin Yvon Spex (Model HR320) 0.32 m equipped with a plane holographic grating (2400 grooves mm^{-1}) in the spectral region 2000-7500 Å at a resolution of ≈ 0.12 Å in first-order. Two detectors were attached to the exit focal plane of the spectrographs and used to detect the optical emissions from

the laser-induced plasma: an Andor DU420-OE (open electrode) CCD camera (1024x256 matrix of 26x26 μm^2 individual pixels) with thermoelectric cooling working at -30 ºC; A 1024×1024 matrix of 13×13 μm^2 individual pixels ICCD (Andor iStar DH-734), with thermoelectric cooling working at –20 ºC. The low noise level of the CCD allows long integration times and therefore the detection of very low emission intensities. The spectral window in high-resolution experiments was about 12 nm. The intensity response of the detection systems was calibrated with a standard halogen lamp. Several (Cu/Ne, Fe/Ne and Cr/Ar) hollow cathode lamps (HCL) were used for the spectral wavelength calibration of the spectrometers.

In time-resolved measurements, for synchronization, the CO_2 laser was operated at the internal trigger mode and the ICCD detector was operated in external and gate modes. The external trigger signal generated by the laser was fed through the scope and delay generator into the back of the ICCD detector head. The total insertion delay (45 ± 2 ns) is the total length of time taken for the external trigger pulse to travel through the digital delay generator and gater so that the ICCD will switch on. The time jitter between the laser and the fast ICCD detector gate was about ± 2 ns. The delay time t_d is the time interval between the arrival of the laser pulse on the metal mesh and the activation of the ICCD detector. The gate width time t_w is the time interval during which the plasma emission is monitored by the ICCD. Both parameters were adjusted by the digital delay generator of the ICCD detector. The CO_2 laser pulse picked up with the photon drag detector triggered a pulse generator (Stanford DG 535) through the scope and this pulse was used as external trigger in the ICCD camera. The laser pulse and the gate monitor output were displayed in a digital oscilloscope. In this way, by using the output of the photon drag detector, the oscilloscope, the delay pulse generator and the gate monitor output of the ICCD camera, the gate width time t_w and the delay time t_d could be adjusted without insertion time. The temporal history of a LIB plasma is illustrated schematically in figure 2. The time for the beginning of the laser pulse is considered as the origin of the time scale. As example, the insert pictures illustrate some emission spectra of germanium plasma recorded at different delay and width times. The temporal shape of the CO_2 laser pulse is also shown.

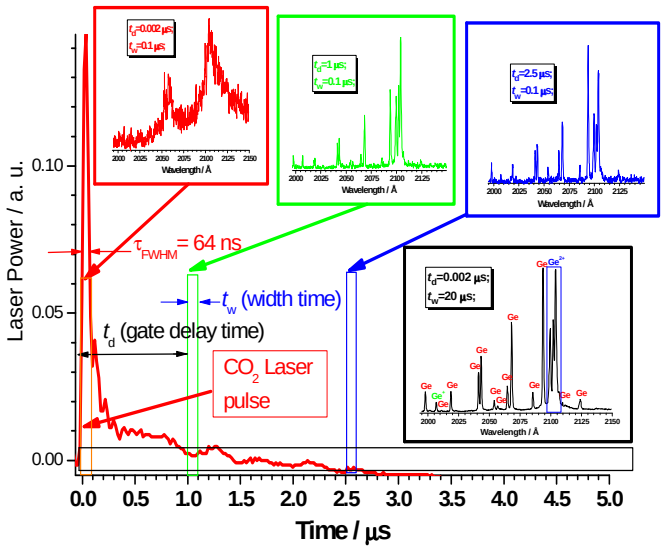

Figure 2. A schematic overview of the temporal history of the LIB Ge plasma. The temporal shape of the laser pulse is shown. Inset plots illustrate some spectra observed at different delay and width times.

5. RESULTS AND DISCUSSION

When a sample is irradiated by a high-power laser, a visible breakdown occurs. The start of LIB is an abrupt dramatic event involving the production of more than $\approx 10^{16}$ electron-ion pairs and the emission of characteristic radiation of the gas-plasma. The LIB plasma in He induced by a single CO_2 laser pulse (106 J/cm^2) is shown in the inset of figure 1. Although the laser-induced plasma appears spatially uniform to the naked eye, it is indeed elongated along the direction of the incoming laser beam. However, the structure of the LIB plasma is complex, and indeed there may be several distinct plasma regions produced along the laser beam axis. These multiple collinear plasmas are observable by the naked eye in gases at pressures around the atmospheric level. For a laser power density around 4.5 GW×cm^{-2}, the laser-induced plasma may be 6 cm long and a few centimeters in diameter. There is an expansion back toward the laser that essentially fills the converging cone of the laser radiation. The growth of the plasma in the direction opposite to the laser beam had lead to the model of radiation-supported detonation wave (Section 2.2.5). A shock wave propagates from the focal region (a point at the centre of the cell) into the gas and absorption of energy from the laser beam drives the shock wave, causing it to spread. The laser pulse remains in the focal volume after the plasma formation for some significant fraction of its duration and the plasma formed can be heated to very high temperatures and pressures by IB absorption. Since plasmas absorb radiation much more strongly than ordinary mater, plasmas can block transmission of incoming laser light to a significant degree; a phenomenon known as plasma shielding [63]. The high temperatures and pressures produced by plasma absorption can lead to thermal expansion of the plasma at high velocities, producing an audible acoustic signature, shock waves, and cavitation effects. The plasma also tends to expand back along the beam path toward the laser, a phenomenon known as moving breakdown. The shock wave heats up the surrounding gas which is instantaneously transformed in strongly ionized plasma.

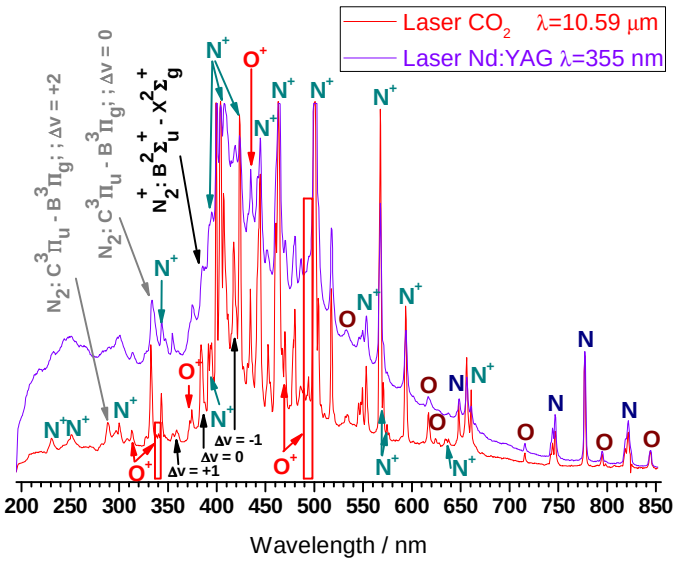

Figure 3. . The LIB emission spectra of air at atmospheric pressure excited by two different laser wavelengths.

A remarkable fact is the no influence of laser wavelength on the observed spectral lines and bands. This behaviour is a consequence of the collisional origin of the breakdown phenomenon. As example figure 3 shows the LIB spectra of air at atmospheric pressure using as excitation the laser lines at λ=356 nm (Nd:YAG laser) and λ=10.59 μm (CO_2 laser); the coincidence of different spectral lines is total.

5.1. LIBS of Helium

The temporally-resolved LIB technique in He has been used by several researchers [64-70] using high-power lasers. For He, it has been demonstrated by time-integrated and time-resolved OES [71] that a CO_2 laser with the help of a metal sub-target generates helium breakdown plasma in which the helium meta-stable excited state is produced. In this section we present our results on the large-scale plasma produced in helium gas at room temperature and pressures ranging from 12 to 101 kPa by high-power CO_2 LIB plasma [23]. Figure 4a and 4b displays a portion of the low-resolution LIB emission spectrum in He at a pressure of 31 kPa excited by a CO_2 laser wavelength of 9.621 μm, as a function of the laser intensity. The assignments of some atomic lines from He, He^+ and H are shown. Strong atomic He lines dominate the spectrum but, ionic He^+ and atomic H lines are also present. The high intensity of H lines is remarkable, taking into account that the hydrogen atoms present in the sample are due to an impurity of water vapour. This fact is probably due to the energy transfer from the meta-stable excited states of He (for example, $^3P^0_2$, $^3S_1$) to H atoms, increasing the population of the hydrogen excited states [69]. Also, a Penning ionization of hydrogen can be produced by such meta-stable states of helium. Since the hydrogen is truly very trace, the role of this ionization is not important. An increase of emission intensity for atomic and ionic species with increasing the laser intensity was observed. At higher laser power densities the spectral lines are more broadened than at lower power densities due to the high pressure associated with the plasma. It is assumed that at higher laser intensity the LIB plasma is more energetic and the density number of He and He^+ species increase.

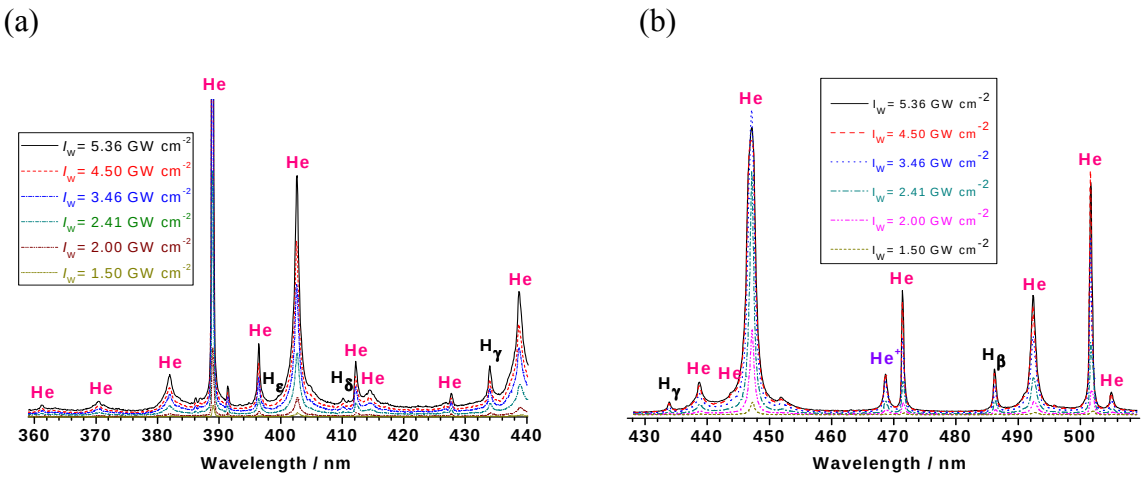

Figure 4. Low-resolution LIB emission spectra in He at 31 kPa pressure observed in two regions, excited by the CO_2 laser wavelength of 9.621 μm, as a function of the laser power density.

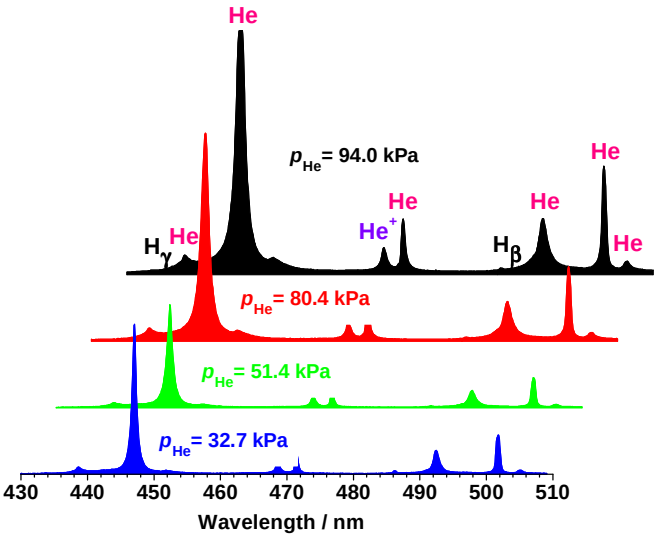

Figure 5. Low-resolution LIB emission spectra at various He pressures excited by the TEA-CO_2 laser wavelength of 9.621 μm at a laser power density of 2.41 GW cm^{-2}.

The pressure of the gas is one of the controlling parameters of plasma characteristics, as well as the factors related to the laser energy absorption. Figure 5 shows LIB emission spectra in the He pressures interval from 32.7 to 94 kPa excited by the CO_2 laser wavelength at 9.621 μm for a laser power density of 2.41 GW×cm^{-2}. A slight decrease of the intensities of He, He^+ and H, from 25 kPa to about 51 kPa, was observed. Beyond 51 kPa, as the helium pressure increased, line intensities increased significantly. This anomalous behavior can be related to the volume of the plasma expanding to a larger size at higher helium pressures.

As we indicated in section 2.2.1, when a high-power laser beam interacts with a gas, electrons involving the formation of laser-induced plasma can be produced through MPI [n$h\nu$ + He → He^+ + e + I_P(He); n$h\nu \geq I_P$(He)] and EII {e + nhν + He → e^*[$\varepsilon \geq I_P$(He)] + He → He^+ + e} both followed by electron cascade. The MPI process is relatively improbable for helium atoms in the ground state He($1s^2$ $^1S_0$) since its high ionization potential (24.587 eV) [72], means that more than 190 photons are required for this process. Besides, the probability of simultaneous absorption of photons decreases with the number of photons necessary to cause ionization. Calculations of MPI probability using Eq. (2.1) for He gives $W_{MPI} \approx 0$ s^{-1} for the CO_2 laser at λ=9.621 μm and I_W=1 GW×cm^{-2}. For example, for a 193 nm (ArF) at the laser intensity I_W=10 GW×cm^{-2} (n=7), the probability of MPI for He gives W_{MPI}=1.4×10^{-25} s^{-1}, being also negligible. We have made experimental measurements of the breakdown threshold laser intensities in helium. Experimental power density threshold for He is measured for the CO_2 laser at λ=9.621 μm. Figure 6 shows the measured breakdown threshold intensity for He as a function of pressure. The threshold intensities for He breakdown have been reported by different authors [6,43]. It has to be noted that we have obtained similar threshold power densities for He as those given by Chan who uses also CO_2 laser [43], but lower values those reported in Ref. [6] using ruby laser. This fact can be related in part to the used focal length (24 cm) and beam size in the focal region (7.85×10^{-3} cm^2) that is one order of magnitude, at least, higher than the values commonly used in the

literature, favoring the probability of existence of free electrons to seed the process and decreasing the threshold laser intensity due to the lack of the diffusion losses.

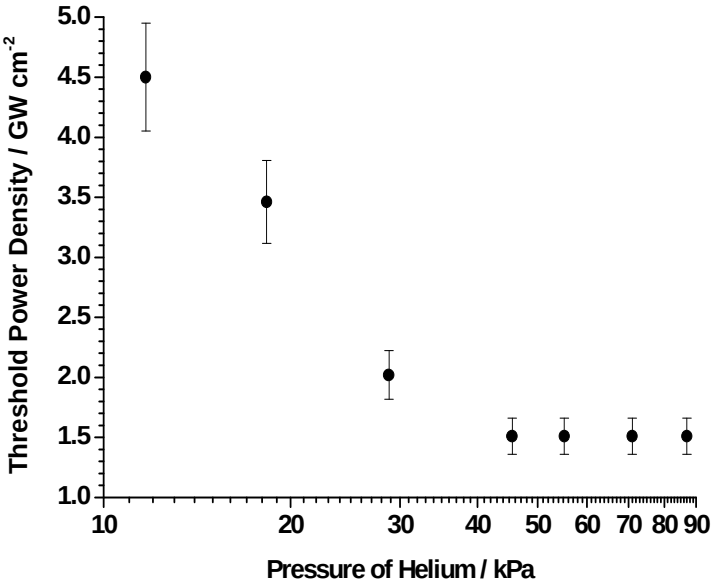

Figure 6. Experimental laser-induced breakdown thresholds in He excited by the CO_2 laser at 9.621 μm. Error bars, partially due to the measured power density, are indicated.

It has been established (see section 2.2.3) the threshold photon flux density or equivalently the threshold power density for MPI varies with the pressure as $p^{-1/n}$. This fact predicts a very weak dependence of the threshold power density on pressure due to the high number of photons (n=190) necessary for ionization. However, as we can see from figure 6, the breakdown threshold power density in helium decreases as pressure increases. It can be seen that the pressure dependence is not in accord with MPI while it is in qualitative agreement with electron impact ionization. Consequently, starting from our experimental observations and calculations, we can conclude that although, the first electrons must appear via MPI or natural ionization, electron impact is the main mechanism responsible for the breakdown in helium.

Using the Saha equation (3.17) for He, we observed that the gas is already amply ionized at thermal energies well below the ionization-energy of 24.587 eV equivalent to 285,320 K. At about 22,500 K the ionization degree is 0.5.

The LIB spectra of He were measured at different delay and width times at atmospheric pressure. In these experiments, the spectra had been obtained in the region 464-475.5 nm, at a delay time ranging from 0 to 20 μs and z=5 mm. The range was chosen in order to detect both, atomic and single ionized He species. Figure 7 illustrates the time-resolved evolution from laser-induced (2.41 GW×cm^{-2}) helium plasma monitored at 0, 0.1, 0.2, 0.3, 0.5, 1, 1.5 and 2 μs gate delays for a fixed gate width time of 0.1 μs. One can see that immediately after the peak laser pulse ($t_d \leq 0.1$ μs), no apparent line emissions were observed. However, after the peak laser pulse, the plasma emission presents a weak continuum that increases as a consequence of the plasma heating. This continuum radiation is emitted by the laser-induced plasma as a consequence of free-free and free-bound transitions. During the initial stages after the

laser pulse ($t_d \leq 0.9$ μs), He^+ emission dominates the spectrum, and no apparent He emission was observed (figure 7). When the delay is increased ($t_d \geq 0.9$ μs), the intensity of the He^+ ionic line steeply decreases as a consequence of the expansion, recombination and cooling of the plasma. For $t_d \geq 0.2$ μs, He^+ line emission becomes progressively narrow as a consequence of the decreasing of the electron number density. At t_d=2.5 μs, the He^+ ionic emission line practically disappears. The intensity of He line is appreciable for $t_d \geq 0.9$ μs reaching at maximum around 3 μs and being detected up to ≈15 μs. The high noise level observed in the spectra is due to the gain used in the ICCD intensifier. This gain is necessary in order to observe the spectra in a gate width time of 0.1 μs.

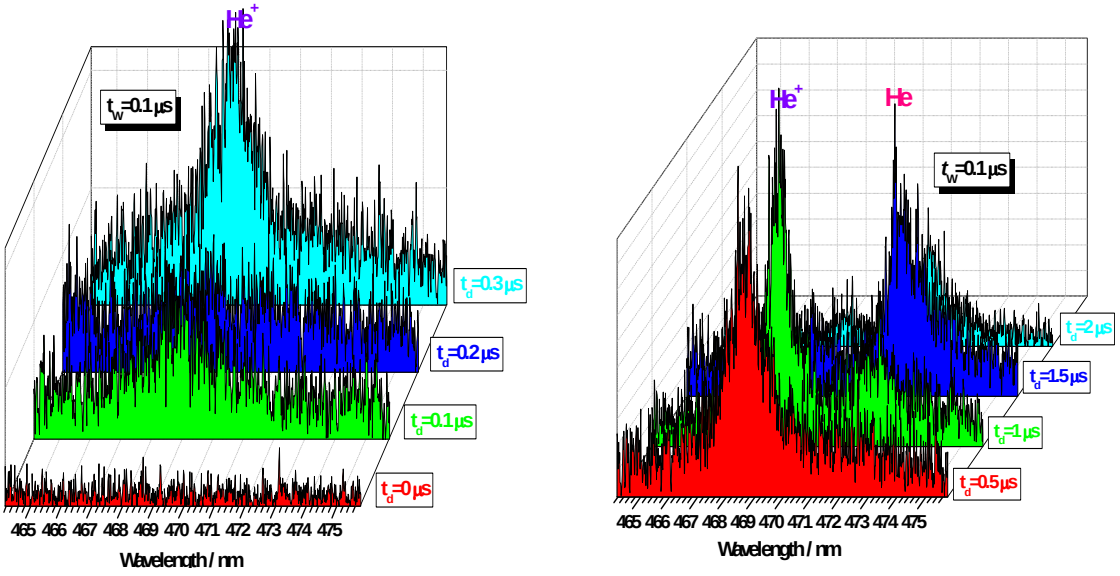

Figure 7. Time-resolved emission spectra from laser-induced (2.41 GW×cm^{-2}) He plasma observed in the region 464-475.5 nm monitored at 0, 0.1, 0.2, 0.3, 0.5, 1, 1.5 and 2 μs gate delays for a fixed gate width time of 0.1 μs and z=5 mm.

Space-and-time resolved OES measurements can be used to estimate the plasma expansion rate and kinetic energy. The temporal evolution of spectral atomic and ionic line intensities at a constant distance from the target can be used to construct the time-of-flight profile. TOF studies of the emission provide fundamental information regarding the time taken for a particular species to evolve after the laser-induced plasma has been formed. Specifically, this technique gives an indication of the velocity of the emitted species. A coarse estimation of the velocity for the different species in the plasma can be inferred from the time-resolved spectra by plotting the intensities of selected emission lines versus the delay time, and then calculating the velocity by dividing the distance from the target by the time where the emission peaks reach their maxima. This method for determination of plasma velocity should be used with care due to the superposition of both, expansion and forward movements of the plasma. The experimental TOF distributions $N(t)$ are essentially number density distributions. They were converted to flux distributions dN/dt employing a correction factor z/t, where z means the flight distance along the plasma expansion and t is the delay time after the laser pulse incidence. From TOF spectra, the translationally kinetic energy can be

deduced [$KE=(1/2)m(z/t)^2$] by measuring the time t required to transverse the distance z from the target to the observation point.

Figure 8 displays the TOF, velocity and kinetic energy distributions of He^+(≈ 468.57 nm) and He(≈ 471.34 nm) lines as a function of delay time for the helium breakdown experiments induced by CO_2 laser. In these experiments, TOF distributions present different characteristics. Thus, the time of the He^+ maximum is the same with the time in which the intensity of the excited He atom line starts to increase, and the time when the ionic species disappear coincides with the maximum for the He neutral atoms. The evident delay between He neutral atoms and He^+ TOF maxima is the effect of the additional amount of He atoms produced by the recombination of He^+ ions with electrons. The velocity distribution of ionic species He^+ is comparatively wider [≈ 28.7 km/s (FWHM)] than the velocity distribution of He [≈ 4.6 km/s (FWHM)]. The velocity distributions of He^+ and He species are centred at about 6.7 and 1.6 km/s, respectively. The kinetic energy obtained for He^+ and He lines as a function of delay time are plotted in the insert of figure 8b. The results show small atomic and large ionic average kinetic energies. We have observed He^+ ions with a kinetic energy ranging from ≈ 0.3 eV up to ≈ 50 eV and He atoms with a kinetic energy ranging from ≈ 0.001 eV up to ≈ 0.9 eV. The kinetic energy distribution of ionic species He^+ is comparatively wider [≈ 18.8 eV (FWHM)] than the kinetic energy distribution of He [≈ 0.4 eV (FWHM)].

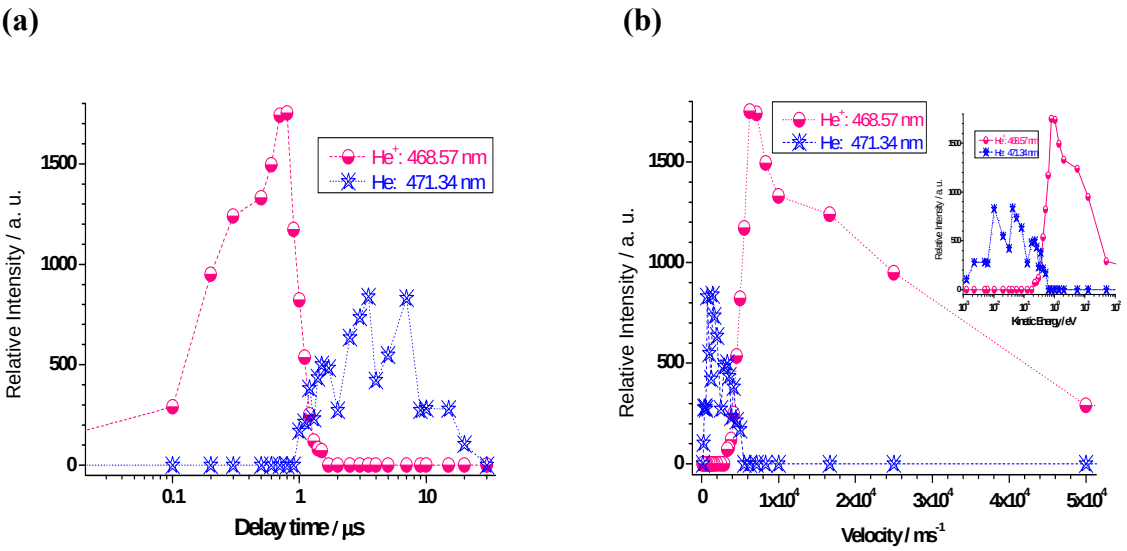

Figure 8. **(a)** Number density TOF distributions of He^+(468.57 nm) and He(471.34 nm) lines as a function of delay time (fixed gate width time of 0.1 μs) for a laser intensity of 2.41 GW×cm^{-2}. **(b)** Velocity distributions derived from the experimental TOF profiles for the indicated species. The insert shows the kinetic energy distribution for the indicated species.

The kinetic energy distributions of He^+ and He species are centred at about 0.8 and 0.05 eV, respectively. However the velocity for He atoms may be taken carefully because probably all of them are not formed at the same distance from the mesh and their velocities become higher and their velocity distribution wider. These results show that recombination is the most important source of He atoms in the plasma and that the

energy in excess to He ionization supplied by CO_2 laser pulse is transferred as kinetic energy.

We have also studied time-resolved OES of the He plasma by varying the laser energy. Figure 9 shows the TOF and velocity distributions of He^+ and He lines at two laser intensities of 2.41 and 1.55 GW×cm^{-2}. The TOF distributions of He^+ were found to consist approximately of one intense maximum at ≈ 0.8 μs (I_W=2.41 GW cm^{-2}) and ≈ 0.5 μs (I_W=1.55 GW cm^{-2}). The TOF distributions of neutral helium consist in several maxima which indicate the complexity of the processes that generated this excited species. We have observed that when the laser intensity is increased, the He TOF distribution gets wider. On the contrary, an abnormal behaviour is observed for the variation of the He^+ TOF distribution with laser intensity. When the laser fluence is increased, the He^+ TOF distribution becomes slightly narrower and moves towards longer delay times. This behaviour is probably due to the temporal profile of the CO_2 laser pulse which can be partially absorbed by the plasma.

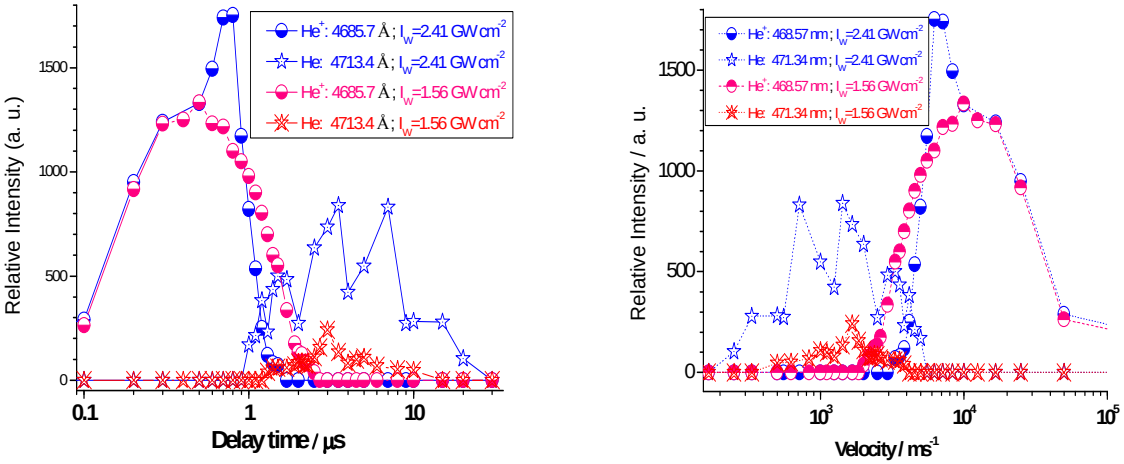

Figure 9. TOF and velocity distributions of He^+(468.57 nm) and He(471.34 nm) lines at two laser intensities (2.41 and 1.55 GW×cm^{-2}).

For the electron density measurements, Stark broadening can be used (see section 3.3). For helium plasma, we use the widths of the He line (1s4s $^3S_1 \longrightarrow$ 1s2p $^3P^0_{2,1,0}$) at ≈ 471.3 nm for delay time > 2.3 μs and the He^+ line (P_α) at ≈ 468.57 nm for delay time ≤ 1 μs. By substituting the Stark line widths of He multiplet at different delay times in Eqn. (3.12) and the corresponding values of the electron impact parameter, W (0.034-0.046 nm from Griem [54] at plasma temperatures between 5000 and 40000 K), we obtain the electron density for delay times greater than 2.3 μs. The Stark broadening (in nm) for the He^+ P_α line is related to the electron density n_e (in cm^{-3}) by the following relationship for an H-like ion [73-75]:

$$n_e = 3.31\times10^{17}(\Delta\lambda^S_{FWHM})^{1.21}. \qquad (5.1)$$

Figure 10 gives the time evolution of electron density and its first derivative with respect to delay time. This figure shows that the electron density exhibits an initial fast decay. Since the continuum dominates plasma emission soon after CO_2 laser shot, electron density cannot be measured before 0.2 μs. The electron density at 0.2 μs is

about 1×10^{18} cm^{-3} and afterwards decreases as the time increases and reaching an approximately constant value of 2×10^{16} cm^{-3} for delay times greater than 10 µs. Multiple measurements lead to a statistical error of the electron density below 10%. The decrease of n_e is mainly due to recombination between electrons and ions in the plasma (see section 2.2.2). These processes correspond to the so-called radiative recombination and three-body recombination processes in which a third body may be either a heavy particle or an electron. The electron number density $n_e(cm^{-3})$ in the laser-induced plasma is governed by equation (2.10). As it is observable from figure 10 the three-body recombination process prevails over the ionization one. By a non-linear fit to of the electron density as function of the delay time to a single exponential decay, we obtained a recombination time $t_{rec}=0.84 \pm 0.03$ µs with a regression coefficient of 0.98. From this value, the rate constant of the recombination process was estimated as $k_{rec} \approx 8.5\times10^{-30}$ $cm^6\ s^{-1}$.

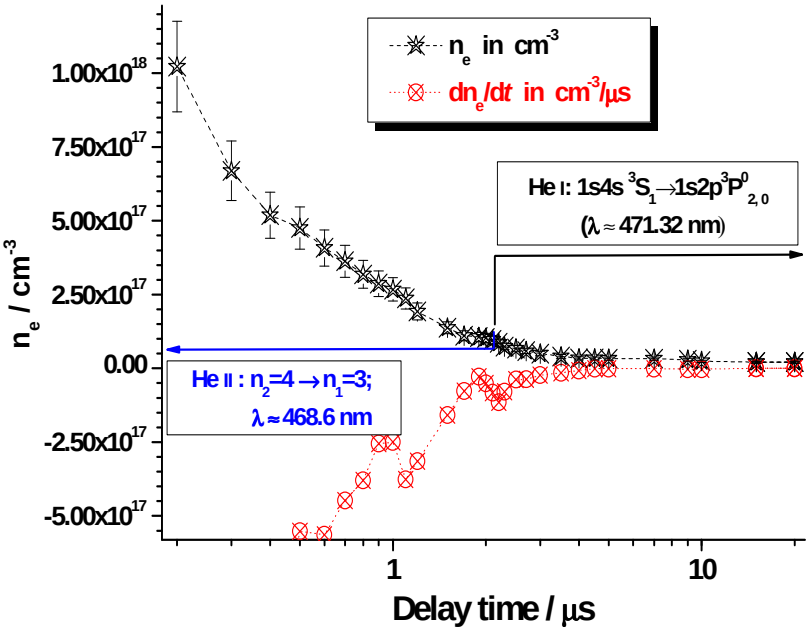

Figure 10. The temporal evolution of electron density n_e and dn_e/dt for different delay times from plasma ignition at a laser intensity of 2.41 GW×cm^{-2}.

5.1. LIBS of Germanium

Elements of the group IVA have interesting electronic properties and important practical applications. In particular, Si and Ge nanocrystals embedded in a dielectric matrix (such as SiO_2) have been demonstrated as potential candidates for the fabrication of optoelectronic, photovoltaic and non-volatile memory devices. Although there is a large amount of work on the study of the solid phase characteristics of these compounds, the gaseous properties of the component elements are not so well known. Germanium is an important semiconductor material used in electronic devices, fiber-optic systems, infrared optics, semiconductor-based detectors and polymerization

catalysts. It is also used as an alloying agent for increase the refraction index of glasses or as substrate wafers for high-efficiency multi-junction solar cells [76]. In this section we present our results on time-resolved optical emission measurements in laser-induced plasma plumes following CO_2 pulsed-laser irradiation of Germanium targets [24]. It is well known that germanium under normal absorption conditions is transparent to IR radiation. However, when the laser intensity increases and reaches a certain threshold value, as happens with high-power lasers, Ge is no longer transparent. The dynamics of materials ablated from surfaces by pulsed-laser irradiation are of fundamental technological and physical interest. In this way, the plasma induced by nanosecond lasers is successfully employed for Ge thin film deposition [77,78]. The temporally-resolved LIB technique in Ge has been studied by several researchers [79,80] using high-power lasers.

The UV LIB emission spectrum of Ge induced by a CO_2 pulsed laser at a wavelength of 10.591 μm and an intensity of 1.4 GW×cm^{-2} is shown in figure 11. The assignments of some individual atomic-ionic lines from Ge, Ge^+; Ge^{2+} and Ge^{3+} are indicated by stick labels. Strong ionic Ge^{3+} lines dominate the spectrum indicating the high ionization of germanium produced by LIB.

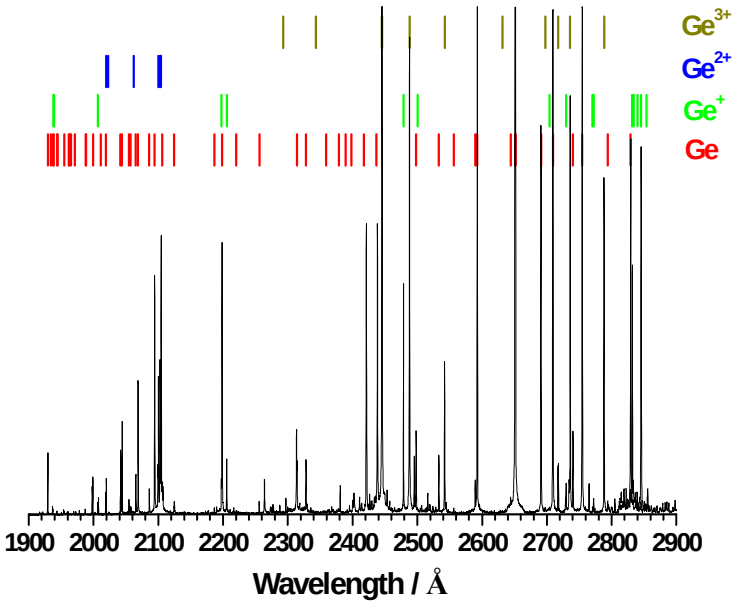

Figure 11. The ultraviolet LIB emission spectrum of Ge induced by a CO_2 laser wavelength of 10.591 μm.

Figure 12 displays a portion of the LIB emission spectrum in Ge as a function of the laser intensity. An increase in the emission intensity for atomic and ionic species along with the increase the laser fluence was observed. At higher laser fluences the spectral lines are broader than at lower power densities due to the high pressure associated with the plasma. It is assumed that at higher laser intensity the LIB plasma is more energetic and the density number of ionic and atomic species increase.

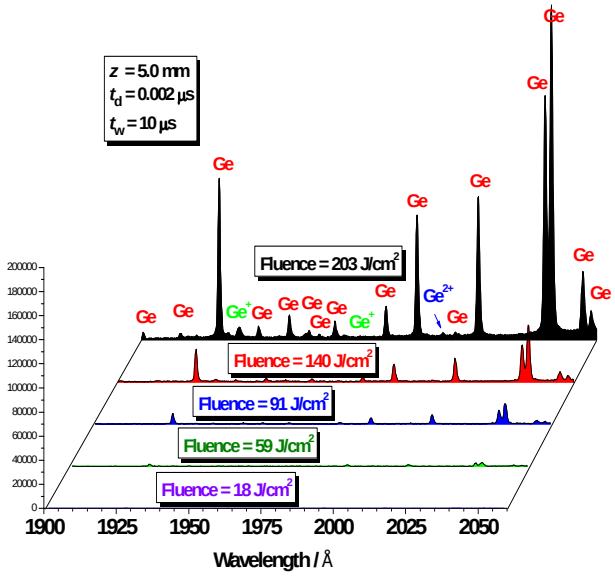

Figure 12. The LIB emission spectra of Ge at various laser fluences monitored at 0.002 µs delay time for a gate width time of 10 µs.

The LIB spectra (1.4 GW×cm^{-2}) of Ge were measured at different delay and width times. In a first set of temporal measurements, the spectra had been obtained in the spectral region 2000-2150 Å, at a delay time ranging from 0.002 to 5 µs and z=15 mm (Figure 13a). Also, the time-integrated spectrum (t_d=0.002 µs and t_w=20 µs) is shown

(a) **(b)**

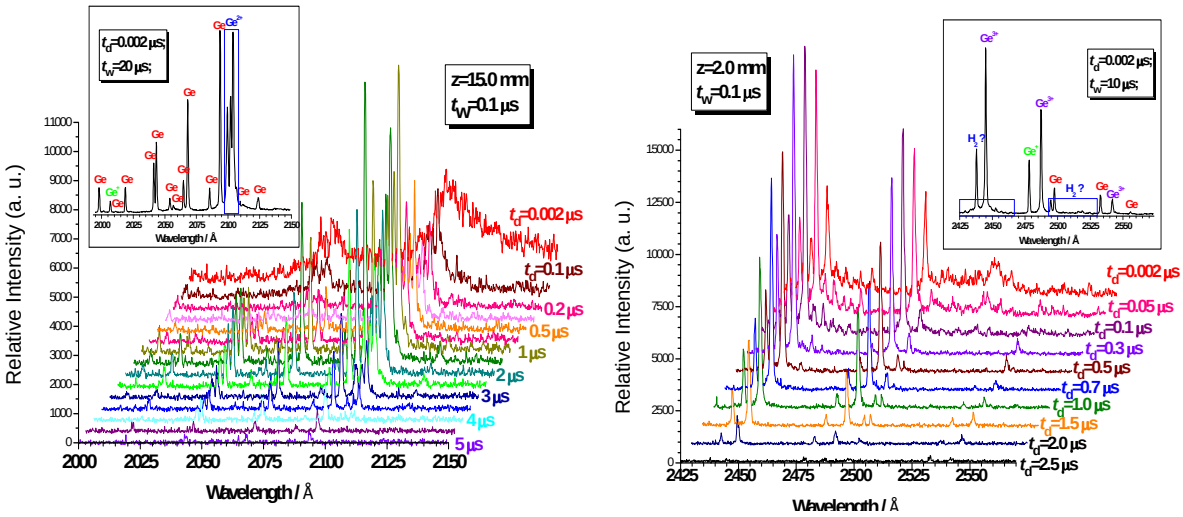

Figure 13. Time-resolved emission spectra from the laser-induced Ge plasma recorded for two different experimental conditions: **(a)** 2000-2150 Å and z=15 mm; **(b)** 2425-2570 Å and z=5 mm.

The spectral range was chosen in order to detect atomic, single and double ionized Ge species. During the initial stages after the laser pulse (t_d≤1 µs), Ge^{2+} emission dominates the spectrum. The emission lines for Ge^{2+} become progressively and spectrally narrower

as a consequence of the variation in electron number density. This indicates that the electron density and excitation temperature decrease during the plasma expansion. When the delay is increased ($t_d \geq 1$ μs), the intensity of Ge^{2+} ionic lines steeply decrease as a consequence of the radiative recombination between ions and electrons, being detected up to ≈ 4 μs. For $t_d \leq 0.2$ μs no apparent Ge emission was observed. When the delay is increased ($t_d \geq 0.2$ μs), the intensity of Ge atomic lines steeply increases, also due to the electron-ion recombination in the plasma. The intensities of Ge lines reach the maximum at around 1.5 μs and being detected up to ≈ 5 μs. Figure 13(b) displays a similar temporal evolution of the LIB spectrum of germanium plasma in the spectral region 2425-2570 Å at delay times ranging from 0.002 to 2.5 μs and z=2 mm. Also it is shown the time-integrated spectrum for t_d=0.002 μs and t_w=10 μs. The spectral range was chosen in order to detect Ge, Ge^+ and Ge^{3+} species. In spite of our use of high-purity germanium, emissions from residual air (4 Pa), especially from nitrogen species as well as fragments of dissociated water molecules (H_2 and OH), were observed. During the initial stages after the laser pulse ($t_d \leq 2.5$ μs) Ge^{3+} emissions dominate the spectra. The intensities for the emission lines of Ge^{3+} show a maximum at 0.1 μs. As above, the emission lines for Ge^{3+} for $t_d \geq 0.1$ μs become progressively and spectrally narrower as a consequence of the electron number density variation. The Ge emission lines, due to the actual observation distance used (z=2 mm), were now observed during the initial stages after the laser pulse.

Figure 14(a) displays the TOF profiles for germanium breakdown experiments induced by CO_2 laser pulses. The Ge, Ge^+, Ge^{2+}, and Ge^{3+} lines in the UV region correspond to the spectra of figure 13 recorded at 5 mm. The TOF distributions of Ge and Ge^+ species were found to consist approximately of one weak maximum at ≈ 0.5 μs and one intense maximum at ≈ 1.2 μs, respectively.

(a) **(b)**

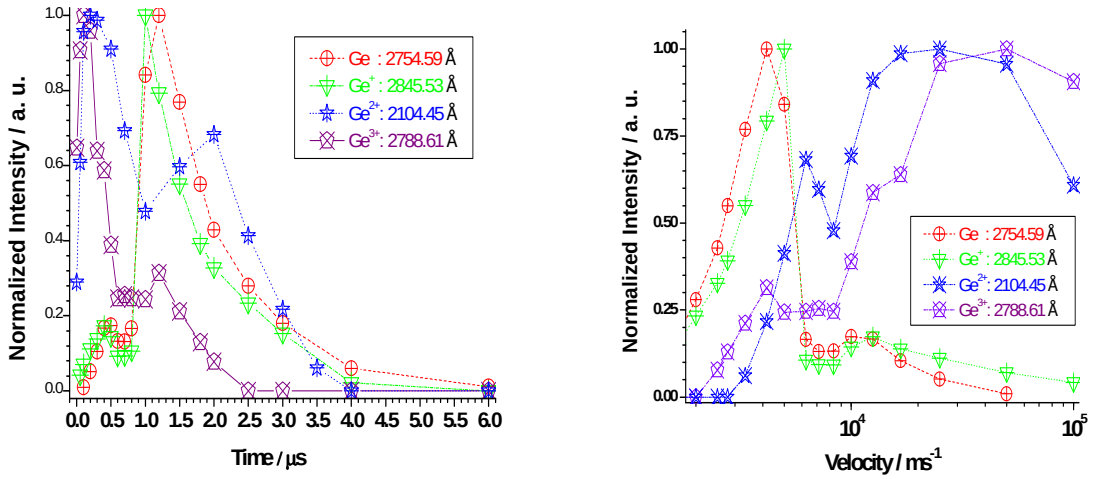

Figure 14. **(a)** Number density TOF distributions of Ge(2755 Å), Ge^+(2845 Å), Ge^{2+}(2104 Å), and Ge^{3+}(2789 Å) lines as a function of delay time (fixed gate width time of 0.1 μs), for a laser intensity of 1.4 GW×cm^{-2} and z = 5 mm. **(b)** Velocity distributions derived from the experimental TOF profiles for the indicated species.

The TOF distributions of Ge^{2+} were found to consist approximately of one intense maximum at ≈ 0.2 μs and one medium maximum at ≈ 1.9 μs while that for Ge^{3+}, one intense maximum at ≈ 0.1 μs and one weak maximum at ≈ 1.2 μs were observed. The emission intensity of Ge^{3+} ionic lines decreases more rapidly than the emission intensity of the other lines. The time duration of different lines of Ge, Ge^{+}, Ge^{2+}, and Ge^{3+} were nearly 6, 5, 4 and 2.5 μs, respectively. The evident delay between Ge and Ge^{+} species, with respect to Ge^{2+} and Ge^{3+} ions TOF maxima, is probably due to the formation of these species from the recombination of Ge^{2+} and Ge^{3+} ions with electrons. The velocity distributions that are derived from these TOF distributions are displayed in figure 14(b). These distributions present different characteristics. For atomic Ge(2754 Å) and ionic Ge^{+}(2845 Å), Ge^{2+}(2104 Å) and Ge^{3+}(2788 Å) species, the velocity distributions are centered at ≈ 4.1, 5, 25 and 50 km/s, respectively. The velocity distributions for Ge and Ge^{+} are comparatively narrower [≈2.8 and ≈2.7 km/s (FWHM), respectively] than the velocity distributions for Ge^{2+} [≈97 km/s (FWHM)] and Ge^{3+} [≈120 km/s (FWHM)].

The different components of the TOF and velocity distributions for each species may be due to different formation mechanisms. Particularly, for Ge and Ge^{+} species, the complex velocity distribution observed in figure 14 might indicate that several processes can be involved in its formation. For example, $Ge + nh\nu + e \rightarrow Ge + e^{*} \rightarrow Ge^{+*} + 2e$ and $Ge + nh\nu + e \rightarrow Ge + e^{*} \rightarrow Ge^{*} + e$ processes (inverse bremsstrahlung and electron-impact ionization and electronic excitation) can be associated to the maxima at 0.5 μs observed in figure 14(a). On the other hand, the observed maxima at 1.2 μs can be due to the processes $Ge^{2+} + 2e \rightarrow Ge^{+} + e$ and $Ge^{+} + 2e \rightarrow Ge + e$ (three body electron-ion recombination). For Ge^{2+} and Ge^{3+} two maxima are observed in the TOF profiles. The intense maxima at ≈ 0.2 μs are probably due to $Ge + nh\nu + e \rightarrow Ge + e^{*} \rightarrow Ge^{2+*} + 3e$ and $Ge + nh\nu + e \rightarrow Ge + e^{*} \rightarrow Ge^{3+*} + 4e$ processes. The medium/week maxima for Ge^{2+} and Ge^{3+} which appear at 1.9 and 1.2 μs, respectively, could be due to three body electron-ion recombination processes ($Ge^{3+} + 2e \rightarrow Ge^{2+} + e$; $Ge^{4+} + 2e \rightarrow Ge^{3+} + e$). From these observations it seems that Ge^{2+} and Ge^{3+} are mainly generated on the crystalline Ge target while Ge and Ge^{+} are mainly produced in gas phase at some distance from the laser focal position.

The excitation temperature was obtained from the Boltzmann equation (3.16) for the line intensities of several Ge lines at a delay time of 3 μs. The spectral lines wavelengths, energies of the upper levels, statistical weights, and transition probabilities used for these lines were obtained from NIST Atomic Spectra Database [58]. The obtained excitation temperature was 20000 ± 1200 K.

For the electron density measurements we use the Stark broadening of the Ge^{3+} line ($5d\ ^2D \longrightarrow 5p\ ^2P^0$) at ≈ 2488 Å for delay times ≤ 2.5 μs and the Ge line ($4s^2 4p5s\ ^1P^0_1 \rightarrow 4s^2 4p^2\ ^1D_2$) at ≈ 3039 Å for delay times > 2.5 μs (see Sec. 3.3). By substituting the Stark line widths of Ge^{3+} and Ge lines at different delay times in Eqn. (3.12) and the corresponding values of the electron impact parameter, W (0.0240-0.00763 Å from Popovic et. al. [81] and 0.0140-0.0147 Å from Dimitrijevic et. al. [82], respectively, at plasma temperatures between 5000-50000 K), we obtain the electron density for different delay times.

Figure 15 gives the time evolution of electron density and its first derivative with respect to delay time by setting the gate width of the intensifier at 0.1 μs and a laser intensity of 1.42 $GW \times cm^{-2}$ and z = 5 mm. The errors provided for electron densities

considered the uncertainty in the impact parameters and line broadenings. The initial electron density at 0.002 μs is approximately 2×10^{16} cm^{-3}. Afterwards, the density increases until 3.5×10^{16} cm^{-3} over the period of 0.3 μs and then decrease as the time is further increased. For times > 2.5 μs the electron density decreases quickly.

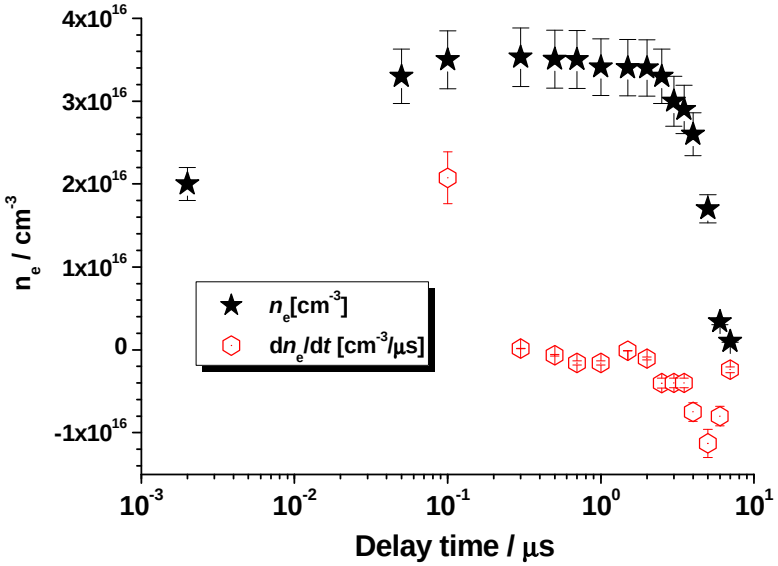

Figure 15. The temporal evolution of electron density n_e and dn_e/dt for different delay times from plasma ignition at a laser intensity of 1.42 GW×cm^{-2} and z = 5 mm.

As it is observable from figure 15, the equilibrium condition can be established at 0.3 μs (dynamical equilibrium; see Sec. 2.2.2). For t < 0.3 μs the ionization prevails while for t > 0.3 μs the three-body electron recombination process dominates over the ionization one. By a non-linear fit of the intensities for Ge^+, Ge^{2+} and Ge^{3+} as function of the delay time to a single exponential decay, we obtained three recombination times of t_{rec}=0.91 ± 0.08 μs. 0.40 ± 0.08 μs, and 0.30 ± 0.07 μs respectively. The rate constants of the recombination processes can be estimated from the relation $k_{rec}=1/(n_e^2.t_{rec})$. The corresponding values for Ge^+, Ge^{2+} and Ge^{3+} are 8.9×10^{-28}, 2.0×10^{-27}, and 2.7×10^{-27} cm^6 s^{-1}, respectively.

5.2. LIBS of Germane (GeH_4)

In this section we analyze the LIB spectrum of a precursor of germanium species such as germane [22]. Up to this paper, we have found no data on experiments of LIBS of gaseous precursors of germanium as germane (GeH_4) which is used for the deposition of epitaxial and amorphous silicon-germanium alloy layers. In this study, LIB plasma generated by CO_2 laser pulses (λ=10.653 μm) in GeH_4 has been investigated by OES. The plasma induced in germane to pressures ranging from 2 to 10 kPa and laser fluences from 18.1 to 352 J×cm^{-2} has been detected and analyzed. The strong emission observed in the plasma region is mainly due to the germanium species

described in Sec. 5.1. Also, relaxation of excited atomic H and molecular H_2 were observed.

For the present experiments the measured focused-spot area was 7.85×10^{-3} cm^2. This value is higher than the calculated area (2.2×10^{-4} cm^2) obtained from the beam waist (Eq. 3.23). This fact is due to the non-Gaussian profile of the CO_2 laser beam. Moreover the CO_2 laser beam passes through a circular aperture of diameter 17.5 mm. For this diaphragm the calculated divergence angle for the laser beams at 9.621 and 10.591 μm are 1.3 and 1.5 mrad, respectively. Thus, considering the total beam divergence (≈ 4.4 mrad), the calculated diameter of the focused TEA-CO_2 laser (beam waist) is 1.06 mm, which is very similar to the measured value (≈1 mm). If the focal region of the laser beam is assumed to be cylindrical in shape, the spot size in terms of length l (Eq. 2.16) of the focused TEA-CO_2 laser is 6.0 mm, which is similar to the measured value (≈7 mm). For the different pulse laser energies measured in LIB of oxygen, the calculated laser peak power (Eq. 3.18), intensity (Eq. 3.19), fluence (Eq. 3.20), photon flux (Eq. 3.21), electric field (Eq. 3.22) and pressure radiation (Eq. 3.23) are given in Table 1.

Table 1. Laser parameters for the TEA CO_2 LIB experiments in Germane.

Energy E_W (mJ)	Power P_W (MW)	Intensity I_W (GW cm^{-2})	Fluence Φ_W (J cm^{-2})	Photon Flux, F_{ph} (ph. cm^{-2} s^{-1})	Electric Field F_E (MV cm^{-1})
2765	43.4	5.52	352	2.68×10^{29}	1.52
1793	28.1	3.58	228	1.71×10^{29}	1.22
1179	18.5	2.35	150	1.14×10^{29}	0.992
767	12.0	1.53	97.7	7.43×10^{28}	0.801
471	7.4	0.94	60.0	4.56×10^{28}	0.627
304	4.7	0.61	38.7	2.94×10^{28}	0.506
229	3.6	0.46	29.2	2.22×10^{28}	0.439
206	3.2	0.41	26.2	1.99×10^{28}	0.415
142	2.2	0.28	18.1	1.38×10^{28}	0.343

The LIB spectrum of GeH_4 (pressure of 5 hPa and fluence of 228 J cm^{-2}) was obtained at low resolution in the 2000-8400 Å region. Figure 16 displays an overview of the low-resolution LIB germane emission spectrum. In the UV region a very weak spectrum was obtained due to the low sensitivity of the spectrograph in this zone. However, numerous Ge lines are identified e.g. at 2094, 2188, 2586, 2647, 2765, 3038 and 3267 Å. Intense Ge^+ lines at 2732, 2832 and 2843 Å are detected and also an intense Ge^{3+} line at 3554 Å is seen. Above 3600 Å intense, although less numerous than in the UV, Ge lines are detected at e.g. 4228 and 4685 Å. There are many Ge^+ lines in this zone observed at e.g. 4742, 4816, 5131, 5178, 5511, 5893, and 6079 Å and fewer Ge^{2+} lines at 4178 and 4260 Å. H_γ, H_β and H_α atomic hydrogen lines at, respectively, 4343, 4863 and 6561 Å are detected together with a big number of H_2 bands, indicative of abundant production of this species in the LIB of germane.

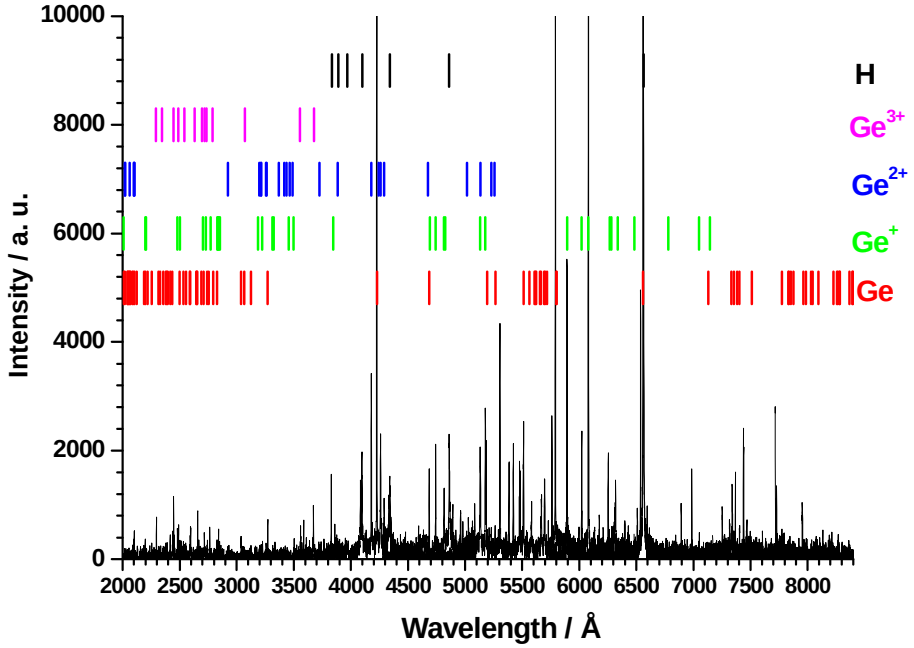

Figure 16. Low-resolution LIB emission spectra in GeH_4 produced by the 10P(26) line of the TEA-CO_2 laser at 10.693 μm and assignment of the atomic lines of Ge, Ge^+, Ge^{2+}, Ge^{3+} and atomic hydrogen.

In order to get more insight into LIB of germane and to obtain an unambiguous assignment of the emission lines, we have scanned the corresponding wavelength regions with higher resolution. This was sufficient to distinguish clearly between nearly all observed lines. Figure 17(a-d) shows a composition of several high-resolution OES of LIB (3.58 GW×cm^{-2}) in germane to 5 hPa (1960–6025 Å). The spectrum of figure 17 has been obtained with 32 successive exposures on the ICCD detector. Strong atomic Ge^{3+} ionic lines dominate the spectrum but, atomic Ge^{2+}, Ge^+, Ge and H lines also are present. The assignments of the atomic Ge (mainly in the 1960–3120 Å and 4220–5800 Å spectral regions), Ge^+ (2000–6000 Å), Ge^{2+} (2000–2100 Å and 3200–5260 Å spectral regions), and Ge^{3+}(2300–3700 Å) individual lines are indicated by stick labels. There is a good agreement between line intensities tabulated in NIST Atomic Spectral Database [58] and the measured intensities observed here for Ge, Ge^+, Ge^{2+} and Ge^{3+}. A preponderance of Ge^{3+} opposed to Ge is detected in the lines at 2445, 2488 and 2735 Å, which are the strongest of the region, although their relative intensity given by NIST [58] are much weaker than those corresponding to Ge, Ge^+ and Ge^{2+}. These facts point the high ionization of germanium produced by infrared LIB. Ge^{2+} species, although not observed in this zone, are very intense with respect to Ge as it is manifested by the lines at 2100, 2102 and 2104 Å, which are 2.4 times more intense than the Ge band at 2094.5 Å, while NIST gives 80 times more intensity for this Ge line. There is an intense line at 2298 Å identified by us as C^{2+} and a set of small bands between 2500 and 2530 Å that may be assigned to H_2. The visible part of the spectrum has the same trend as the UV region: big intensity of the more ionized lines Ge^{2+} opposed to Ge^+ (see e.g. the line at 4261 Å for Ge^{2+} and the line at 4742 Å for Ge^+) (Figure 17d). Besides in this region is

clearly manifested the large amount of H_2 formed in the infrared LIB of germane. The presence of its open rotational structure congests the spectrum throughout the whole visible region together with the H_γ, H_β and H_α atomic lines (Figure 17b-c). Several spectra in the UV region are shown in figure 17(a-f). In these spectra all the germanium lines (Ge, Ge^+, Ge^{2+} and Ge^{3+}) given by NIST [58] are found. Some weak N^+, O^+, C, C^+, C^{2+} and C^{3+} lines were also observed. It shows that the air and some impurities of carbon are ionized by the laser and by collision with the laser-induced germane plasma.

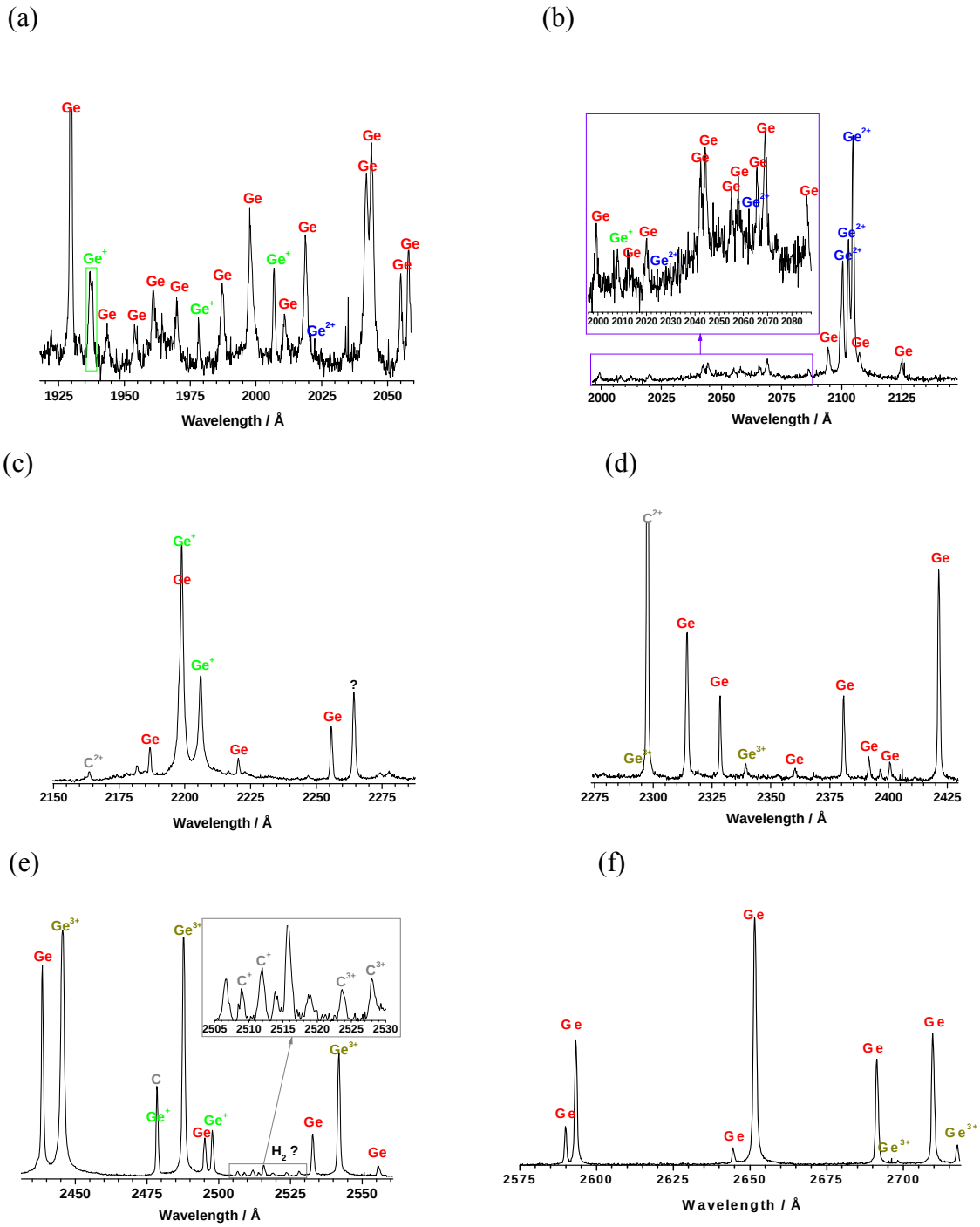

Figure 17. **(a-f)** High-resolution LIB emission spectrum observed in several spectral regions in germane excited by the CO_2 laser at 10.693 μm with a power density of 3.58 GW×cm^{-2}, and assignment of some atomic/ionic lines

For Germane plasma, the excitation temperature was obtained from the Boltzmann equation (3.16) for the intensities of several Ge and Ge^+ lines. The excitation temperatures were determined for a germane pressure of 5 hPa and CO_2 laser power density 3.58 GW×cm^{-2}. The obtained excitation temperatures were 8100 ± 300 K and 23500 ± 2500 K for Ge and Ge^+, respectively (figure 18).

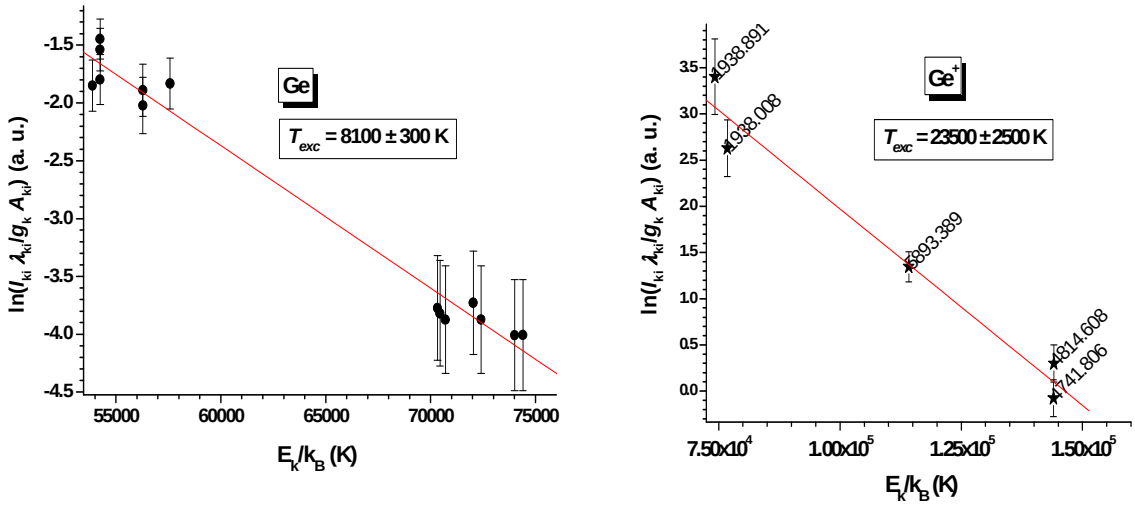

Figure 18. Linear Boltzmann plots for several Ge and Ge^+ transition lines used to calculate plasma excitation temperature, T_{exc}. Plots also show linear fits to the data.

The difference between these temperatures can be due to the different quenching rate coefficients between each species. Furthermore, this fact may be interpreted to result from the different emissivity distributions of atomic and single ionized germanium lines. The emissivity of the Ge^+ lines is produced, on the average, near the laser-induced plasma inner region with higher temperature. On the contrary, the emissivity of the Ge lines comes, on the average, from the low temperature region close to the plasma front, where the Ge^+ density is lower. The intensity measurements correspond to the integration of the local emissivity values along the line-of-sight, integrated in turn in the perpendicular directions. As a consequence, the Ge Boltzmann plot provides a temperature value which is a certain average of the low-temperature values in the plasma (8100 K), whereas the temperature obtained from the Ge^+ Boltzmann plot (23500 K) averages the values existing in the high-temperature region. Keeping in mind these results, the temperature obtained from relative intensity of Ge^+ atomic lines (23500 K) was chosen as the first approximation for the excitation temperature.

When LIB is produced in germane under high intensity laser radiation, many molecules obtain an energy that surpasses the binding energy. As a consequence, the molecules will dissociate into H and Ge atoms and ultimately some atoms can ionize and free or quasi free electrons appear in the laser focal volume. In these conditions GeH_4 becomes a mixture of electrons, positive ions such as Ge^+, Ge^{2+}, Ge^{3+} and H and Ge neutral atoms. The transition between a gas and plasma is essentially a chemical equilibrium, which shifts from the gas to the plasma side with increasing temperature. Let us consider the first three different ionization equilibria of Ge:

$$Ge(4s^2 4p^2\ {}^3P_0) \rightleftarrows Ge^+(4s^2 4p\ {}^2P^0_{1/2}) + e + IP(Ge\text{-}I),$$

$$Ge^+(4s^2 4p\ {}^2P^0_{1/2}) \rightleftarrows Ge^{2+}(4s^2\ {}^1S_0) + e + IP(Ge\text{-}II),$$

$$Ge^{2+}(4s^2\ {}^1S_0) \rightleftarrows Ge^{3+}(4s^1\ {}^2S_{1/2}) + e + IP(Ge\text{-}III),$$

where the first three ionization potentials for germanium are $E_i^{\text{Ge-I}}$ = IP(Ge-I) = 7.90 eV, $E_i^{\text{Ge-II}}$ = IP(Ge-II) = 15.935 eV, and $E_i^{\text{Ge-III}}$ = IP(Ge-III) = 34.2 eV [72]. For each ionization equilibrium, the LTE between ionization and recombination reactions at temperature T is described by the Saha equation (3.17). Figure 19 shows the ionization degree $N_i/(N_0 + N_i)$ of Ge, Ge^+ and Ge^{2+}, plotted as a function of the gas temperature T, at a constant total pressure $p = (N_0 + N_e + N_i)k_BT$ of 5 hPa. The graph shows that Ge is already fully ionized at thermal energies well below the first ionization-energy of 7.90 eV (equivalent to 91700 K). At about 1/10 of the ionization energy the majority of the germanium atoms are ionized (ionization degree 0.99). Yet, at lower temperatures the electrically charged components of a partially ionized Ge gas may dominate the behavior of the gas.

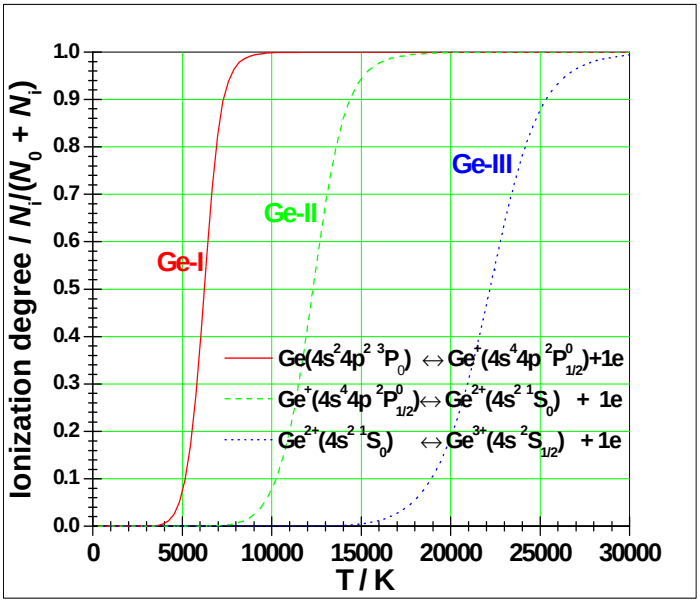

Figure 19. Temperature dependence of the ionization degree $N_i/(N_0+N_i)$ of Ge, Ge^+ and Ge^{2+} at a pressure of 5 hPa.

To see the effect of laser irradiance on the germane plasma plume high resolution spectra in the region 2710-2860 Å at different values of fluences have been obtained for a pressure of 5 hPa of germane and are given on Figure 20. These spectra were recorded after the incidence of only one pulse of the TEA-CO_2 laser. The spectral lines for the three species get wider as the fluence increase due to the pressure increase in the plasma. Figure 21 shows the variation in the emission intensity ratios of Ge^{3+}/Ge, Ge^+/Ge and Ge^{3+}/Ge^+ as a function of the laser energy. An increase in the Ge^{3+} and Ge^+ formation with respect to neutral Ge with increasing laser energy was observed. In the studied lines for an increase in the fluence of a factor of 3.7, the increase was 2.4 for the

Ge^{3+}/Ge ratio, 4.8 for the Ge^{+}/Ge proportion and 0.5 for the Ge^{3+}/Ge^{+} ratio. As it is expected, the increase in fluence affects more severely to the ionized species, being the Ge^{3+} the most influenced by this parameter. The fact that the proportion Ge^{3+}/Ge^{+} is smaller than the unit indicates that a conversion process ($Ge^{3+}+2e^{-} \rightarrow Ge^{+}$) takes place during the integration time of the measurements.

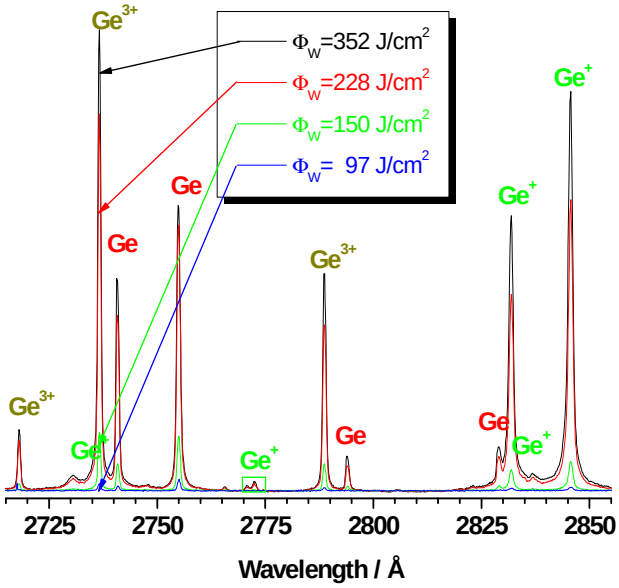

Figure 20. LIB emission spectra in germane at a pressure of 5 hPa observed in the 2715-2855 Å region, excited by the TEA-CO_2 laser as a function of the laser fluence.

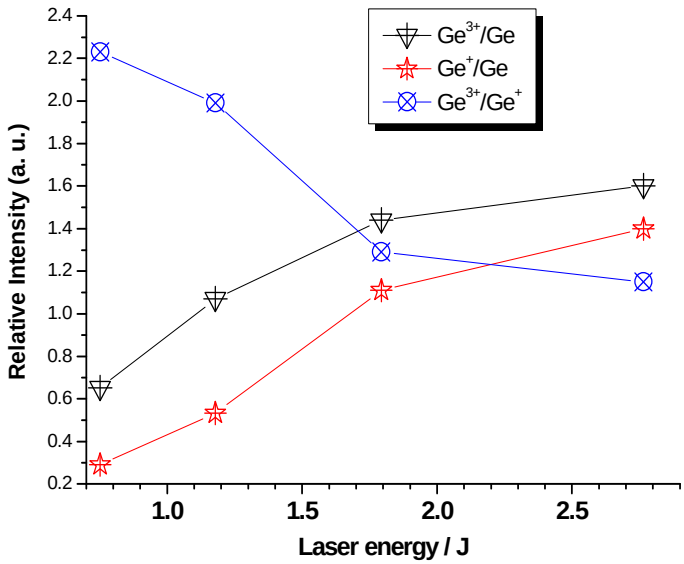

Figure 21. Variation in the emission intensity ratios of Ge^{3+}/Ge, Ge^{+}/Ge and Ge^{3+}/Ge^{+} in LIB emission spectra of germane as a function of the TEA-CO_2 laser energy.

The behavior with the germane pressure of the intensity of the lines of the three species Ge^{3+}, Ge^{+} and Ge is different. In Figure 22 we give the high resolution spectra obtained for three values of initial pressures of germane 5, 7 and 10 hPa, when are irradiated by the CO_2 laser at a pulse energy of 1793 mJ, in the UV region between 2710-2860 Å.

The intensity of Ge^{3+} increases with germane pressure from 5 to 7 hPa to decrease further up to 10 hPa. Differently, Ge^{+} increase monotonously from 5 to 10 hPa while neutral Ge atoms do not increase until 7 hPa to rise quickly up to 10 hPa. This behavior shows the different role that collisions inside of the plasma play in the formation of the different species. Above 5 hPa, the high density of species formed in the infrared LIB of germane make to the newly formed Ge^{3+} ions to lose energy in the detection time to turn into neutral Ge atoms, increasing the intensity of their lines for higher pressure conditions. However, the intensity of the lines of the Ge^{+} species increases proportionally with pressure, indicating that at least in the time of the detection the species are stable. At the highest germane pressure, the more intense spectral lines are broadened as a consequence of the high pressure associated with the plasma. As a consequence of these studies we conclude that at a higher laser fluence the plasma is more energetic and more ionized, while at higher pressures the Ge^{3+} ions relax to Ge^{+} ions and neutral Ge atoms.

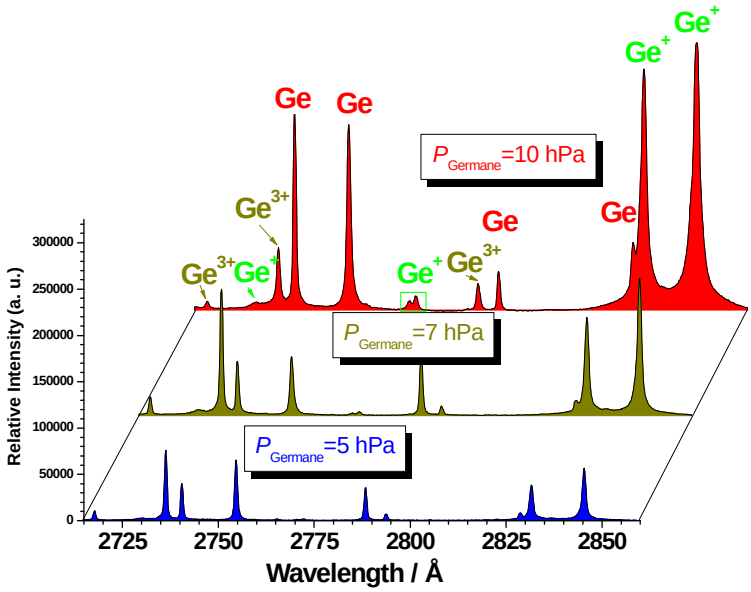

Figure 22. High-resolution LIB emission spectra at various germane pressures, excited by the TEA-CO_2 laser at a power density of 3.58 GW×cm^{-2}.

Figure 23 shows the measured breakdown threshold intensity for germane as a function of the gas pressure. As it can be seen, "threshold with fresh gas" is more than two times higher than the "threshold with a previous breakdown". Threshold for fresh gas shows a minimum which is indicative of a collisional assisted avalanche ionization mechanism, as predicted by the classical theory (see section 2.2.3) and breakdown is initiated mainly by the interaction of the laser field with the natural free electron density; in the case of the "threshold with previous breakdown" the needed energy decrease due to a higher electron density in the focal region due to natural free electron density more remaining electron from a previous breakdown. The obtained values are in agreement with threshold values for O_2, N_2 or air [16] obtained in similar conditions but lower than other reported values [9, 83, 84] because different experimental conditions (focal length of 24 cm) and beam size in the focal region (7.85×10^{-3} cm^2) used.

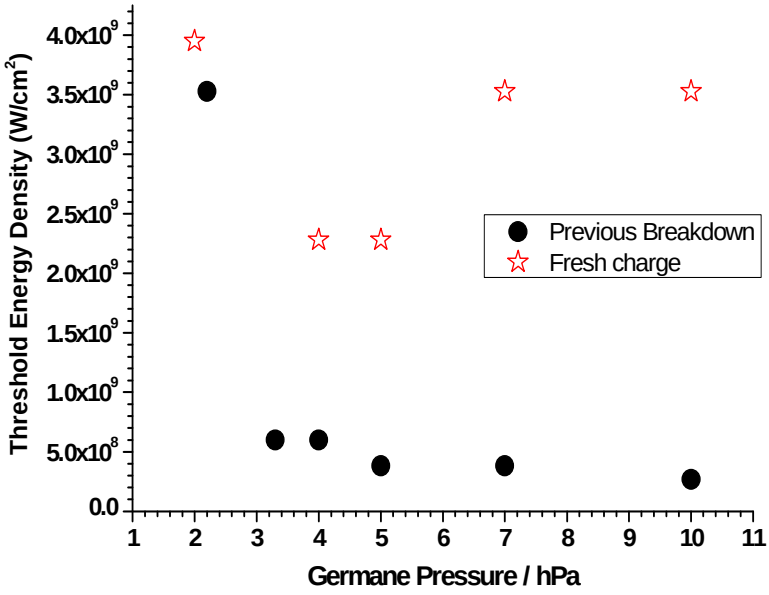

Figure 23. Experimental LIB thresholds excited by the TEA-CO_2 laser in Germane for different pressures; Solid circle: after previous breakdown and open start: fresh charge (without previous breakdown).

5.4. LIBS of CO_2

In contrast to the large number of experiments carried out on LIBS of other gases, a rather restricted number have been performed in CO_2 [25, 85-87]. This section reports temporal studies of the CO_2 plasma directly produced by a high-power IR CO_2 pulsed laser. Only CO_2 and its impurities are present in the samples. We discuss thermo-chemical processes induced by the laser pulse on carbon dioxide and we evaluate plasma changes. The characteristics of the spectral emission intensities from different species have been investigated as functions of the CO_2 pressure and laser irradiance. Optical breakdown threshold intensities in CO_2 have been measured. We discuss the dynamics of the plasma expansion and formation of C, C^+, C^{2+}, O^+ and O^{2+} species for different delay times with respect to the beginning of the laser pulse. The TOF profiles for O^+, O^{2+}, C^+ and C^{2+} species have been used for an estimation of the corresponding three-body electron-ion recombination rate constants.

In these experiments, a nanosecond CO_2 pulsed laser operating with the line 10P(14) at λ=10.532 μm and intensities from 1.2 to 5.6 GW×cm^{-2} was used. The primary CO_2 employed was of high purity >99.995 % (<30 ppmv N_2, <15 ppmv O_2, <2 ppmv C_nH_m, <1 ppmv CO, and <5 ppmv H_2O). Before every experiment, the cell was evacuated to a pressure of 4 Pa and filled with CO_2 up to the work pressure (6.4 to 101 kPa). An overview of the OES of the LIB in carbon dioxide compared with the atomic/ionic lines of C, C^+, C^{2+}, C^{3+}, O, O^+, O^{2+}, N and N^+ is displayed in figure 24. In this case the laser delivered 1320 mJ.

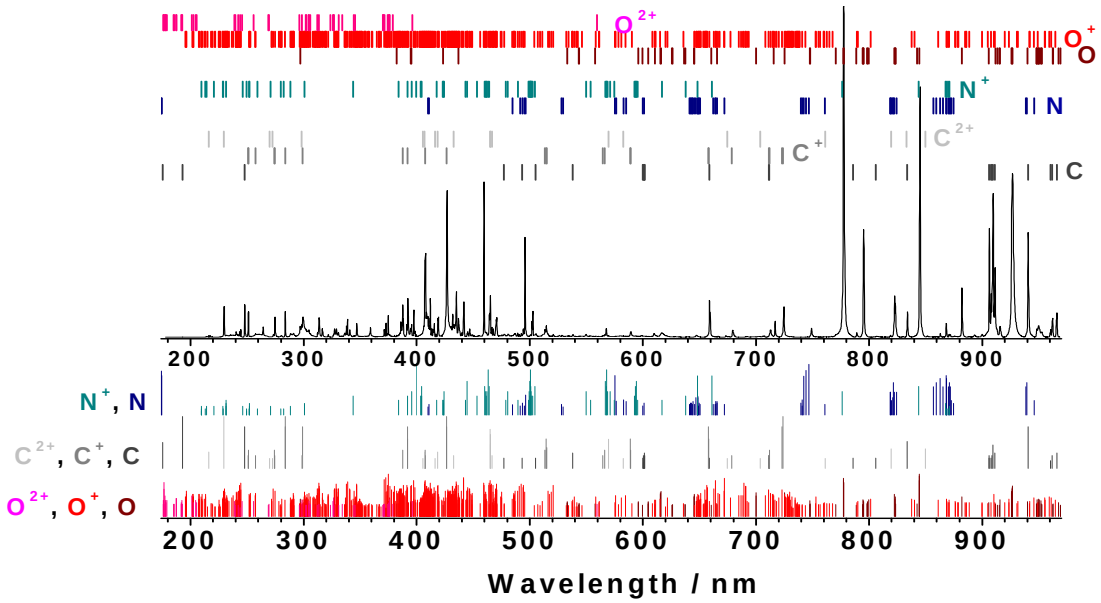

Figure 24. The LIB emission spectrum of carbon dioxide (33 kPa) plasma (Laser intensity 2.6 GW·cm^{-2}) compared with atomic/ionic lines positions and relative intensities listed at NIST of C, C^+, C^{2+}, N, N^+, O, O^+ and O^{2+}.

The assignments are indicated by stick labels. In the lower part of figure 24, the relative intensities of the observed lines are shown. There is a good agreement between the line intensities tabulated in NIST [58] and the measured intensities observed. The spectrum of figure 24 has been obtained with six successive exposures on the detector using the low-resolution spectrometer. A zoom of this spectrum is shown in figure 25. In this figure, in addition to the identified atomic/ionic lines, molecular band systems of $C_2(E^1\Sigma_g^+–A^1\Pi_u$; $e^3\Pi_g–a^3\Pi_u$; $d^3\Pi_g–a^3\Pi_u)$, $CN(B^2\Sigma^+–X^2\Sigma^+$; $A^2\Pi–X^2\Sigma^+)$, $O_2(b^1\Sigma_g^+–X^3\Sigma_g^-)$, $O_2^+(A^2\Pi_u–X^2\Pi_g)$ $N_2(C^3\Pi_u–B^3\Pi_g)$ and $N_2^+(D^2\Pi_g–A^2\Pi_u$; $B^2\Sigma_u^+–X^2\Sigma_g^+)$ are observed (see table 2). In the spectrum of figure 25(a), strong atomic/ionic C, C^+, C^{2+}, O^+, and O^{2+} lines dominate, but also molecular bands of $C_2(E\text{-}A)$, $C_2(d\text{-}a)$, N_2^+(D–A) and $O_2^+(A\text{-}X)$ are also detected. In this spectrum the predominant emitting species are the C^{2+}: $2p^2\ ^1D_2 \rightarrow 2s2p\ ^1P^o_1$ ionic line at 229.687 nm, C: $2p(^2P^0)3s\ ^1P^0_1 \rightarrow 2p^2\ ^1S_0$ atomic line at 247.856 nm, C^+: $2p^3\ ^2D^0_{5/2} \rightarrow 2s2p^2\ ^2P_{3/2}$ ionic line at 251.206 nm and C^+: $2s^23p\ ^2P^0_{3/2} \rightarrow 2s2p^2\ ^2S_{1/2}$ at 283.671 nm. In the spectrum of figure 25(b) the predominant emitting species is the C^+ multiplet $2s^24f\ ^2F^0_{J'} \rightarrow 2s^23d\ ^2D_{J''}$ at 426.7 nm. Many medium-week lines of O^+, O^{2+}, C^+ and C^{2+} and several molecular band of $CN(B\text{-}X)$ and $N_2(C\text{-}B)$ are also present. In figure 25(c) there are present very high second diffraction orders of C^+ and C^{2+} lines. The most intense lines are C^{2+}: $1s^22p(^2P°)3p\ ^3P_0 \rightarrow 1s^22s3s\ ^3S_0$ at 466.147 nm and an O^+ multiplet. Also, very weak, atomic lines of O^+, N^+, C, C^+ and H_β and several bands corresponding to C_2 are observed. The spectrum of figure 25(d) is dominated by the ionic line of C^+: $2s^23p\ ^2P^0_{1/2} \rightarrow 2s^23s\ ^2S_{1/2}$ at 658.288, C: $2s^22p4d\ ^1P^0_1 \rightarrow 2s^22p3p\ ^1P_1$ at 658.761 overlapped with the H_α line. Many weak lines of O, N, N^+, C^+, C^{2+} and lines of the molecular bands $CN(A\text{-}X)$ and O_2(b-x) are detected. The spectra of the figures 25(e) and 25(f) show most intense atomic lines of O at around 777.2, 844.6 and 926.6 nm. There are also present other weak lines of C, C^+ C^{2+}, N, O, O^+, and molecular bands of $CN(A\text{-}X)$, $C_2(A\text{-}X)$ and $O_2(b\text{-}X)$.

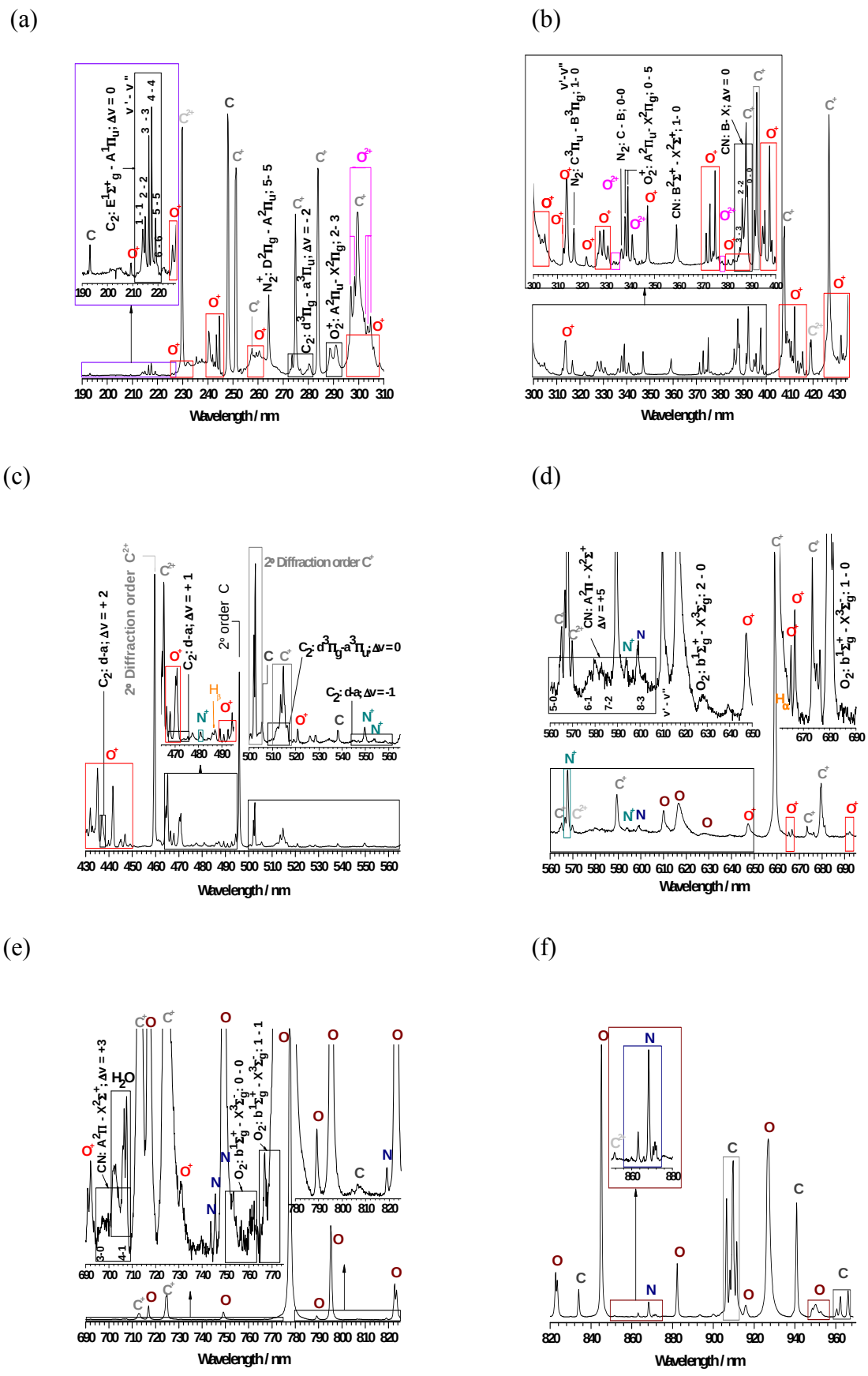

Figure 25. Low-resolution LIB emission spectrum of carbon dioxide observed in the 190–970 nm region and assignment of the atomic/ionic lines and molecular bands.

Table 2.- The most intense molecular spectral bands appearing in the LIB spectrum of CO_2.

Species	Transition	System	λ (nm), v'- v"
C_2	$E^1\Sigma^+_g - A^1\Pi_u$	Freymark bands	214.29, 0-0; 214.26, 1-1; 214.46, 2-2; 214.91, 3-3; 215.59, 4-4; 216.51, 5-5; 217.67, 6-6; 219.06, 7-7.
C_2	$e^3\Pi_g - a^3\Pi_u$	Fox-Herzberg	273.32, 0-2; 277.38, 1-3; 281.79, 2-4.
C_2	$d^3\Pi_g - a^3\Pi_u$	Swan bands	438.25, 2-0; 437.14, 3-1; 436.52, 4-2; 473.78, 1-0; 471.60, 2-1; 469.82, 3-2; 516.64, 0-0; 513.05, 1-1; 509.88, 2-2; 563.64, 0-1; 558.64, 1-2; 554.15, 2-3; 550.27, 3-4; 547.10, 4-5; 544.78, 5-6.
N^+_2	$B^2\Sigma_u^+ - X^2\Sigma_g^+$	1st negative	391.14, 0-0.
N_2	$C^3\Pi_u - B^3\Pi_g$	2nd positive	315.93, 1-0; 337.13, 0-0.
O^+_2	$A^2\Pi_u - X^2\Pi_g$	2nd negative	289.03, 2-3; 339.78, 0-5.
CN	$B^2\Sigma^+ - X^2\Sigma^+$	Violet system	359.04, 1-0; 388.39, 0-0; 387.20, 1-1; 386.22, 2-2; 385.46, 3-3; 384.91, 4-4.
CN	$A^2\Pi_i - X^2\Sigma^+$	Red system	562.73, 5-0; 575.10, 6-1; 588.03, 7-2; 601.67, 8-3; 692.76, 3-0; 709.0, 4-1.
O_2	$b^1\Sigma^+_g - X^3\Sigma^-_g$	IR atmospheric	628.65, 2-0; 688.24, 1-0; 761.92, 0-0; 770.83, 1-1.

On the other hand, the observed LIB spectrum of carbon dioxide was compared with the spectra obtained in our laboratory at others experiments [88-90].

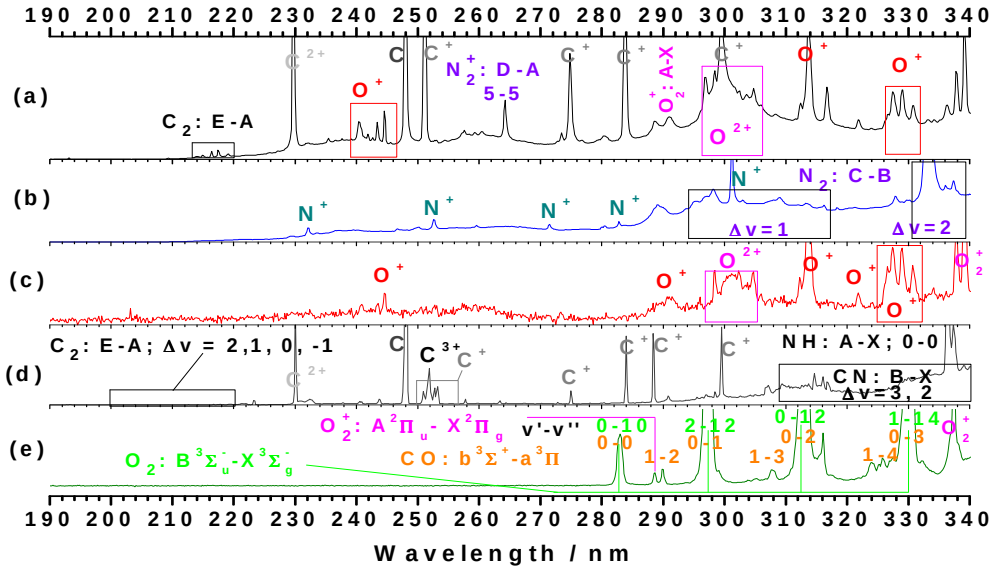

Figure 26. Portion of the low-resolution emission spectra from: **(a)** LIB of carbon dioxide at the described experimental conditions; **(b)** LIB of N_2 at 120 kPa excited by the line of 1039.36 cm^{-1} of a TEA-CO_2 laser; **(c)** LIB of O_2 at a pressure of 53 kPa, excited by the 10.951 μm line of the CO_2 laser; **(d)** LIB of graphite at an air pressure 4 Pa, excited by the 9.621 μm line of the CO_2 laser; **(e)** a *dc* electric glow discharge of carbon dioxide at low pressure.

As an example, figure 26 shows several OES at low resolution obtained in our laboratory from LIB of CO_2, N_2, O_2, graphite and a *dc* electric glow discharge of carbon dioxide at low pressure. The LIB spectra of CO_2, N_2, O_2 and C are dominated by the atomic/ionic lines while the *dc* electric glow discharge CO_2 spectrum is dominated by molecular bands. In the *dc* electric glow discharge of carbon dioxide, several bands $O_2(B^3\Sigma_u^- - X^3\Sigma_g^-)$, $O_2(b^1\Sigma_g^+ - X^3\Sigma_g^-)$, $O_2^+(A^2\Pi_u - X^2\Pi_g)$, $CO(B^1\Sigma^+ - A^1\Pi)$, $CO(b^3\Sigma^+ - a^3\Pi)$ and $CO(d^3\Pi - a^3\Pi)$. As shown in figure 26, ionic carbon or oxygen lines are not observed in a *dc* electric glow discharge of carbon dioxide (Figure 26e).

Laser-induced breakdown threshold intensities for carbon dioxide gas were measured as a function of pressure ($p < 10^5$ Pa) (figure 27).

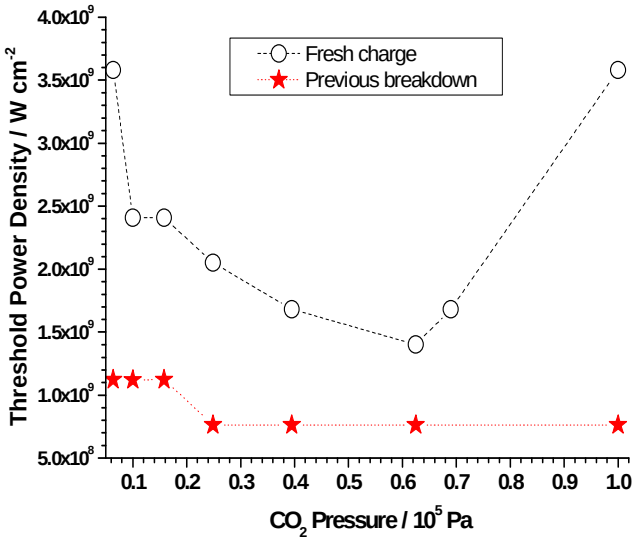

Figure 27. Experimental LIB thresholds excited by the TEA-CO_2 laser in CO_2 at 10.532 μm for different pressures; *open circles*: fresh charge (without previous breakdown) and *solid starts*: after previous breakdown. .

As it can be seen in this figure, the threshold with fresh gas is more than two times higher than the threshold with a previous breakdown. This behavior is similar to that observed for other gases. Threshold for fresh gas shows a minimum which is indicative of a collisional assisted avalanche ionization mechanism, as predicted by the classical theory (see section 2.2.3).

Experimental measurements of time-resolved emission spectra had been made in different spectral regions, at a delay time ranging from 0 to 20 μs and a distance from the target of 5 mm. Figure 28 illustrates the time-resolved evolution from laser-induced (1.7 GW×cm^{-2}) CO_2 plasma monitored at different delay times for a fixed gate width time of 0.1 μs. Immediately after the peak laser pulse ($t_d \leq 0.1$ μs) no apparent line emissions were observed and the plasma emission presents a weak continuum. This continuum radiation is emitted by the laser-induced plasma as a consequence of free-free and free-bound transitions. For $0.1 \leq t_d \leq 0.5$ μs, C emission dominates the spectrum. When the delay is increased ($t_d > 0.5$ μs), the intensity of the C^+ ionic lines steeply increases as a consequence of the expansion, recombination and heating of the plasma. At $t_d = 7$ μs, the ionic emission lines practically disappear. The intensity of C line is

appreciable for $t_d \geq 0.1$ μs reaching at maximum around 2.5 μs and being detected up to ≈15 μs.

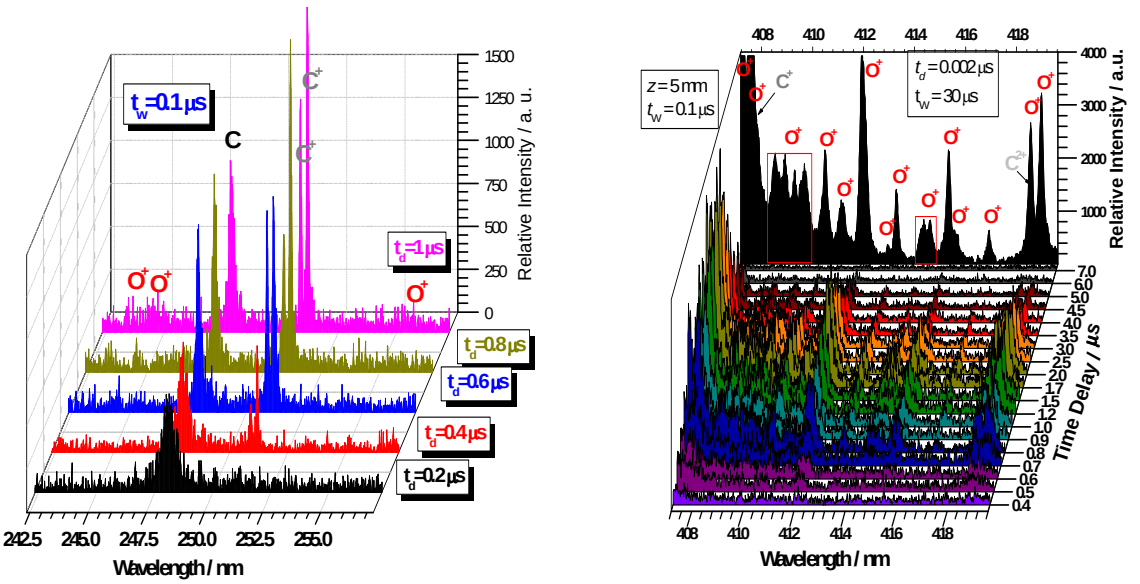

Figure 28. Time-resolved emission spectra from laser-induced carbon dioxide plasma monitored at different delay times for a fixed gate width time of 0.1 μs. The assignment of some atomic and ionic lines is indicated.

.

In addition, when the delay increases (0.5 μs≤t_d≤1.5 μs), O^+ emission line intensities steeply enhance. As the delay is further increased (t_d>1.5 μs), O^+ emission line intensities significantly and steeply decreases as a consequence of the expansion and cooling of the plasma.

The temporal evolution of spectral atomic and ionic line intensities at a constant distance from the target have been used to construct the TOF profile. Figure 29(a) displays the TOF profile for different lines of C, C^+, C^{2+}, O^+, and O^{2+} for the LIB CO_2 experiments at z=5 mm. The TOF profile of O^+(411.9 nm), O^{2+}(304.7 nm), C^+(251.2 nm), and C^{2+}(229.7 nm) species was found to consist approximately of one maximum at ≈ 1.5 μs, 1.2 μs, 1.7 μs and 1.7 μs, respectively. The TOF curve of C(247.9 nm) consists approximately of two intense maxima at ≈ 1.8 μs and ≈ 4 μs. There is a slightly delay between O^+ and O^{2+} species with respect to C^+ and C^{2+} species. This behavior appears reasonable taking into account that the available kinetic energy after the break of the CO_2 bonds is less when carbon species appear (break of two C=O bonds) than when oxygen species appear (break of one C=O bond). On the other hand the emission intensity of the ionic species decreases more rapidly than the emission intensity of the atomic carbon line. The time duration of ionic species was nearly 6 μs, while the time duration of C atomic emission was nearly 15 μs. The velocity distributions that are derived from the TOF profiles are displayed in figure 29(b). In the described experimental conditions, the velocity distributions present different characteristics. The velocity distributions of O^+ and O^{2+} species are centred at about 3.3 km/s, while for C^+ and C^{2+} species the maxima are centred at about 2.5 km/s. We observed that the C^+, C^{2+}, O^+, and O^{2+} velocities have a similar behaviour. According to this result, the formation processes for all ionic species must be similar. On the other hand, we have studied time-

resolved OES of the CO_2 plasma by varying the laser irradiance. We have observed that the laser intensity is increased; the TOF profiles for ionic species broaden and move toward lower delay times. The velocity distribution of atomic carbon is comparative wider than the velocity distributions of ionic species. This behaviour is possibly due to the less energy necessary for its formation taking advantage of the pulse tail and also to the continuous recombination of ions with electrons to give excited carbon atoms.

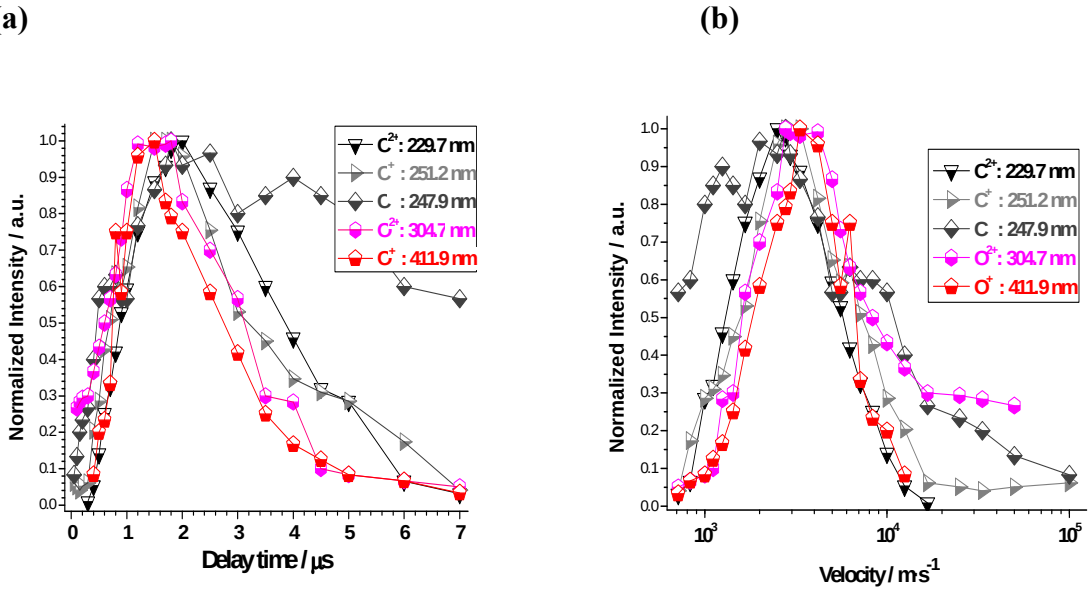

Figure 29. **(a)** Number density TOF distributions of different atomic/ionic lines as a function of delay time for a laser intensity of 1.7 GW×cm^{-2}. **(b)** Velocity distributions derived from the experimental TOF profiles for the indicated species.

The plasma temperature was obtained from the slope of the plot of Eqn. (3.16) for the line intensities of several O^+ lines at a delay time of 1.5 µs. The obtained value was 25900 ± 2100 K. For any given plasma to be considered to be in LTE the lower limit for the electron number density n_e must satisfy McWhirter's criterion (Eq. 3.4). At an evaluated temperature of 25900 K this criterion yields $n_e \approx (0.6\text{-}2.5)\times10^{16}$ cm^{-3} for different transitions observed in O^+. This electron density is lower than the deduced values from the Stark broadening (see further). Based on these calculations, the LTE assumption seems to be satisfied at least during the first 3 µs of the plasma lifetime. On the other hand, by considering two lines of the same species, characterized by different values of the upper energy level, the relative intensity ratio can be used to calculate the plasma excitation temperature (Eq. 3.15). This method was used for estimating the excitation temperature at different delay times (Figure 30) with two O^+ lines at 415.3 and 418.9 nm. Immediately, when the plasma breakdown occurred, it was difficult to observe the O^+ emission lines separated from the corresponding background level because a very intense background continuum was emitted. Therefore, the excitation temperatures were estimated after a delay time of 0.5 µs. One observes that the excitation temperature is rapidly elevated up to a delay time of 1.2 µs and after that, this temperature decreases. The decreasing of the excitation temperature is due to the adiabatic expansion of the plasma. During this expansion the thermal energy is converted in to the kinetic energy and the plasma cools down rapidly.

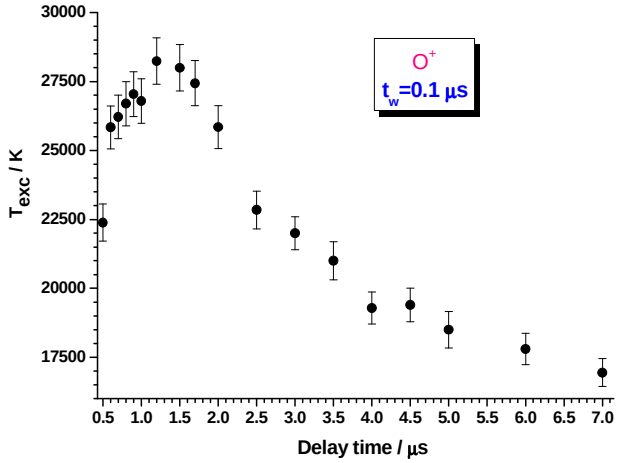

Figure 30. Time-resolved evolution of the excitation temperature of CO_2 plasma produced in carbon dioxide at 33 kPa using two O^+ lines. The error bars represent 3 % of uncertainty.

The electron density was obtained using the widths of the O^+ line ($2s^2 2p^2(^3P)3d\ ^4D_{J'} \longrightarrow 2s^2 2p^2(^3P)3p\ ^4P^0_{J''}$) at ≈ 411.1 nm. By substituting the Stark line widths of O^+ multiplet at different delay times in Eqn. (3.12) and the corresponding values of the electron impact parameter, W (0.0224-0.0137 nm from Griem [54] at plasma temperatures between 5000 and 40000 K), we obtain the electron density for different delay times. Figure 31 gives the time evolution of electron density and its first derivative with respect to delay time by setting the gate width of the intensifier at 0.1 µs and a laser intensity of 1.7 GW×cm^{-2}. Multiple measurements lead to a statistical error of the electron density below 10%. The initial electron density at 0.2 µs is approximately 5.1×10^{16} cm^{-3}. Afterwards, the density increases and reaches a maximum (2.5×10^{17} cm^{-3}) at 1.5 µs, and then decreases as the time is further increased. After 7 µs the electron density is about 6.1×10^{15} cm^{-3}.

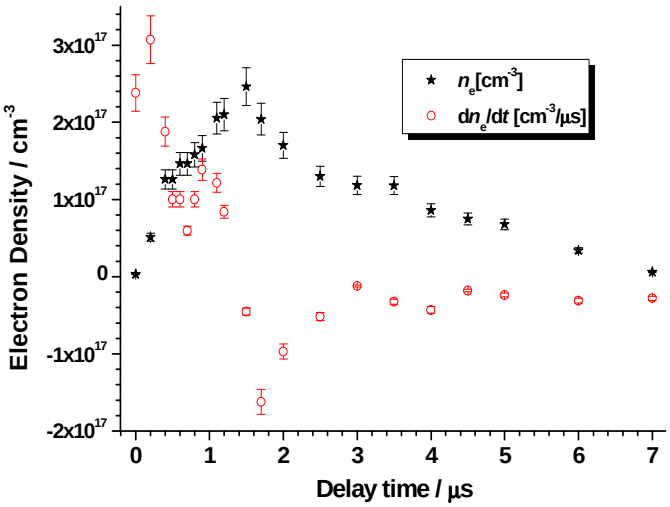

Figure 31. The temporal evolution of electron density n_e and dn_e/dt for different delay times from plasma ignition

The decrease of n_e is mainly due to recombination between electrons and ions in the plasma. These processes correspond to the so-called radiative recombination and three-body recombination processes in which a third body may be either a heavy particle or an electron.

As it is observable from figure 31, the dynamical equilibrium (see section 2.2.2) can be established at 1.35 μs. For $t < 1.35$ μs the ionization prevails while for $t > 1.35$ μs the three-body electron recombination process dominates over the ionization one. By a non-linear fit of the intensities for O^+, O^{2+}, C^+ and C^{2+} as function of the delay time to a single exponential decay, we obtained three recombination times of t_{rec}=1.7 ± 0.1 μs. 1.8 ± 0.1 μs, 2.2 ± 0.1 μs and 4.2 ± 0.1 μs respectively. The rate constants of the recombination processes can be estimated from the relation $k_{rec}=1/(n_e^2.t_{rec})$. The corresponding values for O^+, O^{2+}, C^+ and C^{2+} are 4.2×10^{-27}, 3.9×10^{-27}, 3.2×10^{-27} and 1.7×10^{-27} cm^6 s^{-1}, respectively. These values are similar to other literature's reported data [41,42].

6. CONCLUSION

This chapter reviews some fundamentals of LIBS and some experimental studies developed in our laboratory on He, Ge, GeH_4 and CO_2 using a high-power pulsed laser. In this experimental study we have used several laser wavelengths and different laser intensities in the order of GW×cm^{-2}. In the case of solid ablation, medium-vacuum conditions (≈ 4 Pa) were used. The spectra of the generated plasmas are dominated by emissions of strong atomic, ionic species and molecular bands. For the assignment of the molecular bands a comparison with conventional emission sources was made. Excitation temperatures, ionization degrees and electron number densities for some species were estimated by using different spectroscopic methods. The characteristics of the spectral emission intensities from different species have been investigated as functions of the gas pressure and laser irradiance. Optical breakdown threshold intensities in He, GeH_4 and CO_2 gases have been experimentally measured. The physical processes leading to laser-induced breakdown of the gases have been analyzed. Plasma characteristics in LIBS of different samples were examined in detail on the emission atomic/ionic lines by means of time-resolved OES technique. The results show a faster decay of continuum and ionic spectral species than of neutral atomic and molecular ones. The velocity and kinetic energy distributions for different species were obtained from TOF measurements. Excitation temperature and electron density in the laser-induced plasma were estimated from the analysis of spectral data at various times from the laser pulse incidence. From TOF measurements, recombination times and three-body recombination rate constants were estimated for different ionic species.

ACKNOWLEDGMENTS

We would like to gratefully acknowledge the funding support received in part by the DGICYT (Spain) Projects: MEC: CTQ2008-05393/BQU and MEC: CTQ2010-15680/BQU for this research. We deeply gratefully acknowledge Professor Magna Santos, recently retired at "Consejo Superior de Investigaciones Científicas", Madrid, for important contributions to this article.

REFERENCES

[1] Maker, PD; Terhune, RW; Savage, CM. Proc. 3rd Int. Conf. Quantum Electronics; (Paris: Dunod) 1963, Vol. 2, 1559.

[2] Raizer, YP. Breakdown and heating of gases under the influence of a laser beam; Soviet Physics: Uspekhi. Vol. 8, Nº 5, 1966.

[3] Raizer, YP. Laser-Induced discharge phenomena; Consultants Bureau: New York. 1977.

[4] Bebb, HB; Gold, A. Multiphoton Ionization of Hydrogen and Rare Gas Atoms; Physics of Quantum Electronics; ed P L Kelly et al McGraw-Hill: New York. 1966.

[5] De Michelis, C. IEEE J. Quantum Electron. 1969, 5, 188-202.

[6] Morgan, CG. *Rep. Prog. Phys*., 1975, 38, 621-665.

[7] Bekefi, G. Principles of Laser Plasma; Wiley: New York. 1976.

[8] Lyman, JL; Quigley, GP; Judd; OP. Multiple-Photon Excitation and Dissociation of Polyatomic Molecules; Ed. Cantrell, CD. Springer: Berlin., 1980.

[9] Rosen, DI; Weyl, GJ. *Phys. D. Appl. Phys*., 1978, 20, 1264-1276.

[10] Gamal, YE. EDJ. Phys, *D. Appl. Phys*., 1988, 21, 1117-1120.

[11] Yueh, FY; Singh, JP; Zhang, H. Encyclopedia of Analytical Chemistry (Laser-lnduced Breakdown Spectroscopy, Elemental Analysis); ed R A Meyers. Wiley: *Chichester*. 2000.

[12] Cremers, DA; Radziemski, LJ. *Handbook of Laser-lnduced Breakdown Spectroscopy*; Wiley: Chichester. 2006.

[13] Miziolek, AW; Palleschi, V; Schechter, I. Laser-Induced Breakdown Spectroscopy; Cambridge University Press: Cambridge. 2006.

[14] Singh, JP; Thakur, SN. Laser-Induced Breakdown Spectroscopy; Elsevier:, New York. 2007.

[15] Yong-Ill, L. Laser Induced Breakdown Spectrometry; Nova Science Publishers: New York 2000.

[16] Camacho, JJ; Diaz, L; Santos, M; Juan LJ; Poyato JML In *Laser Beams: Theory, Properties and Applications*; Thys M; Desmet E. Eds. Optical Breakdown in Gases induced by High-Power IR CO_2 Laser Pulses; Nova Science Publishers: New York 2009.

[17] Kroto, HW; Heath, JR; O'Brien, SC; Curl, RF; Smalley, RE. *Nature,* 1985, 318, 162-163.

[18] Ikegami, T; Nakanishi, F; Uchiyama, M; Ebihara, K. *Thin Solid Films,* 2004, 457, 7-11.

[19] Ashfold, MNR; Claeyssens, F; Fuge, GM; Henley, SJ. *Chem. Soc. Rev.,* 2004, 33, 23-31.

[20] Yueh, FY; Singh, JP; Zhang, H. In *Encyclopedia of Analytical Chemistry*; Meyers RA. Ed. Laser-induced Breakdown Spectroscopy; Elemental Analysis; John Wiley & Sons Ltd, Chichester, 2000, pp 2066-2087.

[21] Camacho, JJ; Poyato JML; Diaz, L; Santos, M; In *Applied Physics in the 21st Century:* Valencia RP Ed. Spectroscopic Analysis of Chemical Species in Carbon Plasmas induced by High-Power IR CO_2 Laser; Nova Science Publishers: New York 2009.

[22] Santos, M; Diaz, L; Camacho, JJ; Poyato, JML; Pola, J; Krenek, T; Appl. Phys. A, 99, 811, 2010.

[23] Camacho JJ; Diaz, L; Santos, M; Poyato, JML in Spectrochim. Acta B, 66, 57, 2011.

[24] Camacho JJ; Diaz, L; Poyato, JML Aceppeted to publication in J. Appl. Phys.

[25] Camacho JJ; Diaz, L; Cid, JP; Poyato, JML Sent to publication.

[26] Cremers, DA; Radziemski, LJ. *Handbook of Laser-lnduced Breakdown Spectroscopy*; Wiley: Chichester, England, 2006.

[27] Miziolek, AW; Palleschi, V; Schechter, I. (Eds.), *Laser-lnduced Breakdown Spectroscopy;* Cambrige. 2006.

[28] Singh, JP; Thakur, SN. (Eds.) *Laser-lnduced Breakdown Spectroscopy*; Elsevier: Oxford UK, 2007, Vol. 1, pp 1-427.

[29] Yong-Ill, L., *Laser Induced Breakdown Spectrometry*; Nova Science Publishers: New York 2000.

[30] Chan, F. *Introduction to plasma physics and controlled fusion*; Plenum Press: New York. 1984.
[31] Weyl, GM. *Laser-induced plasmas and applications.* In: Radeziemski, Cremers, editors, New York: Marcel Dekker; 1989 [Chapter 1].
[32] Hughes, TP. *Plasma and laser light*, Wiley: New York. 1975.
[33] Keldysh, T. *Sov Phys JETP*, 1965, 20, 1307–1314.
[34] Gold, A; Bebb, HB, *Phys. Rev. Lett.* 1965, 14, 60-63.
[35] MacDonald, AD. Microwave Breakdown in Gases; Wiley: New York. 1966.
[36] Raizer, YP. Gas Discharge Physics; Springer: Berlin, Heidelberg. 1991.
[37] Kopiczynski, TL; Bogdan, M; Kalin, AW; Schotwau, HJ; Kneubuhl, FH. *Appl. Phys. B. Photophys. Laser Chem*., 1992, 54, 526-530.
[38] Tozer, BA. *Phys. Rev*., 1965, 137, 1665-1667.
[39] Radziemski, LJ; Cremers, DA; Laser-induced plasma and applications; New York: Dekker. 1989.
[40] Gurevich, A; Pitaevskii, L. *Sov. Phys. JETP*, 1962, 19, 870-871.
[41] Capitelli, M; Capitelli, F; Eletskii, A. *Spectrochim*. *Acta B*., 2000, 55, 559-574.
[42] Capitelli, M; Casavola, A; Colonna, G; Giacomo, AD. *Spectrochim*. *Acta B*., 2004, 59, 271-289.
[43] Chan, CH; Moody, CD; McKnight, WBJ. *Appl. Phys*., 1973, 44, 1179-1188.
[44] Haught, AF; Meyerand, RG; Smith, DC. *Physics of Quantum Electronics*; In P. L. Kelley, B. Lax, & P. E. Tannenwald (Eds.), MacGraw-Hill: New York. 1966. 509.
[45] Young, M; Hercher, M. *J. Appl. Phys*., 1967, 38, 4393-4400.
[46] Barchukov, AI; Bunkin, FV; Konov, VI; Lubin, AA. Sov. *Phys. JETP*, 1974, 39, 469-477.
[47] Hermann, J; Boulmer-Leborgne, C; Mihailescu, IN; Dubreuil, B. *J. Appl. Phys*., 1993, 73, 1091-1099.
[48] Offenberger, AA; Burnett, NH. *J. Appl. Phys*., 1972, 43, 4977-4980.
[49] Donaldson, TP; Balmer, JE; Zimmermann, JA. *J. Phys. D: Appl. Phys*., 1980, 13, 1221-1233.
[50] Meyerand, RG; Haught, AF. *Phys. Rev. Lett*., 1964, 13, 7-9.
[51] Spitzer, L. Physics of Fully Ionised Gases; John Wiley: New York. 1962.
[52] Russo, RE; Geohegan, DB; Haglund, RF; Murakami, K (Eds.) *Laser Ablation*; Elsevier, Amsterdam. 1998.
[53] Amoruso, S; Bruzzese, R; Spinelli, N; Velotta, R. *J. Phys*. *B: At. Mol. Opt. Phys.*1999, 32, R131-R172.
[54] Griem, HR. Principles of plasma spectroscopy; University Press: *Cambridge*., 1997.
[55] Griem, HR. *Phys. Rev*., 1962, 128, 515-523.
[56] Huddlestone, RH; Leonard, SL. Plasma Diagnostic Techniques; Academic Press: New York. 1965.
[57] Hutchinson, IH. Principles of plasma diagnostic; University Press: Cambridge. 2002.
[58] NIST Atomic Spectra Database online at http://physics.nist.gov/PhysRefData/ ASD/index.html
[59] Cabalin, LM; Laserna, JJ; *Spectrochim. Acta Part B*, 1998, 53, 723-730.
[60] Demtröder, W. *Laser Spectroscopy*. Vol. 2. Experimental Techniques. Springer. Berlin 2008.
[61] Bogaerts, A; Chen, Z. *Spectrochim. Acta Part B,* 2005, 60, 1280-1307.
[62] Zeldovich, YB; Raizer, YP. *Physic of Shock waves and high temperature hydrodynamics phenomena*. Academic, New York 1966.
[63] Drogoff, LB; Margotb, J; Chakera, M; Sabsabi, M; Barthelemy, O; Johnstona, TW; Lavillea, S; Vidala, F; Kaenela, VY. Spectrochim. *Acta Part B*., 2001, 56, 987-1002.
[64] Benderskii, AV; Zadoyan, Z; Schwentner, N; Apkarian, VA; *J. Chem. Phys.* 1999, 110, 1542-1557.
[65] Kim, KY; Alexeev, I; Milchberg, M; *Optics Express,* 2002, 10, 1563-1572.
[66] Hermann, J; Bruneau, S; Sentis, M; *Thin Solid Films,* 2004, 453, 377-382.

[67] Abdulmadjid, SN; Suliyanti, MM; Kurniawan, KH; Lie, TJ; Pardede, M; Hedwig, R; Kagawa, K; Tjia, MO; *Appl. Phys. B*, 2006, 82, 161-166.
[68] Mao, XL; Wen, S; Russo, RE; *Appl. Surf. Sci.* 2007, 253, 6316-21.
[69] Ramli, M; Kagawa, K; Abdulmadjid, SN; Idris, N; Budi, WS; Marpaung, MA; Kurniawan, KH; Lie, TJ; Suliyanti, MM; Hedwig, R; Pardede, M; Lie, ZS; Tjia, MO; *Appl. Phys. B*, 2007, 86, 729-734
[70] Henry, CA; Diwakar, PK; Hahn, DW; *Spectrochim Acta B* , 2007, 62, 1390-1398
[71] Ramli, M; Idris, N; Fukumoto, K; Niki, H; Sakan, F; Maruyama, T; Kurniawan, KH; Lie, TJ; Kagawa, K; *Spectrochim Acta B*, 2007, 62, 1379-1389.
[72] Martin, WC; Zalubas, RJ. *Phys. Chem. Ref. Data*., 1983, 12, 323-379.
[73] Fleurier, C; Gall; PL. J. *Phys. B: At. Mol. Opt. Phys.* 1984, 17, 4311-4322.
[74] Pittman, TL; Fleurier, C; *Phys. Rev. A*, 1986, 33, 1291-1296.
[75] Griem; HR; Shen; KY; *Phys. Rev.* 1961, 122, 1490-1496.
[76] Skoog, MD; West, DM; Holler, FJ; eds. *Fundamental of Analytical Chemistry*; Harcourt Brace and Company: Florida, 1997.
[77] Yamada, S; Oguri, S; Morimoto, A; Shimizu, T; Minamikawa, T; Yonezawa, Y; *Jpn. J. Appl. Phys.* 2000, 39, 278-280.
[78] Sande, JCG; Afonso, CN; Escudero, JL; Serna, R; Catalina, E; Bernabeu, E; *Appl. Optics* 1992, 31, 6133-6138.
[79] Wolf, PJ; *Appl. Phys. A*, 1996, 62, 553-558.
[80] Nemet, B; Musiol, K; *Contrib. Plasma Phys.* 1999, 39, 85-88.
[81] Popovic; LC; Dimitrijevic; MS, *Bull. Astron. Belgrade*, 1977, 156, 173-178.
[82] Dimitrijevic; MS, Jovanovic, P; Simic, Z; *Astronomy & Astrophysics*, 2003, 410, 735-739.
[83] Striker; J; Parker, JG; *J. Appl. Phys.* 1982, 53, 851-855.
[84] Gasmi, T; Zeaiter, HA; Ropero, G; Gonzalez-Ureña, A; *Appl. Phys. B*, 2000, 71, 169-175.
[85] Francois, V; Ilkov, FA; Chin, SL; *J. Phys. B: At. Mol. Opt. Phys.* 1992, 25, 2709-2724.
[86] Ling, H; Shen, XK; Han, YX; Lu, YF; *Proc. of SPIE*, 2006, 6107, 61070A1-61070A8.
[87] Kiefer, J; Troger, JW; Seeger, T; Leipertz, A; Li, B; Li, ZS; Alden. M; *Meas. Sci. Technol.* 2010, 21, 065303-065309.
[88] Camacho, JJ; Poyato, JML; Diaz, L; Santos, M; *J. Phys. B: At. Mol. Opt. Phys.* 2007, 40, 4573-4590.
[89] Camacho, JJ; Santos, M; Diaz, L; Poyato, JML; *J. Phys. D: Appl. Phys.* 2008, 41, 215206-215219.
[90] Camacho, JJ; Diaz, L; Santos, M; Reyman, D; Poyato, JML; *J. Phys. D: Appl. Phys.* 2008, 41, 105201-105213.